Thin Film Mechanics

Ryan C. Cooper

Columbia University

2014

ABSTRACT
Thin Film Mechanics
Ryan C. Cooper

This doctoral thesis details the methods of determining mechanical properties of two classes of novel thin films suspended two-dimensional crystals and electron beam irradiated microfilms of polydimethylsiloxane (PDMS). Thin films are used in a variety of surface coatings to alter the opto-electronic properties or increase the wear or corrosion resistance and are ideal for micro- and nanoelectromechanical system fabrication. One of the challenges in fabricating thin films is the introduction of strains which can arise due to application techniques, geometrical conformation, or other spurious conditions. Currently, inadequate models exist to model strain within thin films, making it difficult to produce structurally robust thin films and to prevent premature failure of a coating or device. It is thus imperative to understand and quantify thin film behavior under strain, both to aid in the development of new materials and processing techniques, as well as to enable the implementation of thin films into new designs.

Chapters 2-4 focus on two dimensional materials. Two dimensional materials represent the intrinsic limit of thin films–being constrained to one atomic or molecular unit of thickness. These materials have mechanical, electrical, and optical properties ideal for micro- and nanoelectromechanical systems with truly novel device functionality. As such, the breadth of applications that can benefit from a treatise on two dimensional film mechanics is reason enough for exploration. This study explores the anomylously high strength of two dimensional materials. Furthermore, this work also aims to bridge four main gaps in the understanding of material science: bridging the gap between *ab initio* calculations and finite element analysis, bridging the gap between *ab initio* calculations and experimental results, nanoscale to microscale, and microscale to mesoscale. A nonlinear elasticity model is used to determine the necessary elastic constants to define the strain-energy density function for finite strain. Then, *ab initio* calculations–density functional theory–is used to calculate the nonlinear elastic response. Chapter 2 focuses on validating this methodology with atomic force microscope nanoindentation on molybde-

num disulfide. Chapter 3 explores the convergence criteria of three density functional theory solvers to further verify the numerical calculations. Chapter 4 then uses this model to investigate the role of grain boundaries on the strength of chemical vapor deposited graphene. The results from these studies suggest that two dimensional films have remarkably high strength–reaching the intrinsic limit of molecular bonds.

Chapter 5 explores the viscoelastic properties of heterogeneous polydimethylsiloxane (PDMS) microfilms through dynamic nanoindentation. PDMS microfilms are irradiated with an electron beam creating a 3 μm-thick film with an increased cross-link density. The change in mechanical properties of PDMS due to thermal history and accelerator have been explored by a variety of tests, but the effect of electron beam irradiation is still unknown. The resulting structure is a stiff microfilm embedded in a soft rubber with some transformational strain induced by the cross-linking volume changes. Chapter 5 employs a combination of dynamic nanoindentation and finite element analysis to determine the change in stiffness as a function of electron beam irradiation. The experimental results are compared to the literature.

The results of these experimental and numerical techniques provide exciting opportunities in future research. Two dimensional materials and flexible thin films are exciting materials for novel applications with new form factors, such as flexible electronics and microfluidic devices. The results herein indicate that one can accurately model the strength of two dimsensional materials and that these materials are robust against nanoscale defects. The results also reveal local variation of mechanical properties in PDMS microfilms. This process allows one to design substrates that flex with varying amounts of strain on the surface. Combining the mechanics of two dimensional materials with that of a locally irradiated PDMS film could achieve a new class of flexible microelectromechanical systems. Large-scale growth of two dimensional materials will be structurally robust–even in the presence of nanostructural defects–and PDMS microfilms can be irradiated to vary strain of the electromechanical systems. These systems could be designed to investigate electromechanical coupling in two dimensional films or for a substitute to traditional silicon microdevices.

Contents

List of Figures

List of Tables

Acknowledgments

When I enrolled at Columbia University, I moved into Morningside Heights and would ride my bike to the Upper East Side to visit my girlfriend in Cornell's medical school dormitory. As I leave five years later, Michele and I have married and our family size has doubled. I would like to sincerely thank Gail, Harry, Helayne, Jaimee, Lindsay, and Rob for not just welcoming me into the family but fully embracing and supporting me.

The support from loved ones has steadily grown over the years as I make new friends and grow closer with old ones. I would like to thank my friends for their excitement and encouragement–even if they did not understand what I had been doing. Thank you everyone from East Lyme High School, Drexel, and Columbia that has helped distract, focus, and make these fourteen years of education so enjoyable.

Dedicated to Michele.

Saunter down a path

I notice the flowers bloom

Holding hands with you

Chapter 1

Introduction

Thin film technologies have seen rapid growth over the past century as new processes and materials are developed to create smaller and lower-power devices. Micro- and nanomelectromechanical systems (MEMS and NEMS) typically use thin films ranging from 100 µm to less than 1 nm. Micro- and nanofabrication techniques typically employ micro- and nanofilms to precisely define geometries, chemical, or electrical elements on a surface–silicon or otherwise. Thin films are used in a variety of coatings to alter the opto-electronic properties or increase the wear or corrosion resistance. These films provide the opportunity for miniaturized devices, lower power consumption, high precision manufacturing, smaller form factor, and less material use to name a few benefits.

One of the challenges in fabricating thin films is the introduction of residual strains due to application techniques, geometrical conformation, or other spurious conditions. These thin film stresses were first documented by Mills in 1877[67] and again by Bouty in 1879 coining the term "electrostiction"[10]. Stoney then helped to quantify these "electrostiction" stresses in 1909[100]. It is quite common for thin films to deform and tear before accomplishing the designed task [10, 67, 100]. Even if the thin film is not a moving or load-bearing part, the existence of residual strains and surface forces can cause premature failures in devices. In order to mitigate these failures it is important to characterize the mechanical properties of thin films and their interaction with the substrates. This work aims to provide a framework for analyzing thin films in a variety of nume-

rical and experimental techniques. Two-dimensional crystals and PDMS microfilms are explored in depth, but these methods are widely applicable to variety of novel material characterization.

This work employs nanoindentation to investigate the mechanical response of novel thin films, therefore I would be remiss to neglect introduction of modern nanoindentation. A traditional hardness test uses a tip of known geometry (e.g. Knoop, Vickers, Berkovich, etc.) and uses a known force, F to drive the tip into the surface of the sample. After the tip is removed, one inspects the impression left by the indenter tip and measures the area, A. The hardness, H is calculated as $H = F/A$. The hardness of a material can be described as the resistance of a material to plastic deformation. Indeed, an empirical result of hardness measurements is $H \propto \sigma_{yield}$ and $H \propto \sigma_{UTS}$, where σ_{yield} is the yield strength of a material–stress beyond which the material is left with permanent deformation–and σ_{UTS} is the ultimate tensile strength of the material–the stress beyond which there is damage or failure of a material [11, 77]. Oliver and Pharr are credited with developing the first modern nanoindenter in 1992 [74]. During loading, the material is deforming in an elastic-plastic fashion and during unloading, the material recovers elastically. Measuring the stiffness during unloading, $S = \partial F/\partial d$–where F and d are force and displacement, respectively–the modulus of the material is then determined to be $E \propto S/A$. Nanoindentation thus depends upon three main components, force-displacement measurement, knowing the area of contact as a function of depth, and an accurate determination of the initial point of contact. Once these three components are determined in a test, one can then add a sinusoidal forcing function to measure both H and E as a function of depth. The burgeoning field of nanoindentation has grown since its initial development into a variety of applications, that are beyond the scope of this thesis because it has been covered in other publications [19, 75, 109].

This work employs nanoindentation techniques to determine the mechanical properties of novel thin film materials for use in MEMS and NEMS technologies. Nanoindentation results rarely provide a straightforward stress-strain response of a material under loading–the exception lying in microcolumn compression testing, which is by no means a trivial

experimental procedure[29]. The measured force-displacement curve of materials under nanoindentation usually results in a nonlinear response sometimes compounding both geometric and material nonlinearities. The real benefit to nanoindentation of materials is the ability to apply highly localized stress concentrations to test micro- and nanofilms. Interpreting the results of nanoindentation requires some assumption about the material's response to loading. In chapters 2-4, the 2D materials are assumed to store energy in an nonlinear elastic manner (i.e. reversibly) until the point of brittle fracture. Chapter 5 assumes that the layers of PDMS behave in a linear viscoelastic manner (i.e. the storage of energy and loss of energy during loading are separable and proportional to strain and strain rate, respectively). These material assumptions necessitate an analytical or numerical model to predict the behavior of the assumed material properties under nanoindentation. The model can then either be validated or refined to reflect experimental measurements.

Chapter 2 investigates the nonlinear elastic properties of two dimensional molybdenum disulfide. We derive a thermodynamically rigorous non-linear elastic constitutive equation and then calculate the non-linear elastic response of two-dimensional MoS_2 with first-principles density functional theory (DFT) calculations. The non-linear elastic properties are used to predict the behavior of suspended monolayer MoS_2 subjected to a spherical indenter load at finite strains in a multiple length scale finite element analysis model. The model is validated experimentally by indenting suspended circular MoS_2 membranes with an atomic force microscope. We find that the two-dimensional Young's modulus and intrinsic strength of monolayer MoS_2 are 130 N/m and 16.5 N/m, respectively. The results approach Griffith's predicted intrinsic strength limit of $\sigma_{int} \sim \frac{E}{9}$, where E is the Young's modulus. This study reveals the predictive power of first-principles density functional theory, in the derivation of non-linear elastic properties of two-dimensional MoS_2. Furthermore, the study bridges three main gaps that hinder understanding of material properties: DFT to finite element analysis (FEA), experimental results to DFT, and the nanoscale to the microscale. In bridging these three gaps the experimental results validate the DFT calculations and the multiscale constitutive model. This work

was published in *Physical Review B* in January 2013.

Chapter 3 thoroughly compares density functional theory calculations across three solvers to verify the numerical work in chapter 2. Li's 2012 paper[59], "Ideal strength and phonon instability in single-layer MoS_2", presents density functional theory (DFT) results of stress as a function of different strain states. The work of Cooper *et al.*[13], "Nonlinear elastic behavior of two-dimensional molybdenum disulfide", performs the same DFT calculations as part of an investigation into the nonlinear elastic properties of MoS_2. Some of the DFT results of Li are substantially different from our recently published work[13]. While both papers agree on states of equibiaxial stress, there is substantial disagreement on states of uniaxial tensile stress. In this comment we show that our DFT computations are properly executed and consistent across three different DFT codes, including the one used by Li[59]. This work is currently under review by *Physical Review B*.

Chapter 4 extends the numerical work of chapter 2 to determine the strength of polycrystalline graphene films created through chemical vapor deposition. Pristine graphene is the strongest material ever measured. However, large-area graphene films produced by chemical-vapor-deposition (CVD) are polycrystalline and thus contain grain boundaries that can potentially weaken the material. We combine structural characterization by transmission-electron-microscopy (TEM) with nanoindentation to study the mechanical properties of CVD-graphene films with different grain sizes. We show that the elastic stiffness of CVD-graphene is identical to that of pristine graphene if postprocessing steps avoid damage or rippling. Its strength is only slightly reduced despite the existence of grain boundaries. Indentation tests directly on grain boundaries confirm that they are almost as strong as pristine. Graphene films consisting entirely of well-stitched grain boundaries can retain ultra-high strength critical for a large variety of applications such as flexible electronics and strengthening components. This work was published in *Science* in May 2013.

The final study of this thesis in chapter 5 employs nanoindentation and finite element analysis to investigate the viscoelastic properties of polydimethylsiloxane microfilms su-

bject to electron beam irradiation. Polydimethylsiloxane (PDMS) is a common substrate for microfluidic devices and for biological studies. The mechanical properties of PDMS can be tailored to suit a variety of needs by altering the amount of accelerating agent during crosslinking, changing the thermal history of curing the polymer, or irradiation to induce cross-linking. The effects of thermal history and accelerator on mechanical properties has been investigated by a variety of tests, but the effects of radiation on mechanical properties are still unknown. Herein, we describe a method of nanoindentation and finite element model-based analysis to determine the viscoelastic properties of microfilms of PDMS exposed to electron beam irradiation. This work is currently under review in the *Journal of Materials Research*.

The nonlinear elastic model used in chapters 2-4 employs *ab initio* calculations so it does not include any empirical parameters to tune to experimental measurements. The nanoindentation results serve as a means of validating the numerical approximations of density functional theory. The nonlinear elasticity theory depends only upon the existence of a continuous strain-energy density function. Molecular dynamic simulations would also provide a means of reproducing *ab initio* strain-energy density predictions, but these simulations are time-dependent and limited to time steps of ≈ 1 femtosecond [104]. By employing standard finite element analysis solutions, it is possible to calculate quasi-static or time-dependent mechanical response of micromechanical structures that would require millions to billions of atoms in a standard molecular dynamics simulation. The simulations performed herein of 1 μm-graphene membranes would would consist of approximately 26 million carbon atoms and a time scale on the order of 1 second. A numerical calculation involving this many bodies would be computationally intense even for some of the world's largest supercomputers. These numerical calculations allow one to predict longer time scale experiments and bulk deformation response using parameters derived from first-principles results.

Chapter 5 provides a framework for determining mechanical properties of inhomogenous microfilms by fitting finite element analysis results to experimental data points. Unlike chapters 2-5, the mechanical properties used in the finite element analysis are

empirically determined. In this respect, the analysis and experiment lend insight into bounds on the mechanical properties based upon experimental observations, as opposed to validation of a theory based upon experimental results in chapters 2-4.

Inhomogeneous microfilms are common in biological tissues and are becoming more widespread in NEMS and MEMS devices as flexible electronics become more widespread [87, 118]. It is imperitive to develop experimental methods for determining mechanical properties and strain states for these inhomogeneous microfilms.

Chapter 2

Investigation of Nonlinear Elastic Properties of MoS$_2$

2.1 Introduction

Two-dimensional materials have recently become an area of increased research focus, despite their long being considered thermodynamically unstable [78]. The experimental significance of 2D materials was first revealed in 2004 when the electrical properties of graphite crystals limited to only a few atoms thick were probed [71]. These 2D crystals were obtained via the clever and simple mechanical exfoliation method. Since this groundbreaking study, graphene and other 2D materials have been studied in areas of basic research such as electronics, optics and mechanics [22, 40, 58, 62, 70, 72].

Two-dimensional materials serve as outstanding testbeds for fundamental studies of mechanical properties under extreme strains [58]. They can be fabricated in a pristine condition essentially free of defects which enables them to achieve extreme tensile strain states prior to fracture or void nucleation. The mechanical flexibility of 2D materials allows them to conform to a surface and adhere to it via van der Waals interactions, thus simplifying the boundary conditions on a 2D material during mechanical characterization [58]. In addition, the relatively small number of atoms per unit cell in known 2D materials offer the opportunity to use first-principles and molecular dynamics computational

methods [111]. Finally, the 2D geometry restricts the possible deformation states which renders higher-order non-linear continuum elasticity formulations sufficiently tractable to combine with the atomistic methods to formulate multi-length scale models that can be readily incorporated into standard finite element analysis formulations [111, 113]. Most of these previous studies concentrated on monatomically-thin graphene, which is a single close-packed atomic plane of a single component (i.e. carbon), but other more general 2D materials can be produced by mechanical exfoliation [5, 68, 72, 85, 94, 95].

In the current study, we extend these methods to to study 2D molybdenum disulfide, which is a multi-component and multi-atomic layer system. Molybdenum disulfide is a layered transition metal dichalcogenide (LTMD) composed of layers of molybdenum atoms sandwiched between sulfur atoms, with each molybdenum atom ionically bonded to six sulfur atom as seen in Figure 2.1. Multiple MoS_2 layers are held together in the bulk material through van der Waals interactions, so the MoS_2 monolayers are easily cleaved.
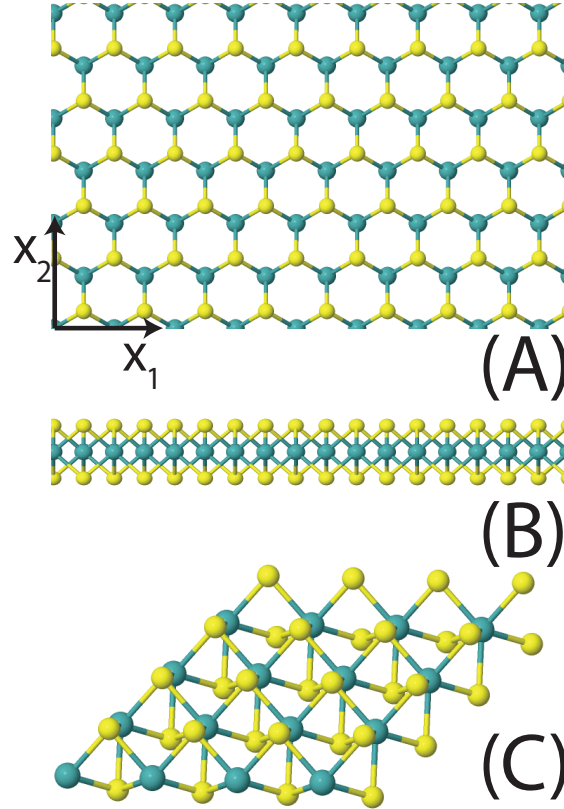
Figure 2.1: Atomic structure of monolayer MoS_2. The green and yellow spheres represent Mo and S atoms, respectively: (A) top view of the atomic structure; (B) side view of MoS_2 to highlight the out-of-plane sulfur atoms; and, (C) oblique view of 4x4 unit cells.

Molybdenum disulfide has been used as a solid lubricant for centuries and was studied as a material for detecting and rectifying radio signals in the 1950s [45]. Bulk MoS_2 has a hardness of 1–1.5 on the Mohs scale and exhibits excellent lubrication in high vacuum or under atmospheric conditions [45]. A study on bundles of MoS_2 nanotubes reveals a Young's modulus of 120 GPa with an inter-tube shear modulus of 160±30 MPa [49]. Bulk MoS_2 is an indirect gap semiconductor with a band gap of 1.2 eV, but by reducing the number of layers one can modify the band structure and create a direct gap semiconductor [43, 56, 57, 62, 85, 98]. Recently, monolayers of MoS_2 have been investigated as materials for microelectromechanical systems (MEMS) and nanoelectromechanical systems (NEMS) devices [49, 62, 72, 85]. The low power dissipation of MoS_2 direct gap semiconductors and its low cost make it an ideal candidate for flexible electronic applications. Studies have investigated the crystal structure and electrical properties

[42, 43, 45, 57, 62, 70, 72, 85, 94, 98]. Finally, the elastic properties of 2D MoS_2 have been investigated to characterize the Young's modulus and breaking strength [5]. However a more complete understanding of the mechanical properties of 2D MoS_2 is necessary to be able to predict its response upon incorporation into MEMS and NEMS devices.

The thickness of a 2D material is indeterminate because its out-of-plane electron configuration may change as a function of deformation state. Hence, stress, σ, and elastic moduli such as Young's modulus, E, are defined intrinsically as force per length rather than force per area. For purposes of comparison to 3D materials, the derived 3D quantities of stress and elastic moduli of a 2D material can be determined as $\sigma^{3D} = \sigma/t$ and $E^{3D} = E/t$, respectively, where t is an assumed thickness of the 2D materials. Herein we assume t = 0.615 nm as a representative thickness of 2D MoS_2, which is the interlayer spacing between layers of MoS_2 in the bulk material)[45]. Unless explicitly expressed otherwise with a superscript 3D, we assume all stress and moduli are 2D quantities.

The overall goal of this study is to determine the non-linear elastic properties of single layer MoS_2. First we derive a thermodynamically rigorous continuum elastic constitutive model of the non-linear elastic response of MoS_2 via a Taylor series expansion of the elastic strain energy density potential. We then use density functional theory (DFT) to calculate the elastic response of MoS_2 for several in-plane deformation states of uniaxial strain as well as biaxial strain. The magnitude of the applied strains ranges from infinitesimal to finite deformations beyond that corresponding to the intrinsic (i.e. maximum) stress. All components of the stiffness tensors of the higher-order elastic constitutive model are determined by fitting the continuum model to the stress vs. strain results of the uniaxial strain deformation states studied by DFT calculations. We use the crystal symmetry of 2D MoS_2 to determine the number of independent elastic constants for the continuum model. To verify the internal consistency of the higher order continuum theory, we calculate the elastic response with DFT of MoS_2 under a condition of uniaxial stress and demonstrate that the continuum model—fit only to the uniaxial strain DFT results— accurately predicts the DFT results in uniaxial stress. To validate the model, we use AFM nanoindentation to determine the force-displacement response as well as the force

required to rupture a monolayer MoS$_2$ film suspended over open circular holes. The results of a detailed finite element analysis (FEA) of the indentation experiments using the non-linear elastic continuum formulation are consistent with the experimental measurements to within experimental uncertainty, thus validating the model.

2.2 Non-linear Elastic Constitutive Model

Figure 2.2 shows the undeformed unit cell of monolayer MoS$_2$ described by two lattice vectors $\mathbf{a}_i$ (i=1,2). Unit vectors in the x_1- and x_2-directions relative to Figure 2.2 are denoted as $\hat{\mathbf{e}}_1$ and $\hat{\mathbf{e}}_2$, respectively, and $\mathbf{a}_1 = a_1\hat{\mathbf{e}}_1$ and $\mathbf{a}_2 = a_2(\frac{1}{2}\hat{\mathbf{e}}_1 + \frac{\sqrt{3}}{2}\hat{\mathbf{e}}_2)$. As will be discussed below, the magnitudes of the lattice vectors are $a_1 = a_2 = 3.16$Å in the undeformed reference configuration.

A macroscopic homogeneous in-plane deformation of the 2D crystal results in deformation of the lattice vectors $\mathbf{a}'_i = \mathbf{F}\mathbf{a}_i$ where $\mathbf{F}$ is the deformation gradient tensor and $\mathbf{a}'_i$ are the deformed lattice vectors. Writing the Lagrangian strain tensor as $\boldsymbol{\eta} = \frac{1}{2}\left(\mathbf{F}^{\mathbf{T}}\mathbf{F} - \mathbf{I}\right)$ where $\mathbf{I}$ is the identity tensor, the strain energy density potential has the functional form $\boldsymbol{\Phi} = \boldsymbol{\Phi}\left(\boldsymbol{\eta}\right)$, which quantifies the elastic strain energy per unit reference area of the undeformed MoS$_2$ [111].
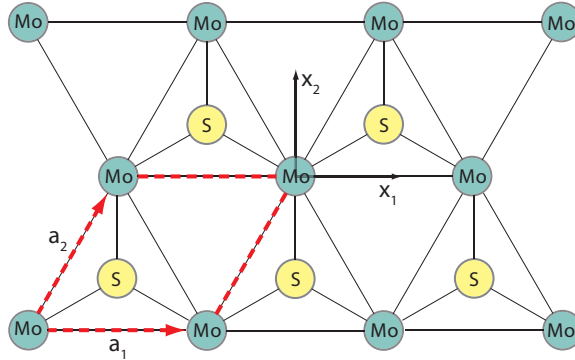
Figure 2.2: Unit cell of monolayer MoS$_2$. The axes are labeled by the black arrows and the unit cell is contained in the dashed red box. Atoms of S lie both above and below plane of the Mo atoms.

The elastic strain energy density potential can be expressed as a Taylor series expan-

sion in powers of strain as

$$\Phi = \frac{1}{2!}C_{ijkl}\eta_{ij}\eta_{kl} + \frac{1}{3!}C_{ijklmn}\eta_{ij}\eta_{kl}\eta_{mn} + \frac{1}{4!}C_{ijklmnop}\eta_{ij}\eta_{kl}\eta_{mn}\eta_{op}$$
$$+ \frac{1}{5!}C_{ijklmnopqr}\eta_{ij}\eta_{kl}\eta_{mn}\eta_{op}\eta_{qr} + ... \tag{2.1}$$

where C_{ijkl}, C_{ijklmn}, $C_{ijklmnop}$, and $C_{ijklmnopqr}$ are the second-, third-, fourth- and fifth-order stiffness tensors, respectively [111]; the summation convention is adopted for repeating indices and summation for lower case indices runs from 1 to 3. The quadratic term in strain suffices to describe a linear elastic material, so the higher-order terms are necessary to describe the non-linear response. The second Piola-Kirchhoff stress tensor, Σ_{ij}, defined in terms of its work conjugate Lagrangian strain is calculated by taking $\partial\Phi/\partial\eta_{ij}$ to obtain

$$\Sigma_{ij} = C_{ijkl}\eta_{kl} + \frac{1}{2!}C_{ijklmn}\eta_{kl}\eta_{mn} + \frac{1}{3!}C_{ijklmnop}\eta_{kl}\eta_{mn}\eta_{op} + \frac{1}{4!}C_{ijklmnopqr}\eta_{kl}\eta_{mn}\eta_{op}\eta_{qr} + ... \tag{2.2}$$

Upon adopting the Voigt notation [73], the stress tensor can be expressed as

$$\Sigma_I = C_{IJ}\eta_J + \frac{1}{2!}C_{IJK}\eta_J\eta_K + \frac{1}{3!}C_{IJKL}\eta_J\eta_K\eta_L + \frac{1}{4!}C_{IJKLM}\eta_J\eta_K\eta_L\eta_M + ... \tag{2.3}$$

where the lower case indices transform to Voigt indices in upper case letters as 11→1, 22→2, 33→3, 23→4, 13→5, and 12→6; the summation convention still holds and summation of upper case indices ranges from 1 to 6. The components of C_{IJ} are the second-order elastic constants (SOEC), those of C_{IJK} are the third-order elastic constants (TOEC), those of C_{IJKL} are the fourth-order elastic constants (FOEC), and those of C_{IJKLM} are the fifth-order elastic constants (FFOEC).

A general anisotropic elastic solid has 21 independent components in the SOEC, 56 in the TOEC, 126 in the FOEC and 252 in the FFOEC. The deformation state of a 2D material can be approximated as being solely an in-plane deformation state when the contribution of bending deformation to the strain energy density is negligible compared to that of in-plane deformation. This implies that only in-plane components (i.e. those with indices that include only I, J=1, 2 and 6 or i, j=1 and 2) of the stiffness tensors may be non-zero, and all out-of-plane components of the stiffness tensors are identically

zero. An undeformed 2D MoS$_2$ monolayer has point group D_{3h} which has a hexagonal crystal structure [68, 120]. Previous studies have shown that in-plane deformation states for this point group have two independents components of the SOEC, three independent components of the TOEC tensor, and four independent components of the FOEC tensor [21, 55]. We calculate that the FFOEC tensor has five independent non-zero components by imposing the symmetry elements of monolayer MoS$_2$ symmetry on the tensor based upon

$$C_{abcdefghij} = Q_{ka}Q_{lb}Q_{mc}Q_{nd}Q_{oe}C_{klmnopqrst}Q_{pf}Q_{qg}Q_{rh}Q_{si}Q_{tj} \qquad (2.4)$$

where $\mathbf{Q}$ refers to the transformation matrix associated with a symmetry element. Thus, monolayer MoS$_2$ requires a total of only 14 independent components of the stiffness tensors to describe finite in-plane deformations. The list of elastic constants is given in Table 2.1.

For general infinitesimal in-plane deformations, the elastic response is isotropic and linear with Young's modulus $E = \left(C_{11}^2 - C_{12}^2\right)/C_{11}$ and Poisson's ratio $\nu = C_{12}/C_{11}$ and the full linear-elastic response is

$$\begin{bmatrix} \Sigma_1 \\ \Sigma_2 \\ \Sigma_6 \end{bmatrix} = \begin{bmatrix} C_{11} & C_{12} & 0 \\ C_{12} & C_{11} & 0 \\ 0 & 0 & \frac{C_{11}-C_{12}}{2} \end{bmatrix} \begin{bmatrix} \eta_1 \\ \eta_2 \\ \eta_6 \end{bmatrix}. \qquad (2.5)$$

For general finite in-plane deformations, the elastic response is anisotropic and non-linear and the in-plane components of the second Piola-Kirchhoff tensor, Σ_1, Σ_2, and Σ_6, are given by

$$\Sigma_1 = C_{11}\eta_1 + C_{12}\eta_2 + \frac{1}{2}C_{111}\eta_1^2 + C_{112}\eta_1\eta_2 - \frac{1}{2}\left(\frac{1}{2}C_{111} + \frac{1}{4}C_{112} - \frac{3}{4}C_{222}\right)\eta_6^2$$

$$+ \frac{1}{2}\left(C_{111} + C_{112} - C_{222}\right)\eta_2^2 + \frac{1}{6}C_{1111}\eta_1^3 + \frac{1}{6}\left(\frac{1}{2}C_{1111} + C_{1112} - \frac{1}{2}C_{2222}\right)\eta_2^3$$

$$+ \frac{1}{2}C_{1112}\eta_1^2\eta_2 + \frac{1}{2}C_{1122}\eta_1\eta_2^2 + \frac{1}{2}\left(\frac{1}{12}C_{1111} + \frac{1}{6}C_{1112} - \frac{1}{4}C_{1122}\right)\eta_2\eta_6^2$$

$$- \frac{1}{2}\left(\frac{5}{24}C_{1111} + \frac{1}{6}C_{1112} - \frac{3}{8}C_{2222}\right)\eta_1\eta_6^2 + \frac{1}{6}C_{11112}\eta_1^3\eta_2 + \frac{1}{24}C_{11111}\eta_1^4$$

$$+ \frac{1}{24}C_{12222}\eta_2^4 + \frac{1}{4}C_{11122}\eta_1^2\eta_2^2 - \frac{1}{4}\left(\frac{1}{10}C_{11111} + \frac{1}{8}C_{11112} - \frac{9}{40}C_{22222}\right)\eta_1^2\eta_6^2 \qquad (2.6)$$

$$+ \frac{1}{24}\left(\frac{11}{80}C_{11111} + \frac{3}{8}C_{11112} + \frac{1}{8}C_{11122} - \frac{9}{16}C_{12222} - \frac{3}{40}C_{22222}\right)\eta_6^4$$

$$+ \frac{1}{6}\left(\frac{1}{2}C_{11111} + \frac{3}{2}C_{11112} + C_{11122} - \frac{3}{2}C_{12222} - \frac{1}{2}C_{22222}\right)\eta_1\eta_2^3$$

$$+ \frac{1}{4}\left(\frac{1}{15}C_{11111} + \frac{1}{8}C_{11112} - \frac{1}{6}C_{11122} - \frac{1}{40}C_{22222}\right)\eta_2^2\eta_6^2$$

$$- \frac{1}{2}\left(\frac{13}{120}C_{11111} + \frac{1}{4}C_{11112} + \frac{1}{6}C_{11122} - \frac{3}{8}C_{12222} - \frac{3}{20}C_{22222}\right)\eta_1\eta_2\eta_6^2$$

$$\Sigma_2 = C_{12}\eta_1 + C_{11}\eta_2 + \frac{1}{2}C_{112}\eta_1^2 + \frac{1}{2}C_{222}\eta_2^2 + \left(C_{111} + C_{112} - C_{222}\right)\eta_1\eta_2$$

$$- \frac{1}{2}\left(\frac{1}{4}C_{112} - \frac{1}{2}C_{111} + \frac{1}{4}C_{222}\right)\eta_6^2 + \frac{1}{6}C_{1112}\eta_1^3 + \frac{1}{6}C_{2222}\eta_2^3$$

$$+ \frac{1}{2}\left(\frac{1}{2}C_{1111} + C_{1112} - \frac{1}{2}C_{2222}\right)\eta_1\eta_2^2 + \frac{1}{2}C_{1122}\eta_1^2\eta_2$$

$$+ \frac{1}{2}\left(\frac{1}{12}C_{1111} + \frac{1}{6}C_{1112} - \frac{1}{4}C_{1122}\right)\eta_1\eta_6^2 - \frac{1}{2}\left(\frac{1}{6}C_{1112} - \frac{7}{24}C_{1111} + \frac{1}{8}C_{2222}\right)\eta_2\eta_6^2$$

$$- \frac{1}{4}\left(\frac{13}{120}C_{11111} + \frac{1}{4}C_{11112} + \frac{1}{6}C_{11122} - \frac{3}{8}C_{12222} - \frac{3}{20}C_{22222}\right)\eta_1^2\eta_6^2$$

$$+ \frac{1}{6}C_{11122}\eta_1^3\eta_2 + \frac{1}{6}C_{12222}\eta_1\eta_2^3 + \frac{1}{24}C_{11112}\eta_1^4 + \frac{1}{24}C_{22222}\eta_2^4$$

$$+ \frac{1}{2}\left(\frac{1}{15}C_{11111} + \frac{1}{8}C_{11112} - \frac{1}{6}C_{11122} - \frac{1}{40}C_{22222}\right)\eta_1\eta_2\eta_6^2$$

$$+ \frac{1}{24}\left(\frac{1}{8}C_{11122} - \frac{3}{8}C_{11112} - \frac{1}{80}C_{11111} + \frac{3}{16}C_{12222} + \frac{3}{40}C_{22222}\right)\eta_6^4$$

$$+ \frac{1}{4}\left(\frac{1}{2}C_{11111} + \frac{3}{2}C_{11112} + C_{11122} - \frac{3}{2}C_{12222} - \frac{1}{2}C_{22222}\right)\eta_1^2\eta_2^2$$

$$- \frac{1}{4}\left(\frac{1}{8}C_{12222} - \frac{9}{40}C_{11111} + \frac{1}{10}C_{22222}\right)\eta_2^2\eta_6^2$$

$$(2.7)$$

$$\Sigma_6 = \frac{1}{2}\left(C_{11} - C_{12}\right)\eta_6 + \frac{1}{4}\left(2C_{111} - C_{112} - C_{222}\right)\eta_2\eta_6 - \frac{1}{4}\left(2C_{111} + C_{112} - 3C_{222}\right)\eta_1\eta_6$$
$$+ \frac{1}{12}\left(C_{1111} + 2C_{1112} - 3C_{1122}\right)\eta_1\eta_2\eta_6 - \frac{1}{48}\left(5C_{1111} + 4C_{1112} - 9C_{2222}\right)\eta_1^2\eta_6$$
$$+ \frac{1}{48}\left(7C_{1111} - 4C_{1112} - 3C_{2222}\right)\eta_2^2\eta_6 - \frac{1}{96}\left(C_{1111} + 8C_{1112} - 6C_{1122} - 3C_{2222}\right)\eta_6^3$$
$$- \frac{1}{240}\left(4C_{11111} + 5C_{11112} - 9C_{22222}\right)\eta_1^3\eta_6 + \frac{1}{24}\left(9C_{11111} - 5C_{12222} - 4C_{22222}\right)\eta_2^3\eta_6$$
$$+ \frac{1}{240}\left(8C_{11111} + 15C_{11112} - 20C_{11122} - 3C_{22222}\right)\eta_1\eta_2^2\eta_6$$
$$- \frac{1}{480}\left(C_{11111} + 30C_{11112} - 10C_{11122} - 15C_{12222} - 6C_{22222}\right)\eta_2\eta_6^3$$
$$+ \frac{1}{480}\left(11C_{11111} + 30C_{11112} + 10C_{11122} - 45C_{12222} - 6C_{22222}\right)\eta_1\eta_6^3$$
$$- \frac{1}{240}\left(13C_{11111} + 30C_{11112} + 20C_{11122} - 45C_{12222} - 18C_{22222}\right)\eta_1^2\eta_2\eta_6$$

$$(2.8)$$

where η_1, η_2, and η_6 are the in-plane components of the Lagrangian strain tensor defined relative to the orientation of monolayer MoS_2 shown in Figure 2.2.

It is worth noting at this point that these elastic constants are not parameters used to describe an empirically observed relation between stress and strain. These constants are intrinsic elastic constants that describe the elastic energy stored in a material subjected to finite elastic deformation. All of the atoms maintain nearest neighbors resulting in an affine deformation even under high stress. The constants derived here are the minimum number of constants to describe the strain-energy density function for a two dimensional material with hexagonal group symmetry. The higher order constants have more obtuse interpretations than small strain elastic constants such as Young's modulus and Poisson ratio, but in principal the elastic constants can be directly measured through experimental methods. In contrast to other empirical models, the choice of elastic constants is determined through an analytic Taylor series expansion of the strain-energy density function and group theory. The stress-strain relations herein depend only upon the existence of a continuous potential during macroscopic homogeneous deformation of a crystal unit cell.

We now consider several special deformation states that simplify the expressions for the general non-linear in-plane elastic response which we will now refer to being in uniaxial strain. The elastic response of monolayer MoS_2 is calculated for these special states. With

reference to Figure 2.2, a state of uniaxial strain in the x_1-direction is characterized by $\eta_1 \geq 0$ and $\eta_2 = \eta_6 = 0$. The corresponding elastic response gives $\Sigma_1 \geq 0$, $\Sigma_2 \geq 0$, where Σ_2 is the lateral constraint stress for this configuration, which is the stress required to maintain zero strain in the lateral direction; symmetry dictates that $\Sigma_6 = 0$. Similarly, we consider a state of uniaxial strain in the x_2-direction. Finally, we consider a state of equibiaxial strain for which $\eta_1 = \eta_2 = \eta \geq 0$ and $\eta_6 = 0$ which results in $\Sigma_1 = \Sigma_2 \geq 0$ and $\Sigma_6 = 0$. The deformation gradient tensors for the three deformation states, respectively, are

$$\mathbf{F}_1 = \begin{bmatrix} \lambda_1 & 0 \\ 0 & 1 \end{bmatrix}, \quad \mathbf{F}_2 = \begin{bmatrix} 1 & 0 \\ 0 & \lambda_2 \end{bmatrix},$$

(2.9)

$$\mathbf{F}_{bi} = \begin{bmatrix} \lambda_{bi} & 0 \\ 0 & \lambda_{bi} \end{bmatrix}$$

where the stretch ratio, λ_1, is the ratio of the deformed length of the unit cell in the x_1-direction to the reference length, λ_2 is defined analogously for deformation in the x_2-direction, and for the equibiaxial case $\lambda_{bi} = \lambda_1 = \lambda_2$.

For uniaxial strain in the x_1-direction the general stress-strain response simplifies to

$$\Sigma_1 = C_{11}\eta_1 + \frac{1}{2}C_{111}\eta_1^2 + \frac{1}{6}C_{1111}\eta_1^3 + \frac{1}{24}C_{11111}\eta_1^4 \tag{2.10}$$

$$\Sigma_2 = C_{12}\eta_1 + \frac{1}{2}C_{112}\eta_1^2 + \frac{1}{6}C_{1112}\eta_1^3 + \frac{1}{24}C_{11112}\eta_1^4 \tag{2.11}$$

$$\Sigma_6 = 0\,. \tag{2.12}$$

For uniaxial strain in the x_2-direction there results

$$\Sigma_1 = C_{12}\eta_2 + \frac{1}{2}\left(C_{111} - C_{222} + C_{112}\right)\eta_2^2 + \frac{1}{12}\left(C_{1111} + 2C_{1112} - C_{2222}\right)\eta_2^3 + \frac{1}{24}C_{12222}\eta_2^4 \quad (2.13)$$

$$\Sigma_2 = C_{11}\eta_2 + \frac{1}{2}C_{222}\eta_2^2 + \frac{1}{6}C_{2222}\eta_2^3 + \frac{1}{24}C_{22222}\eta_2^4 \tag{2.14}$$

$$\Sigma_6 = 0\,. \tag{2.15}$$

For the biaxial strain state there results

16

$$\Sigma_1 = \Sigma_2$$
$$= (C_{11} + C_{12})\,\eta + \frac{1}{2}\,(2C_{111} - C_{222} + 3C_{112})\,\eta^2 + \frac{1}{6}\left(\frac{3}{2}C_{1111} + 4C_{1112} - \frac{1}{2}C_{2222} + 3C_{1122}\right)\eta^3$$
$$+ \frac{1}{24}\,(3C_{11111} + 10C_{11112} - 5C_{12222} + 10C_{11122} - 2C_{22222})\,\eta^4$$

$$\text{(2.16)}$$

$$\Sigma_6 = 0\,. \qquad\qquad\qquad\qquad (2.17)$$

It is significant to note that all fourteen elastic constants appear in the stress vs. strain constitutive relationships for the three special cases collectively. Thus, the values of the elastic constants can be determined by fitting to the stress vs. strain response as calculated from first principles calculations.

In addition, we consider the elastic behavior of MoS_2 under conditions of uniaxial stress as a means to verify the internal consistency of the higher-order continuum theory. Uniaxial stress in the x_1-direction is characterized by $\Sigma_1 \geq 0$, $\Sigma_2 = 0$ with $\eta_1 \geq 0$ and $\eta_2 \leq 0$ due to Poisson contraction. Uniaxial stress in the x_2-direction is defined analagously.

2.3   First Principles Calculations of Elastic Response

We use density functional theory (DFT) to calculate the elastic response for the three special deformation states. The DFT calculations are performed with the VASP software package [50–53, 80] using the projector augmented wave method and both the local density approximation (LDA)[82] and the generalized gradient approximation (GGA)[80, 81] at 0 K.

A unit cell of one molybdenum atom and two sulfur atoms is employed assuming a separation distance of 61.5 Åbetween MoS_2 monolayers. The k-point grid is $13 \times 13 \times 3$ with a cutoff energy of 500 eV. The undeformed equilibrium state is determined through an energy and stress minimization as a function of the in-plane lattice vector and out-of-plane sulfur atom heights. The equilibrium configuration is determined to be a spacing of 3.122 Åbetween molybdenum atoms and an out-of-plane distance of 1.557 Åbetween a plane of sulfur atoms and the intermediate plane of molybdenum atoms. These results are

Table 2.1: Independent Components of Stiffness Tensors

C_{IJ}	C_{IJK}	C_{IJKL}	C_{IJKLM}
C_{11}	C_{111}	C_{1111}	C_{11111}
C_{12}	C_{112}	C_{1112}	C_{11112}
$C_{66} = \frac{1}{2}\left(C_{11} - C_{12}\right)$	C_{222}	C_{1122}	C_{11122}
	$C_{116} = 0$	C_{2222}	C_{12222}
	$C_{126} = 0$	$C_{1126} = 0$	C_{22222}
	$C_{166} = \frac{1}{4}\left(3C_{222} - 2C_{111} - C_{112}\right)$	$C_{1166} = \frac{1}{24}\left(-5C_{1111} - 4C_{1112} + 9C_{2222}\right)$	$C_{11116} = 0$
	$C_{226} = 0$	$C_{1222} = \frac{1}{2}\left(C_{1111} + 2C_{1112} - C_{2222}\right)$	$C_{11126} = 0$
	$C_{266} = \frac{1}{4}\left(2C_{111} - C_{222} - C_{112}\right)$	$C_{1266} = 0$	$C_{11166} = \frac{1}{40}\left(-4C_{11111} - 5C_{11112} + 9C_{22222}\right)$
	$C_{122} = C_{111} + C_{112} - C_{222}$	$C_{1266} = \frac{1}{12}\left(C_{1111} + 2C_{1112} - 3C_{1122}\right)$	$C_{11222} = \frac{1}{2}\left(C_{11111} + 3C_{11112} + 2C_{11122} - 3C_{12222} - C_{22222}\right)$
	$C_{666} = 0$	C_{1666}	$C_{11226} = 0$
		$C_{2226} = 0$	$C_{11266} = \frac{-1}{120}\left(13C_{11111} + 30C_{11112} + 20C_{11122} - 45C_{12222} - 18C_{22222}\right)$
		$C_{2266} = \frac{1}{24}\left(7C_{1111} - 4C_{1112} - 3C_{2222}\right)$	$C_{11666} = 0$
		$C_{2666} = 0$	$C_{12226} = 0$
		$C_{6666} = \frac{1}{16}\left(-C_{1111} - 8C_{1112} + 6C_{1122} + 3C_{2222}\right)$	$C_{12266} = \frac{1}{120}\left(8C_{11111} + 15C_{11112} - 20C_{11122} - 3C_{22222}\right)$
			$C_{12666} = 0$
			$C_{16666} = \frac{1}{40}\left(9C_{11111} - 5C_{12222} - 4C_{22222}\right)$
			$C_{22226} = 0$
			$C_{22266} = \frac{1}{40}\left(9C_{11111} - 5C_{12222} - 4C_{22222}\right)$
			$C_{22666} = 0$
			$C_{26666} = \frac{1}{80}\left(-C_{11111} - 30C_{11112} + 10C_{11122} + 15C_{12222} + 6C_{22222}\right)$
			$C_{66666} = 0$

consistent with experimentally determined lattice spacing of 3.16 Åbetween Mo atoms and 1.59 Åout-of-plane height for S atoms in a bulk MoS_2 crystal [8]. The stress components computed in VASP are in terms of true stress, or Cauchy stress, $\boldsymbol{\sigma}$, in units of force per area on the cross-sectionl edges of the unit cell. For a 2D material it is appropriate to express the stress in terms of force per length of the edge; this is obtained from the product of the the stress components calculated from VASP and the interlayer spacing of 61.5 Å.

The relation between the true stress and second Piola-Kirchhoff (P-K) stress $\boldsymbol{\Sigma}$ is given as

$$\boldsymbol{\Sigma} = J\boldsymbol{F}^{-1}\boldsymbol{\sigma}\left(\boldsymbol{F}^{-1}\right)^T \tag{2.18}$$

where J is the determinant of the deformation gradient tensor $\mathbf{F}$ [15]. In this work, we did not explore the possibility of finite wave vector instabilities which might be relevant at large strains. For example, in graphene a phonon instability of the K-mode occurs for sufficiently large equibiaxial strain [63].

To calculate the elastic response of a given deformation state, the unit cell is determined according to the deformed lattice vectors $\mathbf{a}_i'$ which are functions of the applied $\mathbf{F}$. The molybdenum and sulfur atoms are relaxed in the strained unit cell into the minimum potential energy configuration both in and out of the plane. A series of simulations is performed for both uniaxial strain cases as well as the equibiaxial strain case, beginning with strains within the linear-elastic regime and finishing with strains beyond that corresponding to the intrinsic (i.e. maximum) stress.

The results of the VASP simulations are shown in Figure 2.3a where the second Piola-Kirchhoff stress is plotted as a function of the Lagrangian strain and in Figure 2.3b the true stress is plotted as a function of the true strain. True (i.e. Cauchy) stress is calculated based on equation 2.18 and the true strain is given as $\varepsilon = \ln(\lambda)$. The calculated DFT results are highlighted as symbols. The red symbols represent calculations for uniaxial strain in the x_1-direction, with the + and × symbols indicating the lateral constraint and normal stresses as a function of prescribed strain η, respectively. The green symbols represent calculations for uniaxial strain in the x_2-direction, with the □ and ◇ symbols

indicating the lateral constraint and normal stresses, respectively. The blue $\otimes$ symbols represent the equibiaxial stress ($\Sigma_1 = \Sigma_2$) in the x_1- and x_2-directions.

The values of the fourteen independent components of the stiffness tensors are determined by least-squares curve fitting of equations 2.10–2.17 to the corresponding DFT calculations. The results, shown as solid colored lines in Figure 2.3, demonstrate that the higher order continuum formulation accurately describes the calculated stress-strain response up to approximately 0.30 Lagrangian strain or 0.25 true strain. The resulting fourteen independent elastic constants for monolayer MoS_2 are tabulated in Table 2.2. For the linear-elastic regime at small strains, the Young's modulus is E^{2D}=129 N/m and the in-plane Poisson's ratio is $\nu = 0.29$.

A fifth order expansion of the strain energy density function captures the anisotropy of 2D MoS_2 and the elastic instability used to predict failure of the material. The appropriateness of the fifth order fit is verified by comparing the root-mean-square (RMS) deviation defined as $\sqrt{SSE/n}$, where SSE is the sum of squares error and n is the number of data points used in the fit. Comparing the RMS deviation for the 234 data points of stress and strain, a third order elastic constant expansion results in a RMS deviation of 1.404 N/m, a fourth order approximation results in 0.462 N/m, and the fifth order approximation results in a 0.145 N/m RMS deviation. The third and fourth order approximations cannot capture both the linear response and the peak stress at finite strains in the same fit. The third and fourth order fits underpredict the Young's modulus as 65 N/m and 104 N/m, respectively. The fifth order approximation captures the relevant behavior of 2D MoS_2 under tension including the linear-elastic response and the elastic instability used to predict fracture.

It is interesting to note that the anisotropy of MoS_2 is very prominent in Figure 2.3a comparing the resulting second Piola-Kirchhoff stresses as a result of uniaxial strains in the x_1- and x_2-directions. Along the x_1-direction, as defined in Figure 2.1, the second Piola-Kirchhoff lateral constraint stress becomes higher than the normal stress. The true stress measure, in Figure 2.3b, reveals that this phenomenon is a result of the reference area choice. In a system composed of one type of atom, such as graphene, this behavior

has not been observed [111].

(a)

(b)
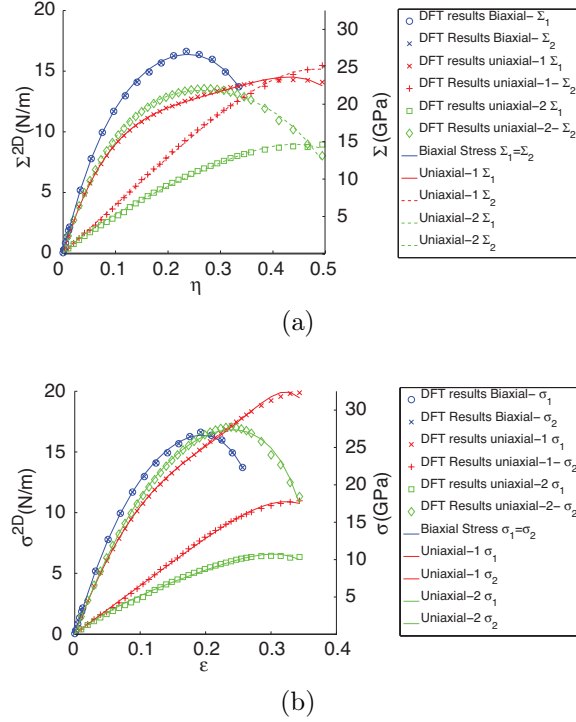
Figure 2.3: 2.3a is the least squares curve fit to DFT data using the LDA functional of three prescribed deformation states. Quantities are plotted in Second Piola-Kirchhoff stress and Lagrangian strain. Symbols depict calculated data and lines indicate least squares fits. 2.3b is the same data converted to true stress and true strain.

SOEC (N/m)	TOEC (N/m)	FOEC (N/m)	FFOEC (N/m)
$C_{11} = 140$	$C_{111} = -1300$	$C_{1111} = 8770$	$C_{11111} = -29830$
$C_{12} = 40$	$C_{112} = -1090$	$C_{1112} = 440$	$C_{11112} = -4340$
	$C_{222} = -30$	$C_{1122} = -230$	$C_{11122} = -230$
		$C_{2222} = 5870$	$C_{12222} = -8450$
			$C_{22222} = -18930$

Table 2.2: Non-zero independent elastic constants fit to the LDA functional DFT data of monolayer MoS_2 relating the second Piola-Kirchhoff stress tensor to the Lagrangian strain deformation state. The SOEC, TOEC, FOEC and FFOEC, second-, third-, fourth- and fifth-order elastic constants, respectively are tabulated.

The calculations are repeated using a projector augmented wave with a generalized gradient approximation (GGA), the Perdew-Burke-Ernzerhof (PBE), functional in VASP. The unit cell remains one molybdenum atom and two sulfur atoms and a separation distance of 61.5 Å between MoS_2 monolayers. The k-point grid remains $13 \times 13 \times 3$ with a cutoff energy of 500 eV. The undeformed equilibrium state is determined through an

energy and stress minimization as a function of the molybdenum atom spacing and out-of-plane sulfur atom heights. The equilibrium configuration is determined to be a spacing of 3.182 Å between molybdenum atoms and an out-of-plane distance of 1.563 Å between a plane of sulfur atoms and the intermediate plane of molybdenum atoms for the PBE functional. The resulting higher order elastic constants are shown in Table 2.3 and the graphs are shown in Figure 2.4.
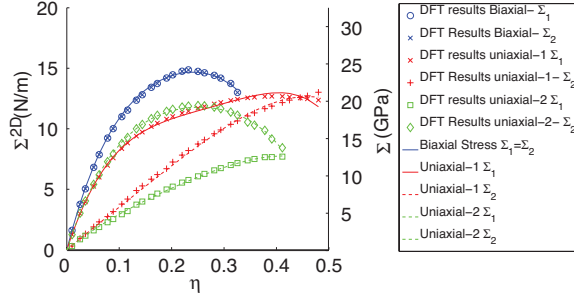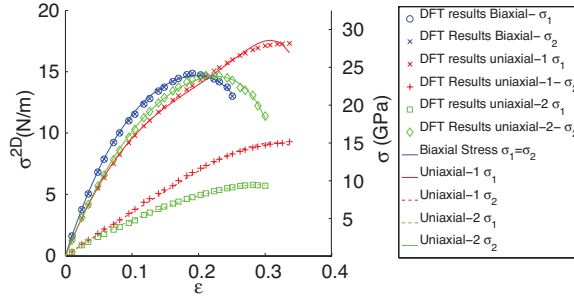
Figure 2.4: 2.4a is the least squares curve fit to DFT data using the PBE functional of three prescribed deformation states. Quantities are plotted in Second Piola-Kirchhoff stress and Lagrangian strain. Symbols depict calculated data and lines indicate least squares fits. 2.4b is the same data converted to true stress and true strain.

SOEC (N/m)	TOEC (N/m)	FOEC (N/m)	FFOEC (N/m)
$C_{11} = 130$	$C_{111} = -1200$	$C_{1111} = 7800$	$C_{11111} = -26460$
$C_{12} = 40$	$C_{112} = -1010$	$C_{1112} = 580$	$C_{11112} = -4200$
	$C_{222} = -60$	$C_{1122} = -50$	$C_{11122} = -800$
		$C_{2222} = 5760$	$C_{12222} = -6880$
			$C_{22222} = -21300$

Table 2.3: Non-zero independent elastic constants fit to the PBE functional DFT data of monolayer MoS_2 relating the second Piola-Kirchhoff stress tensor to the Lagrangian strain deformation state. The SOEC, TOEC, FOEC and FFOEC, second-, third-, fourth- and fifth-order elastic constants, respectively are tabulated.

The PBE functional results fit to the higher order nonlinear elastic constants predicts a Young's modulus of $E = 118$ N/m and a Poisson's ratio of $\nu = 0.31$. At strains above 20 % the difference in stress measures for LDA and PBE is approximately 15 %. The calculations with LDA predict an elastic instability at $\eta = 23.4\,\%$ and $\Sigma = 27\,N/m$, while the PBE calculations predict an elastic instability as $\eta = 23.2$ % and $\Sigma = 24$ N/m.

We verify in two ways that our calculations and constitutive model are correct and internally self-consistent. First we reproduce our VASP calculations of the elastic response under all five deformation states considered herein with both the Abinit and Quantum Espresso DFT software packages. The results from all three software packages are quantitively consistent with each other for the PBE approximation, thus verifying the DFT calculations. Second we demonstrate that the DFT calculations and the continuum constitutive model are internally self consistent, individually for the LDA and PBE approximations. To do so, we first calculated the elastic response for the equibiaxial and the two uniaxial strain deformation states using DFT. Then we determined the fourteen independent elastic constants of the continuum fifth order elastic constitutive description by fitting to the DFT results of the equibiaxial and the two uniaxial strain deformation states. We then predicted the elastic response under the two states of uniaxial stress using the continuum model. We then calculated the elastic response for the two states of uniaxial stress via DFT. The continuum predictions are compared to the DFT calculations in Figures 2.5a for the LDA approximation and 2.5b for the PBE approximation. There is a very good agreement between the predictions and the calculations, thus verifying the internal consistency of the multiscale atomistic (DFT) and continuum constitutive model. It bears emphasis that the fourteen elastic constants are determined by fitting to DFT results from only the equibiaxial and uniaxial strain states for each approximation; the DFT results for the two uniaxial stress deformation states were not used in the curve fitting process.

For completeness, we now discuss the details of the DFT calculation under uniaxial stress conditions. The uniaxial stress DFT calculations are achieved by relaxing the $\hat{\mathbf{e}}_2$-components of the $\mathbf{a}_1$ and $\mathbf{a}_2$ lattice vectors for uniaxial stress in the x_1-direction. The

uniaxial stress state in the x_2-direction is achieved analogously by relaxation of the $\hat{\mathbf{e}}_1$-components. Li[59] performs uniaxial stress calculations that are not consistent with our results. However, our results have been verified using three *ab initio* codes (ie. VASP, Abinit, and Quantum Espresso), and a direct comparison to Li's results will be made in a forthcoming publication [14].
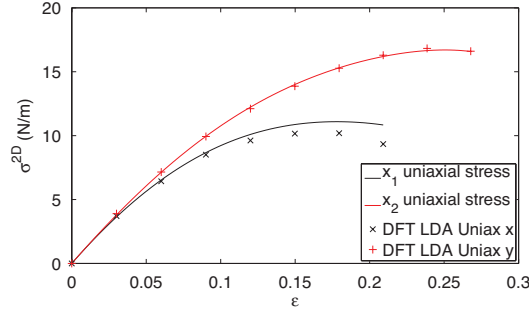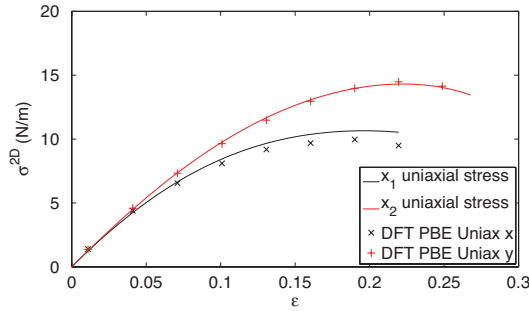
Figure 2.5: Plotted above are the uniaxial stress calculations based upon DFT with a LDA functional 2.5a and a PBE functional 2.5b. The + and × data points represent the data calculated for a uniaxial stress state in the x_1- and x_2-directions, respectively. The red and black lines represent the least squares curve fit prediction of the stress-strain curve for uniaxial stress in the x_1- and x_2-directions, respectively. The data is plotted in true stress and true strain.

2.4 Experimental Methods

Following the approach and procedures of Lee *et al.* [58], the specimens are fabricated on a silicon substrate with a 300 nm epilayer of SiO_2. We introduce an array of circular wells with 500 nm diameter and 500 nm depth, via reactive ion etching, into the substrate following patterning via electron beam lithography. Then, MoS_2 is mechanically exfoliated onto the substrate. The individual flakes of MoS_2, with sizes up to 4 μm by 8 μm, are

randomly distributed atop the substrate and are large enough to cover several adjacent wells.

The nanoindentation experiments performed in this study offer several advantages over mechanical tests performed on nanotube structures. First, the sample geometry is precisely defined and the 2D structure is less sensitive to material or substrate defects. The circular freestanding monolayers of MoS_2 are effectively clamped around the periphery via van der Waals interactions with the substrate, which serves to constrain both radial and out-of-plane displacements. Thus the boundary conditions are well-defined and repeatable, whereas it is much more difficult to obtain such boundary conditions when loading nanotube configurations.
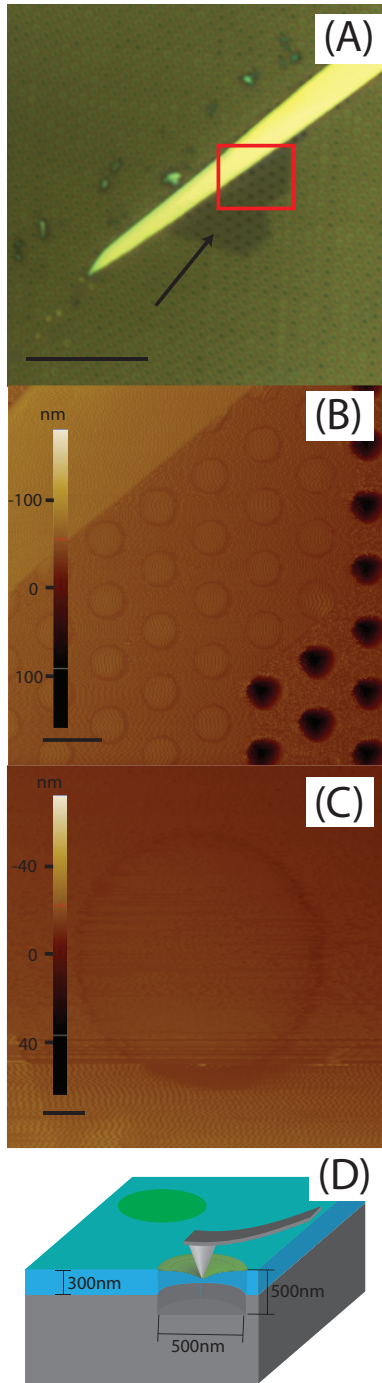
Figure 2.6: Suspended MoS$_2$ on SiO$_2$ substrate imaged via optical microscopy (A) and AFM (B) and (C). The arrow in image (A) points to a flake of monolayer MoS$_2$; (B) shows the AFM image of the area highlighted in red in (A); the scale bars in (A), (B), and (C) are 10 µm, 5 µm, and 100 nm, respectively; and, (D) shows the experimental set-up graphically.

We use optical microstopy to identify candidate monolayer MoS$_2$ sheets suspended above wells, as seen in Figure 2.6A. Then an AFM (XE-100, Park Systems) in non-contact mode confirms the monolayer thickness to be 0.615 nm [3]. Suspended monolayers are

imaged in non-contact mode to determine the center of the membrane. The monolayer films are then indented at their centers with the AFM to determine the force-displacement response as well as the breaking force.

The AFM tip is a diamond cube corner on a silicon cantilever fabricated by MicroStar Technologies; standard silicon AFM tips are not used because the load levels can cause fracture of the tip prior to rupture of the monolayer MoS_2. The tip radius, measured before and after indentation using a transmission electron microscope (TEM), is 26 nm. The AFM cantilever is calibrated against a reference cantilever for accurate determination of its stiffness [105]. Indentations are performed on twelve suspended membranes from one flake of MoS_2 that can be seen in Figure 2.6. Each monolayer MoS_2 membrane is loaded and unloaded several times at a prescribed AFM tip displacement rate of 1.25 µm/s. Eight of the membranes exhibit significant hysteresis of the force-displacement response, indicating that the van der Waals interactions are not sufficient to preclude slipping at the periphery of the suspended membranes; data from these membranes are not included in subsequent analysis. Four of the membranes exhibit negligible hysteresis. The depth of the indent load-unload cycles is increased in 30–50 nm increments until rupture of the membrane is recorded, characterized by the tip plunging through the membrane and a sudden diminution of the force. A typical set of data in Figure 2.7 show two loading-unloading curves in blue and green, demonstrating the negligible hysteresis. Subsequently in the red curve, the membrane is loaded to rupture shown by the × symbol. The average breaking force of the four membranes is 1500 nN with a standard deviation of 300 nN.
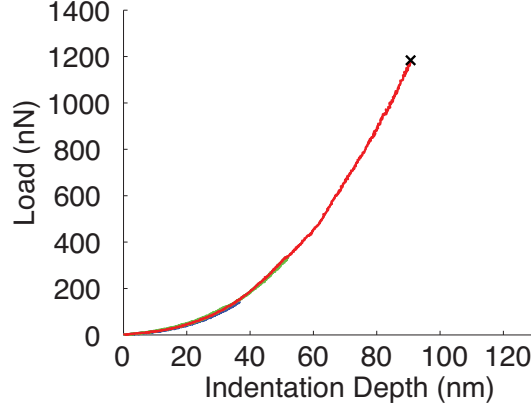
Figure 2.7: Typical loading-unloading curve for a monolayer MoS$_2$ membrane. The blue and green curves include both the loading and unloading data points. There is no evidence of hysteresis. The red curve ends in abrupt fracture of the membrane, marked by the $\times$ symbol.

The force-displacement data are analyzed to characterize the elastic response of monolayer MoS$_2$. A semi-empirical formula approximates the relationship between force and displacement for an axisymmetric membrane under a central point load as [58]

$$F = \sigma_0 \left(\pi a\right) \left(\frac{\delta}{a}\right) + E \left(q^3 a\right) \left(\frac{\delta}{a}\right)^3 \tag{2.19}$$

where F is the applied force on the AFM tip, δ is the load point deflection, a is the membrane radius, E and σ_0 are the 2D Young's modulus and prestress in the film, respectively, and $q = (1.05 - 0.15\nu - 0.16\nu^2)$, and $\nu = 0.29$ the Poisson's ratio. The prestress and Young's modulus are determined by fitting Equation 88 to the experimental force-displacement data. The resulting measure of stiffness is valid only as an estimate of the in-plane Young's modulus; it does not offer any insight into 3D mechanical behaviors such as bending stiffness. In this study, 26 loading curves yield an average value of $\bar{E} = 120$ N/m with a standard deviation of 30 N/m and an average prestress of $\bar{\sigma}_0 = 0.4$ N/m with a standard deviation of 0.2 N/m.

2.5 Experimental Validation

We now discuss results of a detailed finite element analysis (FEA) of the indentation of the circular monolayer MoS_2 membrane and compare the results to the experimental data. The FEA simulation employs the higher-order non-linear elastic constitutive behavior of Equations 4.5-4.10 as well as the elastic constants in Table 2.2 that have been implemented into a User Material (UMAT) subroutine [113] for use with the commercially available finite element program ABAQUS [97]. This implementation is valid for use in membrane elements, which implies that the bending stiffness of the MoS_2 is vanishingly small compared to the in-plane stiffness. This assumption is valid when the radius of curvature of the deformed MoS_2 monolayer is much greater than the distance between nearest atomic neighbors. Specifically for these simulations, the smallest radius of curvature in the MoS_2 is the 26 nm of the indenter tip and the interatomic distance is 3.16 Å.

The circular membrane of diameter 500 nm is modeled with 9575 four-node membrane elements and is clamped to inhibit displacements at its periphery and loaded at its center with a frictionless rigid sphere of radius 26 nm. An equibiaxial prestress is set to 0.42 N/m, the average measure of prestress from AFM nanoindentations. The simulation is performed in approximately 900 time increments equating to an average of 1.2 nm of indenter displacement per increment. The FEA formulation requires 3D stress and modulus measures as well as a well-defined membrane thickness, so we perform the computations using the derived 3D quantities. However we report the results in terms of the intrinsic 2D quantities.

Figure 2.8 shows the simulated force-displacement curve at the center of the membrane for both the LDA and PBE approximations, which are in good agreement with experimental results from AFM nanoindentations. The close agreement between the results from the finite element model based on first-principles data and the nanoindentation curve is a testament to the validity of the experimental and theoretical framework that comprise this study.

Figure 2.9 shows the details of the stress concentration in the MoS_2 monolayer under

the indenter tip. At very shallow indentation depths, the stress state is axisymmetric (cf. Figure 2.9A), consistent with elastic isotropy at small strains. At an intermediate indentation depth in Figure 2.9B, the stress state begins to develop a six-fold rotation symmetry, which becomes fully developed at large indentation depths of Figure 2.9C. Thus monolayer MoS_2 develops an elastic anisotropy with a six-fold rotation symmetry at finite strains of an approximate equibiaxial nature, consistent with the D_{3h} point group of the hexagonal lattice. The deformation state in the very center of the indented region experiences equibiaxial deformation, so that according to Figure 2.3a the LDA data, the peak stress the MoS_2 can withstand is 16.5 N/m a Lagrangian strain of about 0.23. At larger equibiaxial strains, the stress will decrease and the deformation state will be unstable because of the negative local tangent modulus leading to strain softening. Figure 2.9D shows the monolayer MoS_2 at the state when the stress in the very center has begun to decrease. The FEA simulation becomes unable to converge to equilibrium solutions at an indentation depth past 102 nm, where force on the indenter tip in the first-principles FEA model is 1490 nN for the LDA least squares fit and 1360 nN for the PBE least squares fit, well within the experimental uncertainty of the measurements. The 95% confidence interval for the experimental breaking force is 1350–1650 nN. A smaller degree of uncertainty in experimental measurements would lend insight into which approximation closer represents the mechanical properties of MoS_2.
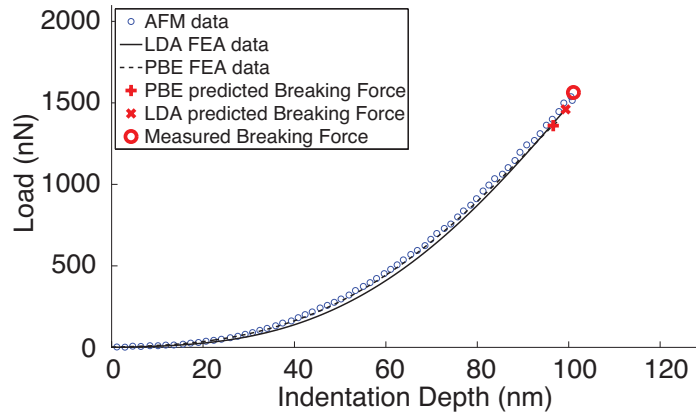
Figure 2.8: Comparison of the multiscale finite element models based on first principles data represented by the solid and dashed lines for LDA and PBE fits, respectively. The AFM data is represented by ∘ symbols. The point at which fracture occurs in the model is represented with a + symbol for the LDA fit and a × symbol for the PBE fit. The measured breaking force from AFM nanoindentatio is represented by the red ◯ symbol.
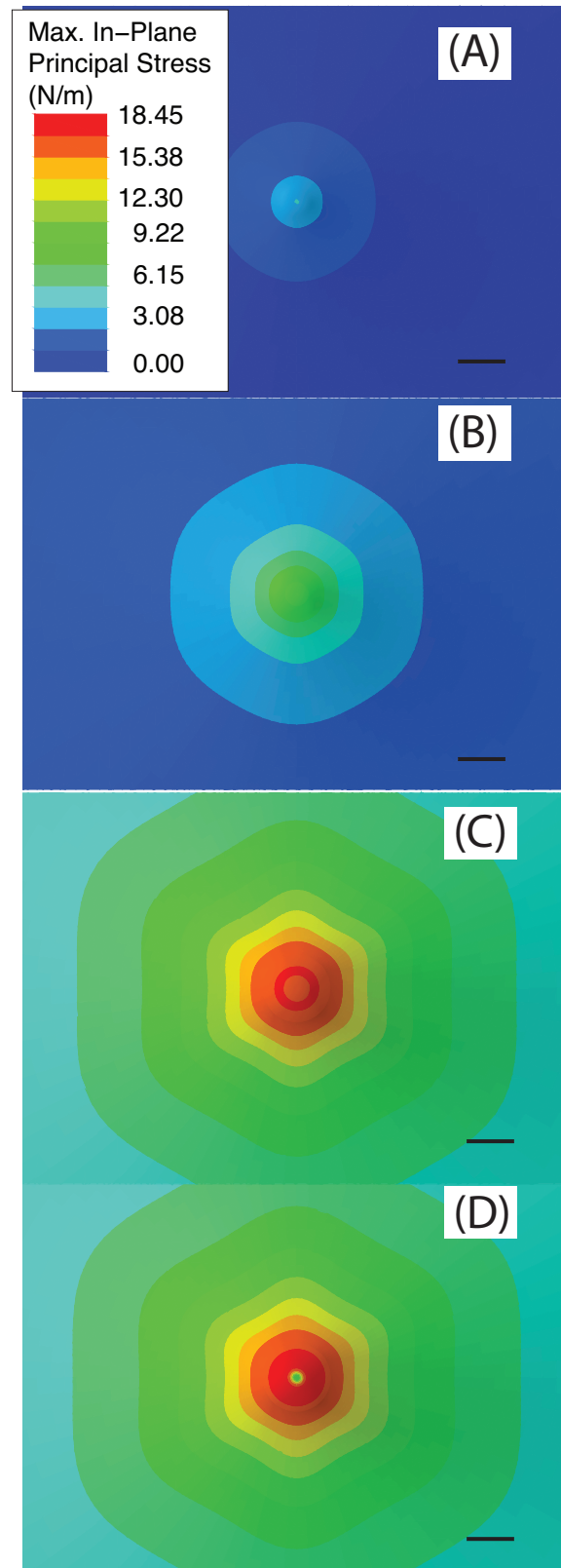
Figure 2.9: Abaqus FEA contours showing maximum principal stress at each integration point under the spherical rigid indenter at indentation depths of: (A) 6 nm; (B) 63 nm; (C) 98 nm; and, (D) 101 nm. The scale bars in (A)–(D) are 30 nm.

2.6 Conclusions

We have calculated using DFT the elastic response of monolayer MoS_2 for in-plane conditions of uniaxial strain and equibiaxial strain. The strains range from infinitesimal values to finite values beyond that corresponding to the intrinsic (i.e. maximum) stress. In addition, we derived the framework for a thermodynamically rigorous non-linear elastic constitutive relationship for arbitrary in-plane deformation by expanding the strain energy density in a Taylor series in powers of Lagrangian strain truncated after the fifth power. There are fourteen indendent components of the resulting stiffness tensors. The values of these components are determined by fitting to the DFT results. The resulting multiscale continuum constitutive relationship is non-linear and anisotropic, although the non-linearity does not manifest itself until a strain beyond about 0.05 and the anisotropy becomes significant only after a strain of about 0.1. AFM nanoindentation experiments performed on circular suspended monolayers of MoS_2 provide experimental evidence of intrinsic strength and in-plane Young's modulus. A detailed finite element model (FEM) of the experimental configuration was performed with ABAQUS along with a user material (UMAT) which incorporated the continuum constitutive model for use in membrane elements. The predicted force vs. displacement response as well as the force at rupture of the MoS_2 film correspond closely to the experimental values. This study bridges three main gaps that hinder understanding of material properties: DFT to FEM, experimental results to DFT, and the nanoscale to the microscale. In bridging these three gaps the experimental results validate the DFT calculations and the multiscale constitutive model.

Our results show that MoS_2 is a strong and flexible crystal. The maximum stress at the point of fracture is the intrinsic strength of the MoS_2, $\sigma_{int} = 16.5$ N/m as confirmed with finite element analysis implementation of the non-linear elastic constants. When assuming a monolayer thickness of t = 0.615 nm, the 3D intrinsic strength of MoS_2 is $\sigma_{int}^{3D} = 26.8$ GPa. The in-plane Young's modulus suitable for conditions of infinitesimal strains is E = 16.5 N/m, or $E^{3D} = 210$ GPa, which is consistent with the experimental results of Bertolazzi[5]. The in-plane Poisson's ratio suitable for conditions of infinitesimal strains as calculated using DFT is $\nu = 0.29$. It is interesting to note that Griffith [30]

predicts the intrinsic strength of a material to be $\sigma_{int} \approx E/9$, whereas experimental and DFT results suggest $\sigma_{int} \approx E/8$ in accordance with studies measuring the intrinsic strength of graphene [58].

Chapter 3

Comparison to T. Li

Two recent paper papers by Li[59] and by Cooper et al.[13] investigate the mechanical properties of two-dimensional (2D) MoS_2 under conditions of finite strain based upon Density Functional Theory (DFT) calculations. The predicted uniaxial stress at finite strains are different in the two papers. In particular, the uniaxial stress results in Figure 2 of Li[59] do not agree with the uniaxial stress results in Figure 5 of Cooper *et al.*[13]. Herein we show that the results of Cooper *et al.*[13] are correct. First, a brief introduction will be given to define precisely all quantities. Subsequently, we present results from three mainstream DFT packages, including the one used by Li[59]. We demonstrate that the results of Cooper *et al.*[13] are robust and that results from all three packages are consistent.

A uniaxial stress state is characterized by the application of stress in one direction while allowing the material to remain stress free in the other two principal directions. In a two dimensional material such as MoS_2, only two principal directions are considered, here assigned to be parallel to the zigzag direction (i.e. x_1-axis) and the armchair direction (i.e. x_2-axis). This same convention is used both in Figure 1 of Li[59] and Figures 1-2 of Cooper *et al.*[13]. A state of uniaxial tensile stress for 2D MoS_2 in the x_1-direction is defined by stress tensor components $\sigma_{11} > 0$ and $\sigma_{22} = 0$, with corresponding strain

tensor components of $\epsilon_{11} > 0$ and $\epsilon_{22} < 0$, given a positive Poisson ratio. The uniaxial tensile stress state in the x_2−direction is defined analogously. An equibiaxial stress state is defined as $\sigma_{11} = \sigma_{22}$ and $\epsilon_{11} = \epsilon_{22}$. The stress measure in a 2D material is defined as force normalized on a per unit length basis. Herein we express the stress as a derived 3D quantity by normalizing the 2D stress by an effective thickness of the 2D material. We report stress as a 3D quantity to facilitate comparison with Li's[59] results. Thus, engineering stress is defined as $\sigma_{eng} = F/A_o$ where F is the current force and A_o is the reference cross-sectional area. The corresponding engineering strain is defined as $\epsilon_{eng} = (L - L_o)/L_o$, where L is the current length, and L_o is the original length. True stress is defined as $\sigma_{true} = F/A$, where A is the current area and is typically plotted against true strain defined as $\epsilon_{true} = \log{(L/L_o)}$.

Li[59] uses the Quantum Espresso density functional theory (DFT) computational package to calculate two uniaxial stress states for 2D MoS_2 (in the zigzag and armchair directions) as well as the equibiaxial stress state, taking the MoS_2 thickness to be 0.6145 nm. The stress measure is erroneously reported to be engineering stress, but the results are in true stress (personal communication, August 29, 2012), while the strain measure is engineering strain. Here we use three different DFT packages (VASP[50–53], Quantum Espresso[25], and Abinit[27]) to calculate the mechanical response of 2D MoS_2 under the same stress states, taking the thickness to be 0.615 nm (the difference in stress arising from assuming a thickness which is 0.0005 nm greater is not perceptible on our plots).

The results of the DFT simulation are expected to be very similar, though there may be small discrepancies due to differences in the nature and degree of discretization of the Kohn-Sham equation (e.g. K-points, plane-wave cutoff, etc), treatment of the core electrons (ie. psuedopotential choice), and convergence criteria. In this comment, all three codes utilize the generalized gradient approximation (GGA) of Perdew, Burke, and Ernzerhof[80, 81] for the exchange-correlation functional.

Our VASP calculations employs the projector augmented wave method[7, 54] and the plane wave cuttoff was chosen to be 420 eV, which was found to be converged. The charge

self-consistency is terminated when changes in the total energy are less than 10^{-4} eV and structural minimization is terminated when changes in the energy are less than 10^{-3} eV. A k-point grid of $15 \times 15 \times 2$ was used. When computing the x_1-direction uniaxial stress state the x_2-components of the two lattice vectors is varied until $\mid \sigma_{22} \mid \leq 0.01$ GPa. The x_2-direction uniaxial stress state is solved analogously. The unstrained unit cell in VASP is found to have dimensions $a_1 = a_2 = 3.183$ (unit cell shown in Figure 1 of Li[59] and Figure 2 of Cooper *et al.*[13]) with an out-of-plane sulfur ion height of 1.564 .

In both Quantum Espresso and Abinit, most aspects of the simulations were equivalent. Trouiller-Martins pseudopotentials were used in both codes[106]. A plane wave cutoff of 420 eV was used in Abinit while 1361 eV was used in Quantum Espresso, with both respective values giving converged solutions. The primitive unit cell is doubled to create orthogonal lattice vectors. This ensures that only the e_2-component of the second lattice vector need be varied to ensure $\mid \sigma_{22} \mid \leq 0.01$ GPa for uniaxial stress in the x_1-direction as required by the minimization algorithms within these codes. The biaxial stress state is achieved by applying equal strains in the x_1- and x_2-directions. A k-point grid of $10 \times 10 \times 1$ was used. In Quantum Espresso, the self-consistency is terminated when changes in the total energy are less than 13.6×10^{-8} eV and the structural minimization is terminated when the force is less than 2.571×10^{-2} eV/Å. In Abinit, self-consistency was performed such that changes in the total energy are less than 27.2×10^{-7} eV and the structural minimization is terminated when both the force is less than 2.571×10^{-3} eV/Å and the change in energy is less than 13.6×10^{-4} eV between structural change steps . In Quantum Espresso, the unstrained unit cell is found to be $a_1 = 3.187$ Å and $a_2 = 5.521$ with an out-of-plane sulfur ion height of 1.574 Å. The Abinit unstrained unit cell is determined to be $a_1 = 3.185$ Å and $a_2 = 5.517$ with an out-of-plane sulfur ion height of 1.574 Å.

Our results from the three DFT packages are compared in Figure 3.1. In general, our results are within sufficient agreement. Abinit and Quantum Espresso use the same type of pseudopotential and are therefore nearly indistinguishable in most calculations. Our VASP calculations result in a slightly smaller sulfur height, as seen in Figure 3.1d.

All codes converge to the same stress until the point of elastic instability as seen in Figures 3.1a-3.1c. The only appreciable difference is a $\approx 5\%$ difference developing in our VASP results relative to Abinit/Quantum-Espresso in the x_2-direction for strains $>20\%$. We pressume that this difference can be attributed to the differences in the PAW approach versus the Trouiller-Martins psuedopotential as substantial checks were performed on k-point, plane-wave cuttoff, and convergence criteria in this region. In summary, there are no major differences among our calculations with the three different DFT codes.
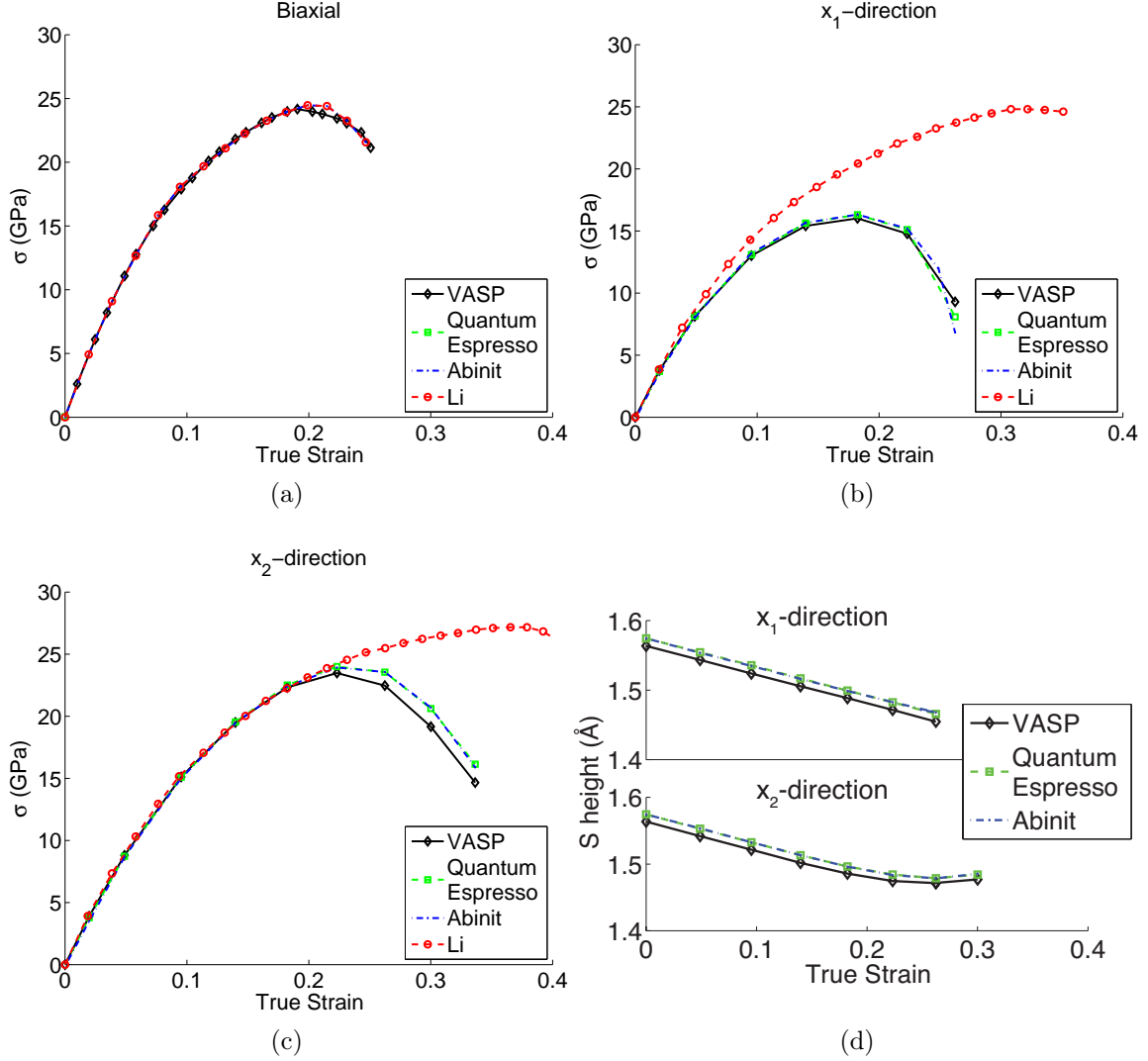
Figure 3.1: 3.1a is the biaxial stress state calculated with VASP, Quantum Espresso, and Abinit. 3.1b and 3.1c are the uniaxial stress states in the x_1- and x_2-directions, respectively, calculated with the same three DFT codes. The results of Li's[59] uniaxial stress DFT calculations–indicated by red ∘'s–are shown for comparison. There is a qualitative and quantitave agreement between Li and the calculations of Cooper *et al.* for a biaxial strain state in 3.1a, but there is qualitative disagreement in the x_1- and x_2-directions as seen in 3.1b-3.1c. 3.1d shows the calculated sulfur height as a function of strain for the three DFT codes for the uniaxial stress in the x_1- and x_2-directions in the upper and lower axes, respectively.

The uniaxial stress states calculated by Li[59] are not consistent with that of Cooper *et al.*[13]. Li uses the Quantum Espresso code with the generalized gradient approximation of Perdew, Burke, and Ernzerhof, along with Trouiller-Martins psuedopotentials[59] and a plane wave cuttoff of 100 Ry (ie. 1360.57eV). Therefore, there should not be any substantial deviation. Figures 3.1a-3.1c show the direct comparison of the two calcula-

tions. The biaxial stress calculations shown in Figure 3.1a agree both qualitatively and quantitatively, but there is a qualitative disagreement between the two sets of calculations for the x_1- and x_2-direction as seen in Figures 3.1b-3.1c uniaxial stress calculations. We have verified our calculations across three DFT packages and conclude that there is a discrepency in the work of Li[59].

Chapter 4

Mechanical Properties and Breaking behaviors of Grains and Grain Boundaries in Chemical Vapor Deposited Graphene

In bulk three-dimensional (3D) materials, the inevitable presence of bulk and surface defects limits the tensile strength to a value that typically falls well short of the intrinsic strength predicted for homogeneous tensile cleavage [66]. Low-dimensional materials such as two dimensional (2D) graphene or quasi-one-dimensional (1D) carbon nanotubes can achieve record strength in part because of the lack of surface defects that often initiate fracture in 3D materials. However, utilizing the ultrahigh strength of low-dimensional materials on the macro-scale remains an open challenge, both from a technological perspective and as a matter of fundamental interest. At sufficiently large scales, all materials will contain lattice defects, and the effects of such defects should be magnified in low-dimensional materials, due to a reduction in the number of dimensions in which a material can receive structural support: in the limit of a 1D atomic chain, even a single vacancy will reduce the tensile strength to zero. Moreover, the same lack of surface-bulk distinction that eliminates surface defects in low dimensional materials also renders them extremely

sensitive to damage during processing.

We have previously used nanoindentation of freely suspended films in an atomic force microscope (AFM) to show that graphene isolated by mechanical exfoliation is the strongest known material and in its defect-free pristine state can achieve its intrinsic strength before succumbing to rupture [58]. However, graphene produced by scalable methods–such as Chemical-Vapor-Deposition (CVD)–produces graphene with various defects, especially grain boundaries [39, 48, 88, 107, 121]. It is of fundamental importance to understand how the nature and presence of such defects will degrade the mechanical properties. Recent theoretical studies have argued that graphene grain boundaries can be as strong as the pristine lattice, depending on their exact configuration, such as tilt angle [28] and arrangement of defects [114]. On the other hand, nanoindentation tests have shown that both the elastic stiffness and fracture strength of CVD-graphene with μm-scale grain size are much smaller than those of defect-free pristine graphene and that fracture occurs at grain boundaries [39, 88]. However, continued progress in development of techniques for processing graphene motivates re-examination of this question from an experimental standpoint. Indeed, we find here (see Chap. 4.1) that techniques used in earlier studies, which were standard practice at the time and remain widely used, significantly degrade the strength of graphene. In this work we employ new processing techniques that leave graphene's strength intact. We use a commercial nanoindenter to test a large number of samples for statistical analysis, and combine nanoindentation and TEM characterization to test individual grain boundaries. The data are analyzed using a multiscale model based on density functional theory and experimentally validated for pristine graphene, as is done in 2 for two dimensional molybdenum disulfide.

Two types of graphene were grown on copper foil: continuous graphene films with small grains (SG), and isolated single-crystals with large grains (LG) (see Methods in Supplementary Materials). Dark-field TEM (DF-TEM) imaging [39] was used to map the grain structure of the graphene films (Fig. 4.1A and C); each false-color area indicates a distinct crystal orientation from the selected area electron diffraction (SAED) patterns of Figs. 4.1B and 1D. These patterns confirm that the SG graphene is similar to the

42
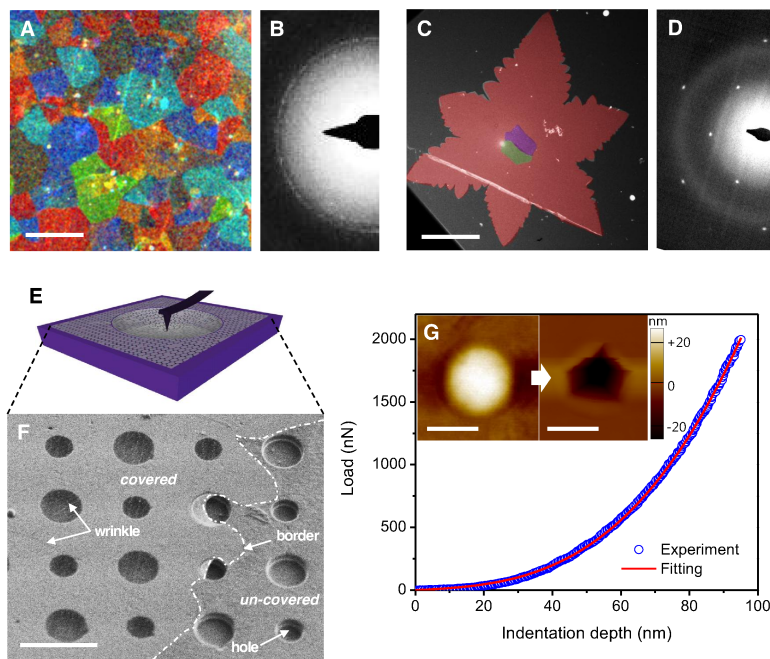
Figure 4.1: Materials and testing methods. (A, C) False-color DF-TEM images and (B, D) SAED patterns of SG graphene and LG graphene films. (E) Schematic of the suspended graphene film over hole for AFM nanoindentation tests. (F) SEM images of the suspended LG graphene film over holes. The border of the graphene-covered area is indicated by a dashed line for visualization. Wrinkles often present in the transferred graphene can be seen. (G) Force-displacement curve of the SG graphene film in AFM nanoindentation. The red line is a fitting curve to Eq. 2 of Ref. [58]. The inset shows the AFM topology images of the suspended SG graphene film before and after fracture. Scale bars: 3 µm in (A, F), 20 µm in (C), 1 µm in (G).

films studied previously [39, 88, 107]: it is polycrystalline with $1-5$ µm grains that are stitched at well-defined grain boundaries, that have been observed to consist of pentagon and heptagon carbon rings without any other defects such as holes [39, 107]. Small bilayer patches are occasionally present in the middle of grains. The star-shaped LG graphene grains are $50-200$ µm single crystals (Fig. 4.1D) [60, 83] of single-layer graphene with small multilayer patches at the center. All of the nanoindentation experiments reported below were performed on the single-layer areas of the SG and LG graphene films.

To create suspended membranes, graphene films grown on copper foil were transferred onto a silicon dioxide substrate with an array of holes with 1 and 1.5 µm in diameter (Fig. 4.1E, see Methods in Supplementary Materials, figs. 4.5 and 4.6). We found that two of the processing techniques used in previous studies [39, 88] severely weakened the

grain boundaries in CVDgraphene: etching the copper with ferric chloride (FeCl3) and removal of a polymer support by baking in air (figs. 4.7 and 4.8). Both steps were avoided herein: the copper was etched with ammonium persulfate instead of ferric chloride, and polydimethylsiloxane (PDMS) was used to support the graphene during copper etching, and to dry-stamp it onto the substrate without baking. The scanning-electron-microscopy (SEM) image of Fig. 4.1F shows the transferred LG graphene film. (See Fig. 4.7A for SG graphene) The graphene films form membranes tautly suspended above the holes, with little contamination. Raman spectroscopy confirms that the membranes are highly crystalline graphene with few defects. (Fig. 4.9)

We used nanoindentation to measure mechanical properties of the suspended membranes, as described in [58, 84]. A representative force-displacement curve obtained using an AFM with a diamond tip of 26 nm radius is shown in Fig. 4.1G. The curve was well fitted by a quasiempirical polynomial form [58]. The cubic fitting parameter yielded 99% confidence intervals for the mean of elastic stiffness of 328 ± 15 N/m near that of pristine graphene (340 N/m), and an order of magnitude higher than the value previously reported for CVD-graphene (55 N/m) [88]. Moreover, the force required to break the membrane is 2000 ± 420 nN, much greater than the previously observed (50-120 nN) [39, 88]. The AFM images in the inset show a SG membrane before and after fracture. The samples showed no sign of slippage at the periphery and the fracture pattern was similar to that observed for pristine graphene (Fig. 4.10).

For statistical analysis of stiffness and strength, we tested a large number of specimens using a nanoindenter, with a 38 nm radius diamond tip (Fig. 4.11A). Each membrane was cyclically tested to increasing depth to fracture; the non-hysteretic force-displacement curves were analyzed as above. Histograms of the derived elastic stiffness are shown in Figs. 4.2A and B for LG and SG graphene (see Fig. 4.11B for pristine). We obtained elastic moduli of 324 ± 13, 339 ± 17, and 328 ± 17 N/m (which correspond to a 3D Young's modulus of $\tilde{1}$ TPa) for pristine, LG, and SG, respectively. Based upon one-way ANOVA analyses, there are no statistical differences among these three values, or between these and the value previously obtained for pristine graphene [58] (Fig. 4.12A
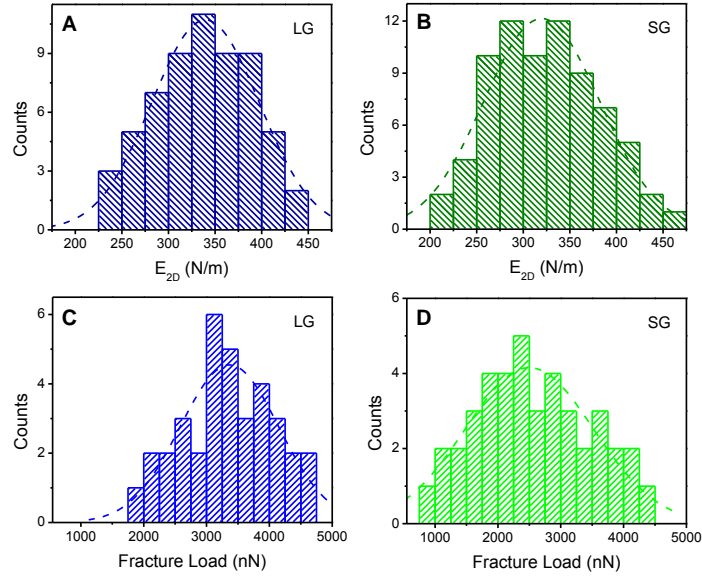
Figure 4.2: Statistical analyses of nanoindenter results. The histograms of the elastic stiffness of (A) LG, and (B) SG graphene films. The histograms of fracture load for (C) LG, and (D) SG graphene films. A tip with 38 nm radius was used in all tests. The dashed lines indicate fitted Gaussian distributions.

and table 4.1); all are in agreement with theoretical predictions in the absence of grain boundaries [47]. The wider distributions observed for SG and LG graphene may be due to the presence of wrinkles and small bilayer patches in the CVD-grown membranes.

The measured fracture loads for LG and SG membranes are shown in Figs. 4.2C and D (see Fig. 4.11C for pristine). The measurements yield fracture loads of 3410 ± 260, 3370 ± 340, and 2590 ± 380 nN for the pristine, LG, and SG films, respectively. The fracture load of the SG films is statistically different from that of the pristine and LG films, while there is no statistical difference between the fracture loads of the pristine and LG graphene based upon one-way ANOVA. (Fig. 4.12B and table 4.2) The smaller mean fracture load and wider distribution observed for SG graphene indicates that the strength is influenced by the randomly occurring defects and grain boundaries in the membranes. Nevertheless, the measured fracture load of the SG graphene is much larger than seen in previous measurements [39, 88].

We calculate the breaking strength of the graphene films as a function of the measured

fracture load and tip diameter with an experimentally validated multiscale model based upon atomic-scale ab initio density functional theory [113]. This constitutive model informs a continuum description of anisotropic and nonlinear elastic behavior for in-plane deformation [112, 113] that permits numerical modeling of the stress in the graphene up to the point of rupture. Figure S9 shows the equibiaxial true stress vs. load under the center of a 38 nm indenter tip for pristine graphene, which yields an equibiaxial breaking strength of 34.5 N/m (103 GPa, when expressed as a 3D value). The mechanical strength or peak stress that can be supported by graphene is a function of the loading configuration. For uniaxial stress in the armchair direction, the same model predicts a strength of 39.5 N/m (118 GPa), consistent with our previously-reported value of 42 ± 4 N/m for the same loading configuration (see Supplementary Materials). With an identical fracture load, LG graphene has an equivalent breaking strength to pristine graphene. Remarkably, the average equibiaxial strength of SG graphene is only slightly smaller, 33 N/m (98.5 GPa). A similar value was obtained for SG membranes tested by AFM. These results demonstrate that polycrystalline graphene with well-stitched grains can act as a large-area ultra-strong material.

Because the stress decreases inversely with distance from the indenter tip, the stress under the tip at rupture does not necessarily correspond to the grain boundary strength. Therefore, we performed indentation tests directly on a few grain boundaries identified by TEM. SG films were transferred onto TEM grids with 2.5 μm holes using a poly(methyl methacrylate) (PMMA) transfer technique [39, 48], followed by annealing in hydrogen and argon to remove the PMMA without reducing the strength of the films. The bright-field TEM (BF-TEM) image of Fig. 4.3A shows a suspended SG film, with adsorbates (likely PMMA residue) that decorate grain boundaries, as confirmed by higher-resolution imaging (Fig. 4.3)[39, 47]; these adsorbates are not observed in LG films (Fig. 4.14). The DF-TEM map of Fig. 4.3C shows the corresponding grain structure. The adsorbates render the grain boundaries visible in AFM (Figs.4.3E, 4.15), but are also present at wrinkles, so that AFM imaging alone is not sufficient to identify grain boundaries. Adsorbates are not expected to affect the grain boundary properties because of the very low

46
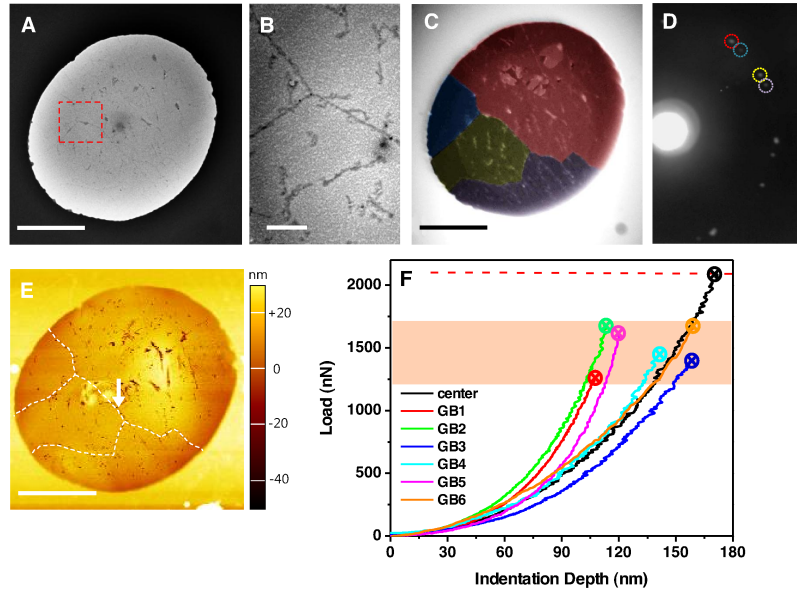
Figure 4.3: BF-TEM observation of grain boundaries and AFM nanoindentation on grain boundaries. BF-TEM images of (A) suspended SG graphene film over a hole and (B) enlarged BF-TEM image of red-dotted area in (A). (C) False-color DF-TEM image and (D) SAED of the same region. The diffraction spots corresponding to each color of (C) are indicated in (D) with circles of different colors. (E) AFM topology image shows that arrays of PMMA residue adhere to grain boundaries. The grain boundaries and indentation point are indicated by dashed lines and white arrow in (E). (F) AFM indentation results show that fracture occurs at slightly lower load when AFM tip indents on grain boundary. Scale bar: 1 Îijm except for 200 nm of (B).

stiffness and strength of PMMA.

Figure 4.3F shows the results of six indentation tests with the tip placed directly on asymmetric tilt grain boundaries near the center of the membrane. An additional test performed at the center of a grain away from grain boundaries (Fig. 4.15I) yielded fracture load similar to that of pristine graphene. The fracture loads at the grain boundaries are 20-40 % smaller, but still an order of magnitude larger than previously measured [39, 88]. The same multiscale analysis described above gives a range of equibiaxial stress of 30-33 N/m (90-99 GPa) for the strength of the grain boundaries, representing at most 15 % reduction from the intrinsic strength. These results confirm that grain boundaries in graphene can achieve ultra-high strength.

Atomistic scale simulations of symmetric tilt grain boundaries predict that grain boun-

47

daries with large tilt angles can achieve near-intrinsic strength (above 30 N/m), but those with low tilt angle possess lower strength of 13-26 N/m, depending on the precise arrangement of defects [28, 114]. The simulated grain boundaries consist of periodically spaced pentagonheptagon ring defects along straight grain boundaries. The simulations predict rupture initiation at the bond joining the pentagonal and heptagonal [48, 88, 121] rings, and that decreasing its initial equilibrium length (i.e. smaller misfit "prestrain") increases grain boundary strength [28, 114].

The asymmetric tilt grain boundaries in the experiments, which cover a wide range of tilt angles (cf. Fig. 4.16 and Table 4.3), consistently exhibited strength above 30 N/m, suggesting that the predicted variation in strength with tilt angle does not occur in these samples. The tortuous atomic structure of random [39] asymmetric grain boundaries is significantly more complex than that assumed for the simulations of symmetric grain boundaries [28, 114]. The more complex energy-minimizing structure [17] likely leads to a smaller misfit "prestrain" of the critical atomic bonds at in the 5-7 defects, thus explaining the ultra-high strength (see details in Fig. 4.16 and Table 4.3).

In addition to well-stitched grain boundaries, we also occasionally observe boundaries in which the adjacent graphene grains overlap (50 nm in width) but do not covalently join [39, 107] (Fig. 4.17). These boundaries were observed to be extremely weak, with no measurable force upon AFM indentation. Overlapped grain boundaries have been observed to possess higher conductance [107] than stitched boundaries, but will result in much weaker films.

To further elucidate the fracture behavior of graphene, AFM nanoindentation on SG membranes was performed to failure, and the ruptured films were observed with TEM. Indentation on a grain boundary (cf. white arrow in Fig. 4.4A) initiates an intergranular crack as in Fig. 4.4B and Fig. 4.18 under the approximately equibiaxial stress state beneath the indenter tip–thus demonstrating the grain boundary to be somewhat weaker than graphene. The crack later kinks into the adjoining grains due to the more complex stress state. Contrary to the prediction or experimental observation during electron irradiation [47], the torn edges of the transgranular cracks have irregular saw-tooth shapes
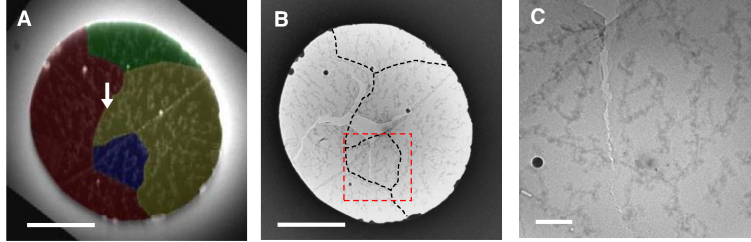
Figure 4.4: (A) False-color DF-TEM image of the suspended SG graphene film over a hole before indentation. The white arrow indicates the indentation point. (B) BF-TEM image after indentation. The black-dashed lines indicate grain boundaries. (C) Enlarged BF-TEM image of the red-dashed area of (B). Scale bars, 1 μm; (C) 200 nm.

as shown in the enlarged BFTEM image of Fig. 4.4C and Fig. 4.19.

Our measurements reveal that the elastic stiffness and strength of CVD-graphene are comparable to those of pristine graphene despite the existence of grain boundaries. Moreover, the strength of grain boundaries is much stronger than previously measured, in agreement with the maximum values predicted in simulations. This study establishes CVD-graphene as a large-area, high-strength material for flexible electronics and strengthening components.

4.1 Materials and Methods

4.1.1 Synthesis of graphene

The 25 μm-thick copper foil (Alfa Aesar, 99.8%) was used for graphene growth under the different conditions for small-grain (SG) and large-grain (LG) samples.

A. Growth condition for SG sample: The copper foil was heated to 1000 °C in a

hydrogen flow of 2 sccm at a pressure of 50 mTorr. After annealing for 60 min, graphene was grown by introducing methane gas flow of 35 sccm while maintaining hydrogen flow. After growth at 300 mTorr and 1000 °C for 30 min, the sample was rapidly cooled to ambient temperature under a flow of methane and hydrogen. As shown in Fig. 4.1A, continuous and polycrystalline small-grain graphene was grown with grain size ranging from 1 to 5 μm. B. Growth condition for LG sample: A closed pocket of copper foil was used for growth of large-grain samples as reported by Li et al. [60]. The copper pocket was heated to 1000 °C in a hydrogen flow of 2 sccm at a pressure of 1 mTorr. After annealing for 60 min, graphene was grown at 10 mTorr and 1035 °C by flowing methane of 1 sccm and hydrogen of 2 sccm. After growth for 60 min, the sample was rapidly cooled to ambient temperature under a flow of methane and hydrogen. As shown in Fig. 4.1B, the isolated and star-shaped large-grain graphene was grown with grain size ranging from 50 to 200 μm.

4.1.2   Preparation of samples for indentation

A 1 cm×1 cm array of circular wells, which have 1 μm and 1.5 μm in diameters and 800 nm in depth, were patterned on Si substrate with a 300 nm-thick SiO2 by nanoimprint lithography and reactive ion etching as reported previously (2). Graphene films were transferred onto the substrate through dry transfer technique as depicted in Fig. 4.5. After attaching graphene-grown copper foil to a PDMS (polydimethylsiloxane, Dow Corning) stamp, the copper was etched in ammFonium persulfate (Transene Co., APS-100, 20wt%) for 2 hours, then the graphene was carefully washed with flowing DI water to remove residue, followed by drying with a weak flow from a nitrogen gun. To check any damage of graphene during etching process, all the samples on the PDMS stamps were observed with optical microscope before transfer as shown in Fig. 4.6. The continuous SG graphene film of Fig. 4.6A has a number of small bilayer patches and wrinkles, meanwhile the starshaped LG graphene film of Fig. 4.6B exhibits a multilayer patch in the middle. The prepared graphene film on a PDMS stamp was slowly placed onto the pre-patterned substrate and we waited for a day until graphene film is fully transferred. After the
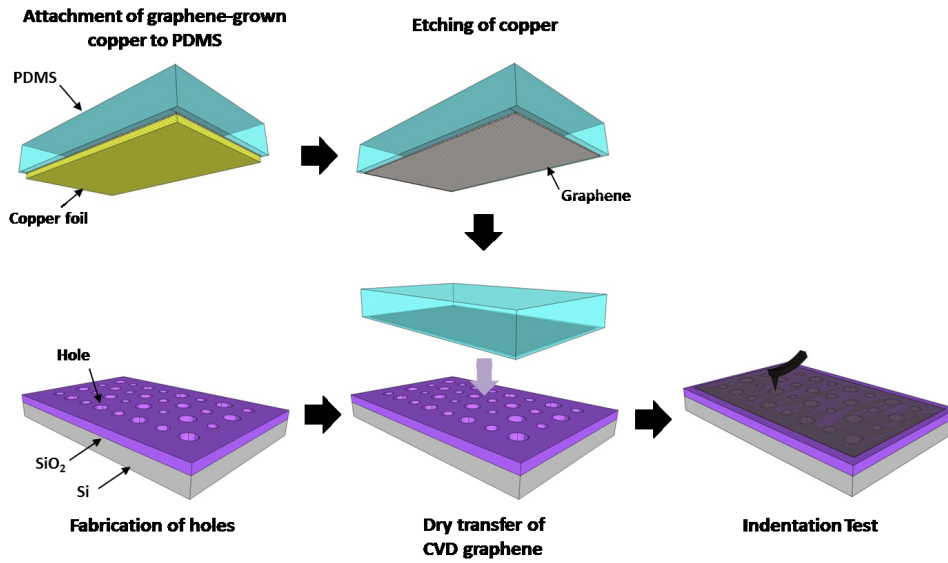
Figure 4.5: Fabrication process of the suspended CVD-graphene film for indentation test.
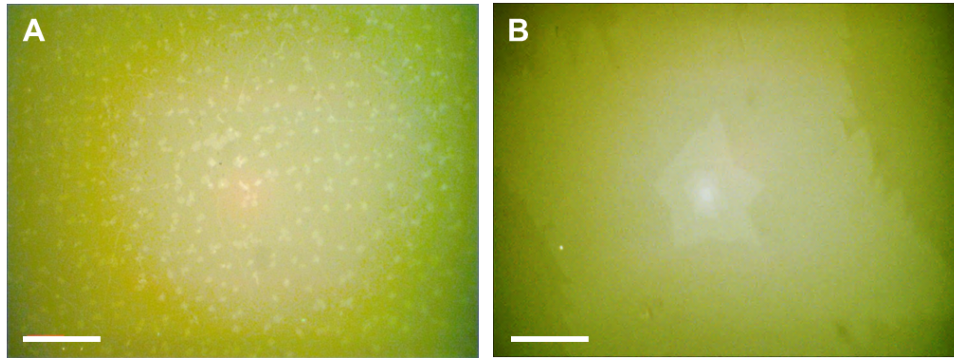
Figure 4.6: Optical Images of graphene films on PDMS before transfer to the substrate. Optical micrographs of (A) SG and (B) LG graphene films on PDMS stamps after etching of copper. The scale bar is 20 μm.

PDMS stamp was heated on the hot plate of 100 °C for 10 min, the stamp was slowly removed from substrate leaving behind suspended graphene. The success of this transfer technique for the suspended graphene film indirectly verifies that CVD-graphene is strong. The suspended pristine graphene for nanoindentation test was prepared by exfoliating graphite on the substrate with holes as previously reported [58].

4.1.3 Preparation of TEM samples

The graphene films were transferred on top of thin silicon nitride TEM grids (Figs. 4.1A and B) and perforated silicon nitride TEM grids with holes of 2.5 μm in diameter (Figs. 4.3 and 4.4) using PMMA transfer technique [39, 107]. After coating of PMMA layer,

the copper foil was etched with ammonium persulfate for 2 h. After rinsing with DI water repeatedly, the floating PMMA-coated graphene film was scooped with TEM grid. For removal of PMMA thin film, TEM samples were dipped in acetone for a few hours, and then annealed at 345 °C for 4 h in a forming gas of hydrogen and argon. The TEM (JEOL JEM-100CX) was operated at 80 kV to avoid any damage to the graphene film from electron bombardment [86, 122].

4.2   Supplementary Text

4.2.1   Defect sensitivity of 1D, 2D, and 3D materials

As shown by Orowan in 1949, the intrinsic tensile strength–the maximum stress a defect free material can resist in tension before failure–scales as $\sigma_{int} \sim \sqrt{(E\gamma/a)}$, where E is Young's modulus, γ is the surface energy, and a is the atomic spacing [76]; more recent theoretical estimates suggest that $\sigma_{int} \approx E/10$ [18, 44]. However, typical 3D materials are much weaker still due to the inevitable presence of defects that circumvent homogeneous tensile cleavage by activating other failure mechanisms [66].

Reduction of material dimensionality has proven to be an efficacious method to preclude the formation of initial defects or at least to constrain their sizes. For example, quasi-1D materials such as silicon nanowires with diameters of a few tens of nanometers can approach the intrinsic strength [99]. Metal nanowires can also achieve great strength when free of dislocations [117], but the operative failure mechanism is due to homogeneous shear at stresses approaching the intrinsic shear strength of $\tau_{int} \approx \mu/2\pi$, where the elastic shear modulus $\mu = E/(2(1 + \nu))$. Only when the density of dislocations within metal nanowires is so high as to render them immobile, the strength of a metal nanowire can supersede the intrinsic shear strength and approach the intrinsic tensile strength [117]. Nonetheless, the strength of nanowires remains limited by surface defects. Carbon nanotubes more closely approach the 1D ideal, but are sufficiently sensitive to defects that they can approach, but fall short of, the intrinsic strength [79].

Reduction of dimensionality also reduces the dimensions in which a material can

provide structural support; hence true 2D materials such as graphene where all atoms exist on the surface are of particular interest. The lower dimensionality of graphene relative to three dimensional bulk materials concomitantly reduces the dimensionality of defects. The 3D bulk defects such as voids or different phases reduce to 2D defects, whereas 2D bulk defects such as free surfaces, stacking faults, grain boundaries, and twin boundaries reduce to 1D defects. Likewise, 1D bulk defects such as crack fronts and dislocations lines reduce to 0D defects. Only the 0D bulk defects such as atomic vacancies and substitutional atoms or interstitial atoms remain 0D defects.

The reduced dimensionality modifies stress distributions due to applied forces as well as defects, which affects the interactions between defects. Taking R to be the distance from a point load or a defect, the stress singularity of a point load changes from $1/R^2$ in 3D to $1/R$ in a 2D material. The stress variation introduced by voids changes from $1/R^3$ in 3D to $1/R^2$ in a 2D material. Likewise, the far-field stress of dislocation loops and interior cracks in a 3D material each diminishes as $1/R^3$ in 3D but respective far-field stress fields of a dislocation dipole and an interior crack diminish as $1/R^2$ in 2D. (However the nearfield stress of dislocations retains the $1/R$ singularity and that of cracks retains the $1/R^{0.5}$ singularity.) Thus the far-field stresses of 2D materials persist at greater relative distances in a 2D material than in a 3D material, so 2D materials are generally more sensitive to defects than 3D materials. However, in quasi-1D materials the stress due to defects varies as $1/R^0$ (i.e. no diminution with distance), so 2D materials are less sensitive to defects than 1D materials.

Notwithstanding that 2D materials are more defect-sensitive than 3D materials, 2D materials can achieve much higher stress relative to the intrinsic strength. This is possible because the defect densities in 2D materials can be much smaller than in 3D materials. We have shown, for example, that suspended graphene prepared by mechanical exfoliation and loaded mechanically via nanoindentation away from a free edge can achieve its intrinsic strength, suggesting that the material is entirely free of defects in the region of stress concentration. Of fundamental interest is the behavior of CVD-grown graphene that contains defects. Atomic vacancies are one potential defect, but it is known that

the equilibrium concentration of atomic vacancies in graphitic materials is very low at ambient temperature. Dislocations are known to exist in graphene, but are likely nucleated from atomic vacancies only at high effective temperatures induced by transmission electron microscope (TEM) observation [110]. Effective CVD growth of graphene has been shown to produce graphene that is free of initial voids and cracks. Thus grain boundaries are the only remaining defect of concern in graphene under ambient conditions.

4.3 Weakening of graphene during processing

As discussed in the main text, our results are in contradiction to previous studies (refs. [39] and [88]), which report that CVD graphene is significantly less stiff and less strong than pristine. It is important to identify the precise reasons(s) for weakness observed previously, so that our results can be replicated and used to guide materials synthesis and processing. As shown in the main text and methods, the SG CVD graphene used in our study is highly similar in grain size and grain boundary shape to the graphene studied previously, which argues against differences in the crystal structure of the as-grown CVD graphene, and point instead toward processing details, as being the cause of the discrepancy. Our sample preparation process differs from that of the previous studies in two important ways: the use of ammonium persulfate ($(NH_4)_2S_2O_8$) instead of ferric chloride ($FeCl_3$) for copper etching, and the elimination of an air-baking step to remove PMMA. We investigated the effect of each factor separately.

We found the use of ferric chloride etchant results in visible differences in the quality and yield of the suspended graphene membranes: the graphene films tear more easily, and the yield of suspended membranes is much lower (Figs. 4.7A and B). Testing of the surviving suspended membranes showed an order of magnitude smaller fracture load (Fig. 4.8A). This test directly implicates ferric chloride as a cause of the weakness of previous films. Various metal particles, including iron present in ferric chloride, have been demonstrated to etch graphene, leading to voids or other defects [9, 86, 96].

We next investigated the role of air-baking to remove PMMA. As a control, we found
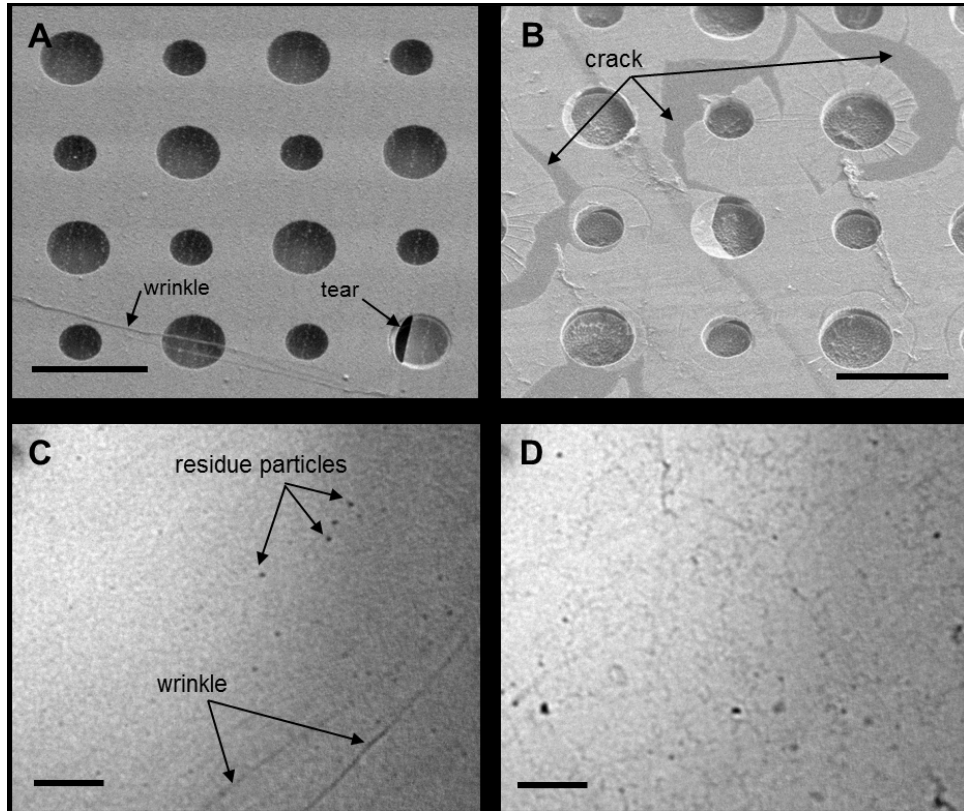
Figure 4.7: Effects of ferric chloride and annealing. (A) SEM image of SG graphene film transferred by PDMS after etching of copper with ammonium persulfate. (B) SEM image of cracked SG graphene film transferred by PDMS after etching of copper with ferric chloride. BF-TEM images of the SG graphene film annealed at 345 ℃ for 4 h (C) in a forming gas of hydrogen and argon and (D) in air. The air-annealed graphene has many defects and cracks, which look like dark lines. The scale bar is 3 μm.

that CVD graphene samples processed with PMMA, etched in ammonium persulfate, and annealed at high temperature in an inert background (345 °C for 4 h in a forming gas of hydrogen and argon) did not show defects detectable in TEM imaging (Fig. 4.7C) or reduction in mechanical strength (Fig. 4.8B). On the other hand, samples annealed in air at both 200 °C and 300 °C showed damage to grain boundaries and decreases in fracture load (Figs. 4.7D and 4.8B). Similar results have been observed previously, and are attributed to local oxidation at chemically active grain boundaries [69]. Samples annealed at 400 °C in air were completely destroyed.

These results confirm that processing differences are the primary cause of the discrepancy between our results and those reported previously , [39, 88]. They also indicate that both use of ferric chloride and air-baking result in weaker graphene, and should be avoided in most applications.
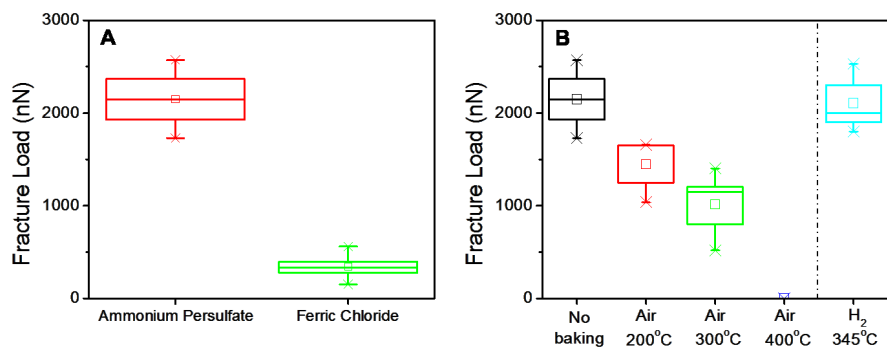
Figure 4.8: Effect of ferric chloride and air-baking on mechanical strength of SG graphene films. (A) Fracture load of SG graphene films prepared with different copper-etching agents. In the transfer process, copper foils were etched with different copper-etching agents of ammonium persulfate and ferric chloride. In case of ferric chloride, graphene shows an order of magnitude smaller fracture load. These samples were not annealed. (B) Fracture load of SG graphene films annealed in different conditions. In this case, copper was etched with ammonium persulfate. When the suspended SG graphene film was annealed at 345 ^{o}C in inert gas flow of H_2 and argon, there is no degradation in mechanical strength. However, air-baking shows a clear decrease in fracture load with increasing temperature. All of the suspended SG graphene samples were broken after air-baking at 400 ^{o}C. Each plot includes five-number summary: the sample minimum, lower quartile, median, upper quartile, and sample maximum.

4.3.1   Raman spectroscopy of suspended graphene films

As shown in Figs. 4.9A-D, the location of suspended graphene film was identified with optical microscope and AFM. To determine the quality of suspended graphene films, Raman spectroscopy (Renishaw, inVia) was employed with 532 nm laser. As shown in Figs. 4.9E and F, all suspended graphene films have relatively high I_{2D}/I_G intensity ratio (> 4.5) and FWHM of 2D peak (< 29), consistent with a highly crystalline single-layer graphene (exfoliated single-layer graphene suspended over hole, denoted as Ref. in Figs. S5E and F). However, the suspended SG graphene films show a small D peak at most of positions as shown in Fig. 4.9E. In case of suspended LG graphene films, no D peak or relatively small D peak was observed as shown in Fig. 4.9F and elsewhere [60]. Even though LG graphene consists of a single crystal, Raman spectra inform us that some area of LG graphene has defects, probably atomic-level defects or wrinkles.
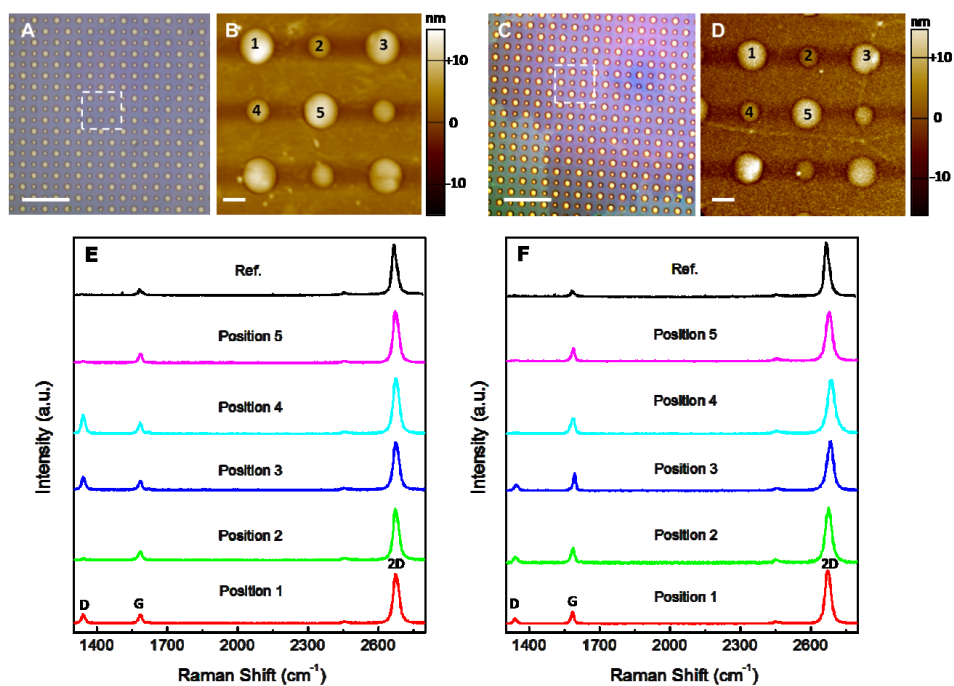
Figure 4.9: Optical micrographs and AFM images of the suspended (A-B) SG and (C-D) LG graphene samples. AFM images of (B) and (D) were obtained from the dashed areas of (A) and (B), respectively. Raman spectra of the suspended (E) SG and (F) LG graphene films were obtained from the positions indicated by numbers in AFM images of (B) and (D). The Raman spectrum of a suspended single-layer graphene sheet exfoliated from graphite (denoted as Ref.) is displayed for comparison. The scale bar is 10 μm for optical micrographs and 1 μm for AFM images.

4.3.2 AFM indentation process

The suspended graphene samples were carefully scanned in non-contact AFM mode to locate an indentation spot. The force-displacement curves were obtained by indenting the center of suspended graphene with an AFM (XE-100, Park Systems). The cantilever with a diamond tip (tip radius = 26 nm, MicroStar Tech) was used. When the peak load is smaller than fracture load, the loading and unloading force-displacement curves shows no hysteresis, which means that the graphene film is fully clamped via van der Waals interactions with the substrate and does not slip around the periphery during measurement [58]. Therefore, the curves showing hysteresis were excluded from analyses. When the SG graphene film was tested, small reductions in force-displacement response were occasionally observed leading to a serrated curve as shown in Fig. 4.10, resulting in high breaking load. These small drops during indentation were explained in terms of initiation of cracks at grain boundaries [39]. However, the measured fracture load (Fig. 4.10) is an order of magnitude higher than previously reported [39] and even comparable to that of pristine graphene despite small drops. We also observed this behavior even in the suspended pristine graphene, which has an edge near the perimeter of the hole. Furthermore, TEM observation and nanoindentation of Fig. 4.3 did not show this behavior even though the AFM tip was place on the grain boundaries. From these, we can deduce that these small drops are attributed to slippage of graphene rather than crack formation at grain boundaries.

4.3.3 Nanoindenter indentation process

An Agilent G200 nanoindenter outfitted with a dynamic contact module (DCM) and a piezoelectric positioning stage (Nanovision) was used to scan and indent graphene samples. We used a diamond DCM tip (tip radius = 38 nm) fabricated by MicroStar Tech. After scanning of the graphene samples, the topography image was used to position the center of the graphene membrane under the diamond tip. This scanning-positioning technique reproducibly located the tip to the center of the graphene membrane to within 1 nm. The G200 nanoindenter continuous stiffness method (CSM) was implemented in a
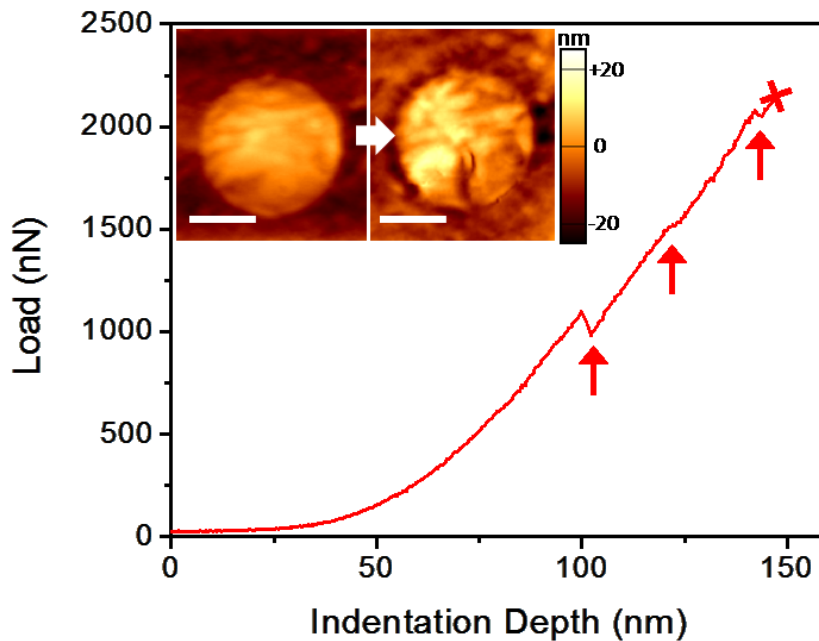
Figure 4.10: Force-displacement curve of the SG graphene film acquired in AFM indentation test. The small drops in the curve are observed during indentation. AFM images of the inset show the suspended SG graphene film before and after AFM indentation. The scale bar is 0.5 μm.

modified manner to determine the point of surface contact. The CSM allows the loading to have a sinusoidal signal applied during a test segment. Nanoindentation of semiinfinite materials uses this sinusoidal load to continuously measure the stiffness of the material as the load is increased [31]. In this method, the indenter tip is oscillated at its resonant frequency. By monitoring the phase angle of the tip, we were able to detect changes in surface stiffness below 1 N/m.

Nanoindentation of the graphene membranes was achieved through a three-step indentation process. In the first two steps, the CSM was implemented to determine surface contact. In the third step, the CSM was disabled to remove unwanted noise from the force-displacement curves. The first step used the CSM method to determine surface contact 800 nm from the center of the membrane on the silicon oxide. The second step used the CSM method and a slower approach speed to determine when contact with the graphene membrane was achieved by monitoring the phase angle of the indenter tip. The third step disabled the CSM method and performed nanoindentations at the center of

Table 4.1: ANOVA of elastic stiffness.

Source of Variation	Sum of Squares	d.f.	Mean Square	F-Statistic	p-Value
Among Groups	14977.4	3	4992.467	2.257124	0.0820
Within Groups	630383.2	285	2211.871		
Total	645360.6	288			

Table 4.2: ANOVA of fracture load.

Source of Variation	Sum of Squares	d.f.	Mean Square	F-Statistic	p-Value
Among Groups	16408785	2	8204393	14.23988	3.29×10^{-6}
SG vs. others	16376446	1	16376446	28.42363	5.47×10^{-7}
Between Pristine and LG	32339	1	32339	0.0561289	0.8132
Within Groups	61648701	107	576156.1		
Total	78057486	109			

the membrane at increasing depths until fracture was recorded. The depth increments were typically 20 nm. The force-displacement curve from nanoindenter is similar to that from AFM nanoindentation as shown in Fig. 4.11A. This can be fitted by the equation used in our previous report [58].

As shown in Fig. 4.12B and C, the box plots of elastic stiffness and fracture load for pristine, LG, and SG graphene films show that elastic stiffnesses of three samples are almost the same. On the other hand, the average fracture load of SG graphene looks smaller than those of pristine and LG graphene films. To verify this statistically, we applied ANOVA (Analysis of Variance) to the nanoindenter results. As shown in Table 4.1, when the stiffnesses of three groups in our work and pristine graphene in our previous paper [58] were compared, p-values (larger than the threshold value of 0.05) demonstrate that four groups of graphene share the same elastic stiffness value regardless of measurement tools. On the other hand, Table 4.2 shows that pristine and LG graphene films have the same average fracture load. However, fracture load of SG graphene film is different from those of the others because p-value is much smaller than 0.05.
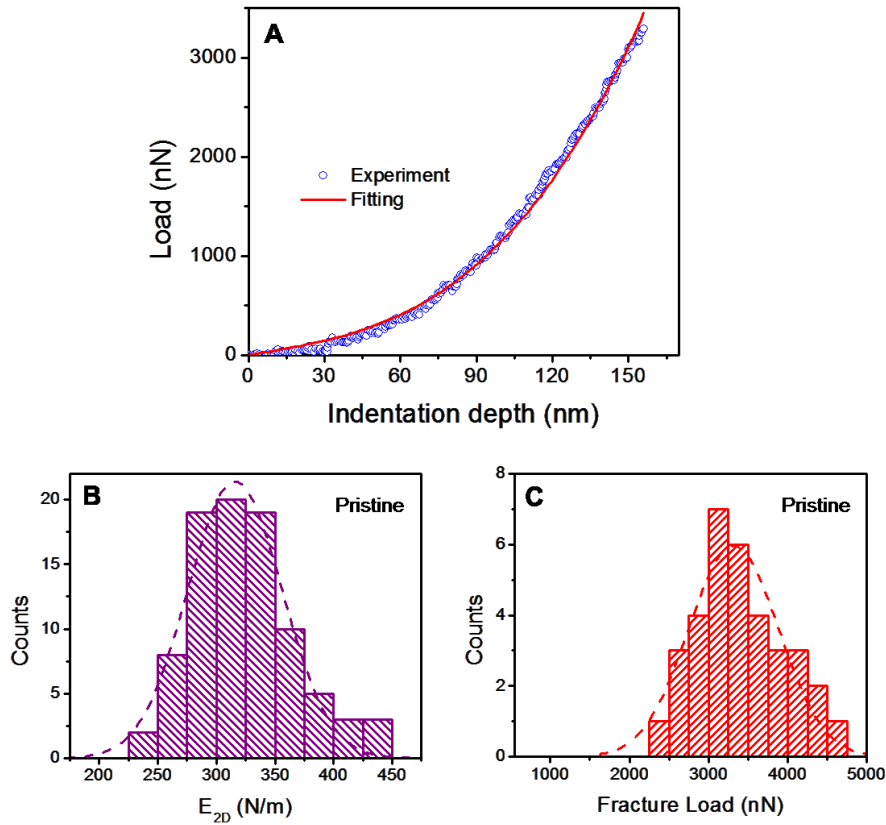
Figure 4.11: Nanoindentation results and statistical analysis. (A) Force-displacement curve of the LG graphene film with nanoindenter. The red line is a fitting curve to Eq. 1. The histograms of (B) elastic stiffness and (C) fracture load for pristine graphene films. A tip with tip radius of 38 nm was used in all tests. The dashed lines indicate fitted Gaussian distributions.
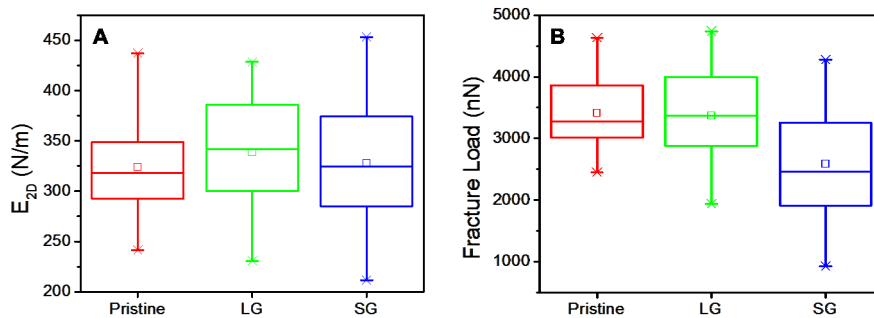
Figure 4.12: Statistical analysis for comparison. The box-plots of (A) elastic stiffness and (B) Fracture load for pristine, LG, and SG graphene films. Each plot includes five-number summary: the sample minimum, lower quartile, median, upper quartile, and sample maximum.

4.3.4 Multiscale model of nonlinear and anisotropic elastic response of graphene

In our previous study [58], we modeled the elastic response of graphene to be nonlinear and isotropic based upon a third-order series expansion of the strain energy density potential. The corresponding expression for uniaxial stress had both linear and quadratic terms of strain. The linear coefficient, the Young's modulus, was determined from fitting the measured force vs. displacement curves to the quasi-empirical polynomial form [58]. The quadratic coefficient was determined based upon fitting of the predicted force on the indenter at failure to the measured breaking force. This analysis resulted in a predicted intrinsic strength of graphene under uniaxial stress conditions to be 42±4 N/m, with the stress measure being true (Cauchy) stress defined as force per current length.

We subsequently refined our analysis of the elastic behavior of graphene [112] by expanding the strain energy density potential in a Taylor series truncated after the fifth power in strain. Upon considering the symmetry elements of the graphene crystal lattice to account for anisotropy in addition to nonlinearity, the continuum stress vs. strain relationship has fourteen elastic constants. The values of these elastic constants were determined by fitting the continuum theory to the stress vs. strain response calculated via first principles Density Functional Theory (DFT) calculations. This analysis resulted in a better estimate for the intrinsic strength of graphene under conditions of uniaxial stress in the armchair direction (i.e. stress in the armchair direction while allowing for a Poisson contraction in lateral directions) to be 39.5 N/m in true stress measure, which is within the uncertainty of our previous estimate. When expressed as the derived 3D stress measure upon normalization by 0.335 nm, the uniaxial stress in the armchair direction is 118 GPa true stress.

Likewise, under conditions of equibiaxial strain (i.e. equivalent stresses in armchair and zigzag directions) for which the mechanical response is isotropic, the intrinsic strength of graphene is 33.1 N/m in true stress measure, which corresponds to a derived 3D true stress of 98.8 GPa.

The nonlinear and anisotropic elastic constitutive behavior of graphene was implemen-

ted [113] as a user material (UMAT) subroutine for the general finite element method (FEM) package ABAQUS [97]. A detailed FEM model of the nanoindentation of suspended circular monolayer films of graphene was then performed by assuming a rigid spherical frictionless indenter tip [113]. The higher order elastic constants of graphene have been calculated by a least squares fit to density functional theory (DFT) results [112]. The constitutive model included fourteen elastic constants that describe the second Piola-Kirchhoff stress tensor in powers of the Lagrangian strain tensor, work conjugate stress-strain tensors, expanded to the fifth order, as had been done in Chap. 2. In ABAQUS, The FEM model employed a 1 μm-circular membrane clamped at the perimeter with 16524 four-node membrane elements and 16633 nodes. The indenter tip, modeled as a rigid sphere, was pushed into the suspended membrane in 0.2 nm increments near the point of elastic instability in frictionless contact. Two indenter radii were used to model the two diamond indenters, 26 nm and 38 nm. The FEM model used in this study has been used to accurately predict the intrinsic strength of pristine graphene [113]. It captures the nonlinear and anisotropic behavior of graphene. The model provides a framework to accurately predict the stress experienced by the graphene membrane during nanoindentation based on DFT calculations. The results of the analysis are in Fig. 4.13A for two different indenter tip radii, where abscissa is the force on the indenter tip and the ordinate is the equibiaxial stress in the true stress measure immediately under the indenter tip. The maximum equibiaxial stress in Fig. 4.13A is slightly higher than 98.8 GPa due to a very small amount of amount viscosity introduced into the constitutive equation in the UMAT implementation to stabilize strain localization that occurs prior to overall elastic instability that leads to rupture. When this was transformed to show stress vs. strain as shown in Fig. 4.13B, the Lagrangian strain at fracture is around 0.2.

4.3.5 Direct indentation on grain boundaries

As explained in the main text, grain boundaries in the suspended graphene films can be identified via DF-TEM. The suspended LG graphene film has fewer remnant adsorbents and single crystal electron diffraction as shown in Fig. 4.14. As shown in Fig. 4.15A,
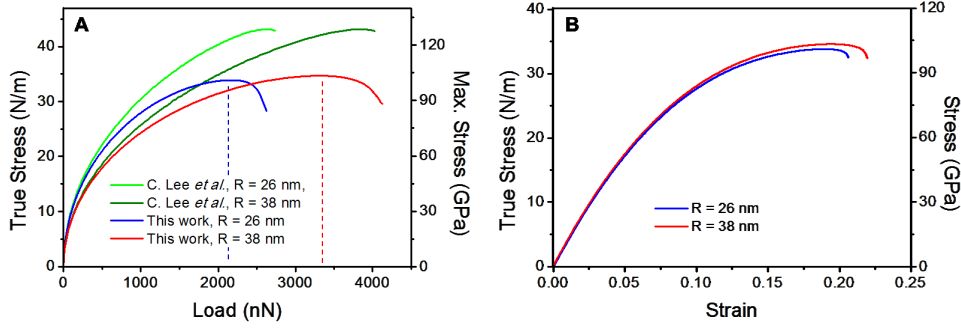
Figure 4.13: FEM analysis for determination of peak equibiaxial (true) stress. (A) FEM simulation results with nonlinear elasticity assumption. Two different tips with tip radii of 26 nm and 38 nm were used. The curves show the results from this work and our previous report [58]. (B) True stress vs. strain curve from FEM simulation. The Lagrangian strain at fracture is around 0.2.

BFTEM of the suspended SG graphene film shows wrinkles and adsorbates. From SAED of Fig. 4.15B, it is verified that the SG graphene is polycrystalline. By selecting the desired diffraction spot with aperture (circles with different colors), the corresponding DF-TEM images can be obtained as shown in Figs. 4.15C-F. Based on these four DF-TEM images, the false-color DF-TEM image of Fig. 4.15G were assembled. The AFM images of topology and phase in Figs. 4.15H and I show that adsorbates sit on grain boundaries. Noted that these adsorbates are also located on wrinkles and inside of grains. To determine the positions of the grain boundaries, therefore, both of DF-TEM and AFM are required. Using DF-TEM and AFM, we can find the exact position of grain boundaries in the suspended graphene and indent away from or on grain boundaries.

The graphene sheets with large-angle tilt boundaries with a high density of defects are predicted to be as strong as the pristine form and stronger than those with low-angle boundaries with fewer defects [28]. This predicted trend is contrary to the behavior in three-dimensional materials. The predicted high strength of large-angle tilt boundaries was explained in terms of the mechanics of critical covalent bonds joining pentagonal and heptagonal defect rings periodically distributed along the grain boundary. The simulations predict that this is the first bond to break at very high stresses. The initial misfit "prestrain" in this critical bond strongly affects the breaking strength, with a smaller misfit "prestrain" leading to greater grain boundary strength [28].
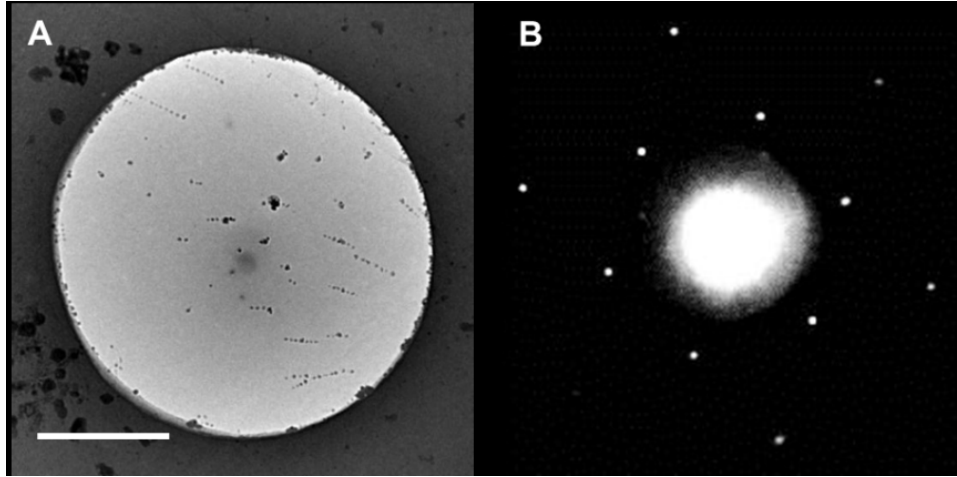
Figure 4.14: TEM observation of LG graphene film. (A) BF-TEM image and (B) SAED pattern of the suspended LG graphene film. The electron diffraction indicates this graphene is a single crystal and a small number of adsorbates are observed. The scale bar is 1 μm.

Recently, Y. Wei *et al.* [114] predicted that it is not just the density of defects that affects the mechanical properties, but also the detailed arrangements of defects. Even though the predicted strength of grain boundary in graphene increases with larger tilt angle, this trend breaks when pentagon-heptagon rings in grain boundary, which is usually observed in CVD-graphene, are not evenly spaced [114]. However, these simulations assume that grain boundary is symmetrical in atomic scale, unlike in grain boundaries of CVDgraphene. Experimentally, CVD-graphene has random asymmetric grain boundaries, containing pentagon-heptagon defects [39], but that the grain boundary atomic structure was significantly more complex and tortuous than the symmetric tilt grain boundaries of the simulations that we assumed to be straight. It is well established that grain boundaries adopt complex atomic structures to minimize misfit elastic energy [17]. The misfit "prestrain" of the critical covalent bond joining the pentagonal and heptagonal rings in such low-energy random asymmetric grain boundaries will be smaller than in less energetically favorable configurations. Thus, based on insight gained from the above analysis of idealized grain boundary structures, randomly oriented asymmetric tilt grain boundaries can be expected to exhibit very high strength, and our experiments demonstrate that the strength approaches that of pristine graphene. (Figs. 4.16 and table 4.3)
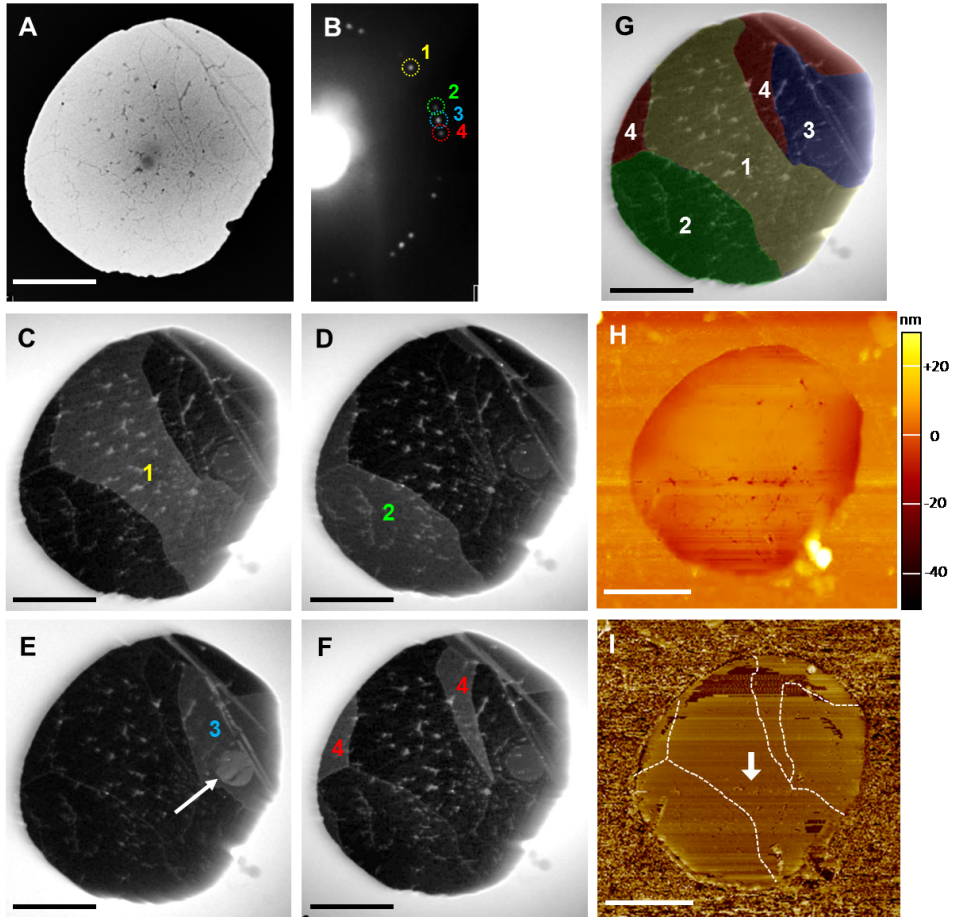
Figure 4.15: Identification processes of grain boundaries in the suspended graphene film. (A) BF-TEM image of the suspended SG graphene film and (B) SAED pattern. From each spot (circles with different colors) of electron diffraction, DF-TEM images were obtained as shown in (C-F). The small bilayer patch with round shape is indicated by white arrow in E. (G) False-color DF-TEM image of the same sample. AFM images of (H) topology and (I) phase show that the adsorbates are located along grain boundaries of graphene. The white arrow of (I) indicates the indentation point when the center of grain away from grain boundaries was indented by AFM as explained in the main text. The scale bar is 1 μm.

Table 4.3: Breaking load vs. tilt angle. The angle of θ_1 and θ_2 (relative to grain boundary) shows the grain boundaries are not symmetrical.

Sample	θ_1(deg)	θ_2(deg)	$\theta_1 + \theta_2$(deg)	Breaking Load (nN)
GB3	2	3	5	1405
GB6	7	9	16	1720
GB4	10	13	23	1449
GB5	13	14	27	1626
GB2	6	22	28	1695
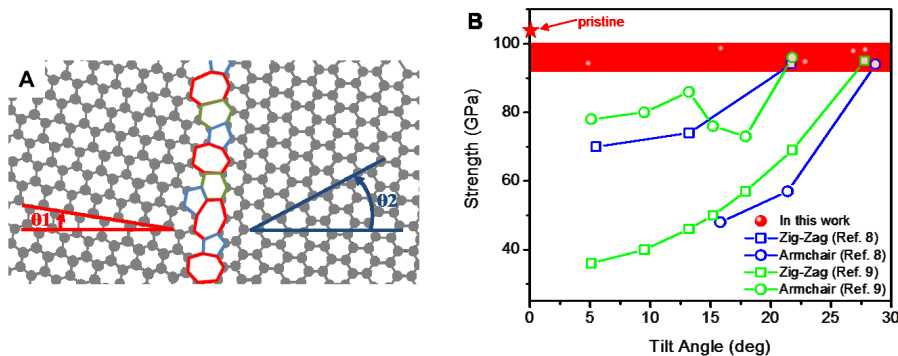
Figure 4.16: Relation between strength of grain boundary and tilt angle. (A) Schematic of asymmetric grain boundary consisting of pentagon-heptagon rings. The angles of $\theta 1$ and $\theta 2$ in the left and right lattices are determined by electron diffractions. The tilt angle of grain boundary is $\theta 1 + \theta_2$. Pentagon, hexagon, and heptagon rings are indicated by blue, green, and red lines in the grain boundary. (B) Plot of strength vs. tilt angle. The AFM indentation was performed on grain boundaries, which tilt angles are known by TEM observation before indentation test. The strength of pristine graphene (defect-free) is indicated in left-top corner. The measured strength in our work shows a relatively high strength regardless of tilt angle, while atomistic simulations showed an increase of strength as a function of tilt angle.

4.3.6 Mechanical properties of overlapped grain boundaries

We observed overlapped narrow areas crossing some of the suspended graphene film as shown in Fig. 4.15A and 4.16A. Even though most of them are wrinkles, it turned out that some of them are the overlapped grain boundaries as reported by Tsen *et al.* [107]. The overlapped grain boundary was identified with TEM as shown in Fig. 4.16. BF- and DFTEM images of Figs. 4.16A-D confirm that the overlapped region is not a wrinkle because it is located at the border of two different crystalline grains. In contrast, DF-TEM image of a wrinkle shows one grain divided by this overlapped line. In addition, because this boundary is brighter than other region in the DF-TEM image of Fig. 4.16D, this is a crystalline grain boundary with overlapped width of 50 nm between two grains, not the gapped grain boundary [107]. When the overlapped grain boundaries were examined, no measurable force was detected as shown in Fig. 4.16E. The blue-dashed line indicates the predicted force-displacement curve in AFM nanoindentation of the suspended graphene. This means that the overlapped grain boundary are held together by van der Waals interaction and is not stitched together via covalent bonding.
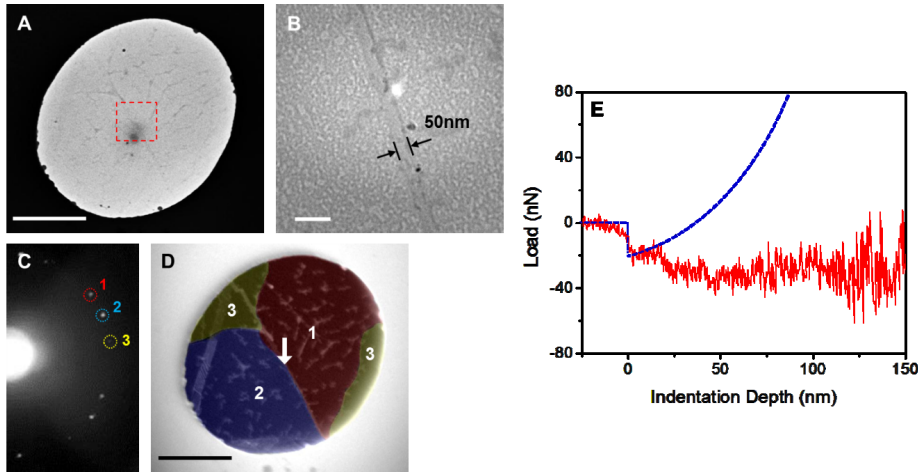
Figure 4.17: Properties of overlapped boundary. (A) BF-TEM image of the suspended SG graphene film and (B) enlarged TEM image of red-dashed area. The adsorbates are present along the overlapped boundary with width of 50nm. (C) SAED pattern and (D) False-color DF-TEM image of the same sample. (E) Force-displacement curve shows no measurable force when the overlapped boundary was indented. The blue-dashed line of (E) indicates the predicted behavior of the indented graphene. The scale bar is unit1μm except for 100 nm of (B).
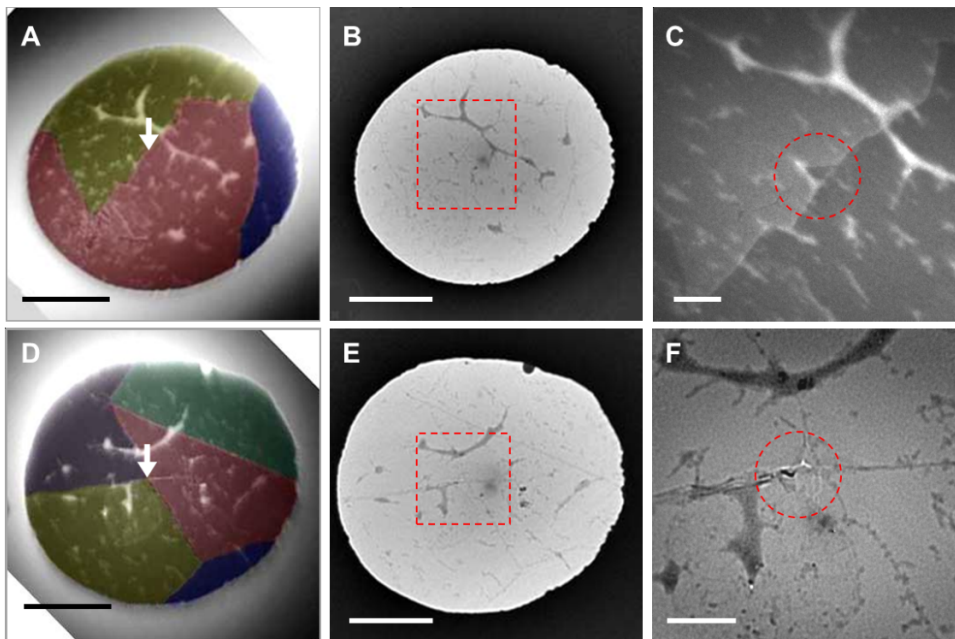
Figure 4.18: TEM observation of the SG graphene films after indentation on grain boundary. (A and D) False-color DF-TEM images of suspended SG graphene film before indentation. The white arrows indicate indentation points, where two grains meet at grain boundary. The indentation was stopped before complete fracture. (B and E) BF-TEM images of corresponding graphene films of (A) and (D) after indentation. There is no other crack across the graphene film except for indentation spot. (C) Enlarged DF-TEM and (F) BF-TEM images of the red-dashed areas in (B) and (E). A small crack indicated by red circle was formed at the indented point, following grain boundary. The scale bar is 1 μm except for 200 nm of (C) and (F).
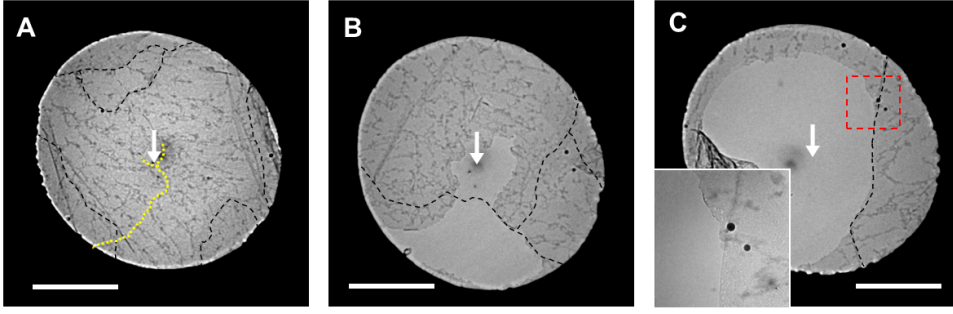
Figure 4.19: TEM observation of crack formation after nanoindentation. (A-C) BF-TEM images shows various graphene fractures when the center of the suspended graphene away from grain boundaries was indented. A crack was formed in indented spot and propagated across grain boundaries as shown by yellow-dashed line in (A). Breaking of graphene along a grain boundary was also observed in (B) and (C). The edges of a crack along grain boundary are smoother than those propagating in the middle of grain as shown in the inset of (C). The scale bar is 1 μm.

4.3.7 Crack propagation during indentation

In particular, when the center of the suspended graphene was indented away from grain boundaries, a crack (yellow-dashed line) is seen to form under the indenter and to propagate toward the edge of hole, crossing the grain boundary as shown in Fig. 4.19A. This result is not in accordance with experimental and theoretical results that mechanical failure always initiates from grain boundaries [88, 114, 123]. Nonetheless, crack propagation along grain boundaries was also observed as shown in Fig. 4.19B and C. Thus, even though a crack formed initially under the indenter away from a grain boundary, it occasionally deflects into and propagates along grain boundaries. Kim *et al.* reported that, when a crack nearby the edge of a hole propagates in suspended graphene as a consequence of electron beam irradiation, the crack propagates along straight lines aligned in the armchair or zigzag directions of the graphene lattice [46]. However, this was not found in our study, likely because different external agents caused the initiation and propagation of cracks. Instead, the edges of cracks along grain boundary are smoother than those in the middle of grains as shown in the inset of Fig. 4.19C.

4.3.8 Main results and implications

1. We measure the mechanical properties of two different types of CVD graphene (small- and large-grain). Our results demonstrate that large-area graphene with mechanical properties comparable to those of pristine graphene can be produced by CVD processes. In addition, the question of how grain boundaries influence the mechanical properties of graphene is fundamental and essential for applications of graphene in flexible electronics, NEMS, sensors, vapor barriers, and composites. Our work experimentally confirms that a grain boundary can be virtually as strong as the pristine lattice and further identifies what factors can deteriorate the mechanical strength. The mechanical properties of grain boundaries in two-dimensional materials are of fundamental interest because they behave differently from those in three-dimensional materials. Our experimental and analytical techniques can be extended to other 2D materials, such as MoS_2, $MoSe_2$, WSe_2, and hBN, and heterostructures, such as graphene-hBN.

2. Our work includes rigorous analysis by a fifth-order nonlinear anisotropic multiscale stress-strain constitutive model incorporated into a detailed finite element analysis, which enables us to determine the strength from the force on the indenter at rupture.

3. Our work demonstrates the mechanical difference between "stitched" and "overlapped" grain boundaries. This finding will guide efforts toward synthesis of strong, large-area graphene. Our finding of the un-stitched "overlapped grain boundary" indicates that growth of well-stitched CVD graphene is necessary for applicability in large-area flexible electronics and mechanical reinforcement applications.

4. A major discrepancy between theory ("The grain boundary is as strong as pristine graphene" in Ref. [28] and [114]) and previous experimental results ("The grain boundary is extremely weak" in Ref. [39] and [88]) had not been explained before our study. Our measurement experimentally validates the theoretical prediction that some grain boundaries can approach the strength of pristine graphene.

5. A second discrepancy is that all of the grain boundaries we tested achieved a streng-

th approaching that of pristine graphene, whereas the theoretical efforts in Refs. [28] and [114] predicted that some grain boundaries would fail at significantly lower stresses. Based upon the failure mechanisms proposed by the theoretical studies, we suggest that this discrepancy may be due to over-simplification of the atomic structure of the grain boundaries assumed in the theoretical studies.

6. The elastic stiffness of CVD graphene measured in Ref. [88] is much smaller than that of pristine graphene because of presence of ripples. Our transfer technique can maintain the flatness of CVD graphene without ripples, resulting in graphene's intrinsic elastic stiffness.

7. Our work also introduces a well-developed technique to study the mechanical properties of grain boundaries in two-dimensional materials. In the previous method of Ref. [88], identification of grain boundaries was performed in AFM imaging by using the presence of processing residue. However, as shown in our work, the residue can be located on the middle of a grain, overlapped grain boundaries, and wrinkles. Therefore, without the combination of AFM and darkfield TEM, it is impossible to find out the type of grain boundaries by AFM alone.

8. We also observed crack propagation when graphene is mechanically indented on or away from grain boundary. This observation shows how the grain boundary acts in two-dimensional materials during fracture. Our work demonstrates that a crack propagates in more complicated way, not like in the simulations (along zigzag or armchair direction)

Chapter 5

Mechanical properties of heterogeneous rigidity in poly(dimethylsiloxane) films induced by electron beam irradiation

5.1 Introduction

Polydimethylsiloxane (PDMS) is a commonly used and well-established thermal-curable, gas-permeable, and bio-compatible material that has found widespread use in microfuidics, microcontact printing and biological studies[119]. PDMS substrates patterned into micron-scale pillars have become an important tool facilitating the measurement and characterization of cellular forces[101]. The mechanical properties and pillar dimensions (i.e. diameter and height) can be varied and quantified to create a real-time cellular force map across the entire cell[24, 102]. A photocatalyst added to PDMS allows one to pattern by photolothography, a useful approach in microfluidics[41]. Untreated PDMS has been shown to be sensitive to deep-UV and e-beam irradiation[16, 26, 89, 108], which induces cross-linking of the elastomer. Previous studies have investigated the surface chemical changes induced by irradiation, this study aims to quantify changes in mechanical properties of e-beam-exposed PDMS.

The mechanical properties of PDMS can vary depending upon a number of factors.

The Young's modulus of spin-coated and drop-cast PDMS can differ by as much as 700% depending upon the film thickness and coating conditions[103]. Changes in the curing temperatures and duration can vary the the modulus as much as 60%[2, 61, 64]. Thermal curing of PDMS has been shown to induce prestrain in the polymer [64]. The base-to-accelerator ratio has the largest effect on the polymer stiffness. A collection of the PDMS modulus values as a function of base-to-accelerator ratio, as reported in the literature, is shown in Figure 5.3. These data lend insight into the variability of the mechanical properties of PDMS–the parameters used in processing the PDMS are detailed in the respective references. The temperature and length of cure time also influences the amount of prestrain and stiffness of PDMS [64].

The ability to selectively vary the stiffness of PDMS can be exploited in a variety of applications. For example, microfluidic channels and valves comprising regions of variable and/or heterogeneous stiffness could be actuated in a geometrically-dependent manner. Similarly, PDMS films with selectively variable stiffness play a critical role in the investigation of cell mechanics.

We have recently developed a process whereby a PDMS film is exposed to an electron beam in a pre-defined pattern, resulting in a surface of locally variable rigidity on the micro- and nanoscale. Dynamic nanoindentation was used to quantify the changes to the mechanical properties of the film. Because most of the electron energy is dissipated within a relatively short range (a few microns at 30 keV) within the PDMS film, the resultant p-roperties are not uniform in the out-of-plane (i.e. Z-direction). We have developed a finite element model (FEM) in order to interpret the results of nanoindentation measurements as a function of applied electron dose and to characterize quantitatively the mechanical properties of the exposed regions of the film. This approach is broadly applicable to materials systems comprising regions and layers with non-uniform mechanical properties, such as cells and other biomaterials, and can thus facilitate better understanding of their mechanical properties.

5.2   Experimental

We now discuss the experimental investigation of the changes in mechanical properties due to e-beam exposure. Surface irradiation of PDMS scises and cross-links polymer chains to increase the cross-link density [37, 92, 93]. PDMS is cured with thermal energy to cross-link dimethylsiloxane into polydimethylsiloxane. This increase in cross-linking induces a volumetric shrinkage [64]. The e-beam exposure increases cross-link density, inducing a transformation strain in the PDMS and modifies its mechanical properties (e.g. elastic and viscoelastic properties). It is therefore necessary to quantify both transformation strain and stiffness variation to accurately predict the mechanical properties of e-beam irradiated PDMS.

The PDMS preparation is detailed in the Supporting Information. The e-beam patterning is accomplished in two ways. An array of 1 μm-diameter evenly spaced in a square grid of 8 μm distances is irradiated on the PDMS surface. Second, a 1 mm × 1 mm area is irradiated. These two irradiated patterns on the PDMS surface provide insight into the prestrain and stiffness changes–as will be discussed in further detail. The irradiated film is estimated to be 3 μm-thick based upon quantum Monte Carlo simulations of electron energy dissipation in the film[1].

The transformed PDMS is constrained on the surface of the otherwise untransformed PDMS film, the transformation strain induces a strain in the untransformed PDMS leading to an undulating surface profile measurable via optical profilometry for the 1 μm-diameter array of exposed areas. The profiles of these arrays are used in a FEM to determine the transformation strain as a function of the exposure dosage.

We describe the viscoelastic behavior of the PDMS by means of a complex shear modulus, which characterizes the ability of the material both to store and damp energy. The complex shear modulus, μ^*, is expressed as

$$\mu^* = \mu_{\text{storage}} + i\mu_{\text{loss}}, \tag{5.1}$$

where the real part, $\Re(\mu^*) = \mu_{\text{storage}}$, characterizes elasticity, and the imaginary part,

$\Im(\mu^*) = \mu_{\text{loss}}$ characterizes damping. Considering μ^* as a phasor with angle δ leads to the loss factor,

$$\tan(\delta) = \mu_{\text{loss}}/\mu_{\text{storage}}, \tag{5.2}$$

which characterizes the damping capacity relative to the storage capacity.

To measure the complex shear modulus of the PDMS, we use an Agilent G200 NanoIndenter with Dynamic Contact Module (DCM) head, fit with a diamond flat-ended cylindrical punch having a radius of 76.4 μm. When testing polymers by instrumented indentation, the flat-ended cylindrical punch is advantageous, because the contact area is constant and known throughout the experiment, even when viscoelasticity and creep are manifest [35, 36]. By means of the Continuous Stiffness Measurement (CSM) option, a normal force oscillation is applied to the indenter while in contact with the PDMS and the characteristics of this oscillation lead directly to the complex shear modulus of the material. The CSM comprises a lock-in amplifier and controlling software; it imposes an oscillating force on the indenter at a specific frequency and measures the amplitude and phase lag of the resulting displacement oscillation at that same frequency.

A single test on the PDMS comprises the following steps: First, with the head well above the sample the indenter oscillates using a force amplitude of $F_i = 20$ μN and a frequency of 110 Hz–this frequency being sufficiently close to the resonant frequency of the nanoindenter to benefit from increased sensitivity. Then, the displacement amplitude, Z_i and phase lag, ϕ_i, are recorded in order to characterize the dynamics of the head in the atmosphere. The head is then brought down to engage the sample; engagement is sensed as a significant shift in the phase lag, ϕ. Following contact, the indenter is pressed into the surface to a depth of 1.5 μm and the displacement amplitude of the oscillations is measured, Z_o. The force amplitude is then set to $F_c = (100 \text{ nm}) F_i/Z_o$. In this way, the force amplitude produces an oscillation of approximately 100 nm. Finally, the displacement amplitude, Z_c, and phase lag, ϕ_c, are measured before disengaging the indenter.

From these prescribed values and direct measurements, the contact stiffness S and

damping $D\omega$ of the contact are calculated as [31]

$$S = F_c/Z_c \cos \phi_c - F_i/Z_i \cos \phi_i \tag{5.3}$$

$$D\omega = F_c/Z_c \sin \phi_c - F_i/Z_i \sin \phi_i. \tag{5.4}$$

The stiffness and damping of the contact are the real and imaginary parts of the stiffness phasor during contact, less the values of those same quantities measured for the head in air in step 2 of the above procedure.

If the thickness of the PDMS is $\times 20$ the contact radius or thicker, then it is straightforward to calculate the components of the complex shear modulus and their ratio[36]

$$
\begin{aligned}
\mu_{\text{storage}} &= S(1-\nu)/(4a), \\
\mu_{\text{loss}} &= D\omega(1-\nu)/(4a), \text{and} \\
\tan(\delta) &= D\omega/S
\end{aligned}
\tag{5.5}
$$

where ν is the Poisson's ratio and a is the radius of the flat-ended cylindrical punch. However, a layered viscoelastic structure–such as PDMS adhered to a glass substrate–has an apparent complex modulus, μ^*_{apparent}, that is influenced by the mechanical properties of the underlying materials. Interpretation of the nanoindentation of layered structures is an inverse problem. The mechanical properties of the constituents must be determined based upon the apparent behavior of the overall layered structure [32, 33, 38, 75, 90]. Equation 5.5 quantifies the *apparent* properties of the e-beam-irradiated PDMS. A FEM is used to model the behavior of the overall PDMS-glass layered structure in order to estimate the influence of the substrate on μ^*_{apparent}.

The e-beam-irradiated PDMS has a higher cross-link density, and as such the stiffness should be higher than the underlying unexposed PDMS. The goal of the nanoindentation investigation and FEM analysis is to determine the change in stiffness as a function of the e-beam dosage. Herein, we define a variable to refer to the ratio of the treated to untreated PDMS modulus as $\Pi \equiv \frac{\Delta \Re(\mu^*_{\text{exposed}})}{\Re(\mu^*_{\text{unexposed}})}$ where $\Re(\mu^*_{\text{apparent}})$ is the real part of μ^*_{apparent} i.e. *apparent* storage modulus. Based upon FEM results μ^*_{apparent} of the PDMS-glass film

is a function of transformational strain, ϵ_0, and Π.

Experimentally, we see that increasing exposure increases $\Re(\mu^*_{\text{apparent}})$ and increases the depth of PDMS sink-in as plotted in 5.1E. Therefore, we postulate that $\Pi = \Pi(\sigma_q)$ and $d = d(\sigma_q)$ where σ_q is the exposure dosage–measured in a charge density of $\frac{\mu C}{cm^2}$– and d is the measured depression depth after e-beam exposure–as seen in the scanning electron microscope image in 5.1A and diagrammed in 5.1B-C. The charge density, σ_q, is a convenient measure of the e-beam treatment. It is not indicative of surface charge density.

Two FEM's are used to determine the mechanical response of the e-beam irradiated PDMS. The first model is designed to determine the amount of transformation strain induced through the process of irradiation. The second model is designed to determine the change in stiffness of the irradiated film based upon the apparent properties of the layered structure.

We now discuss the first FEM used to determine transformational strain, ϵ_0. After e-beam irradiation, the irradiated PDMS experiences a volume reduction and is "pulled"into the film by the surrounding unirradiated PDMS. A periodic pattern of circular areas exposed to 60, 750, 2100, 3400, 4700, and 6000 $\frac{\mu C}{cm^2}$ e-beam doses as seen in the SEM image of 5.1A. The depths measured by optical profilometry are plotted as a function of σ_q in 5.1E.

We model one-fourth of a unit cell of this periodic, undulating structure as detailed in 5.1C. We impose a volumetric shrinkage strain on the 3 µm × 1 µm quarter-cylinder and calculate the depth of depression. We calculate the depth as a function of the imposed strain and cylinder stiffness, $\Pi = 2^n$ where $n = 0, 1, 2, ..., 9$. The imposed volumetric shrinkage is meant to simulate the transformation strain experienced during e-beam irradiation. In this way, the transformation strain is calculated as a function of Π and d as shown in 5.1D.
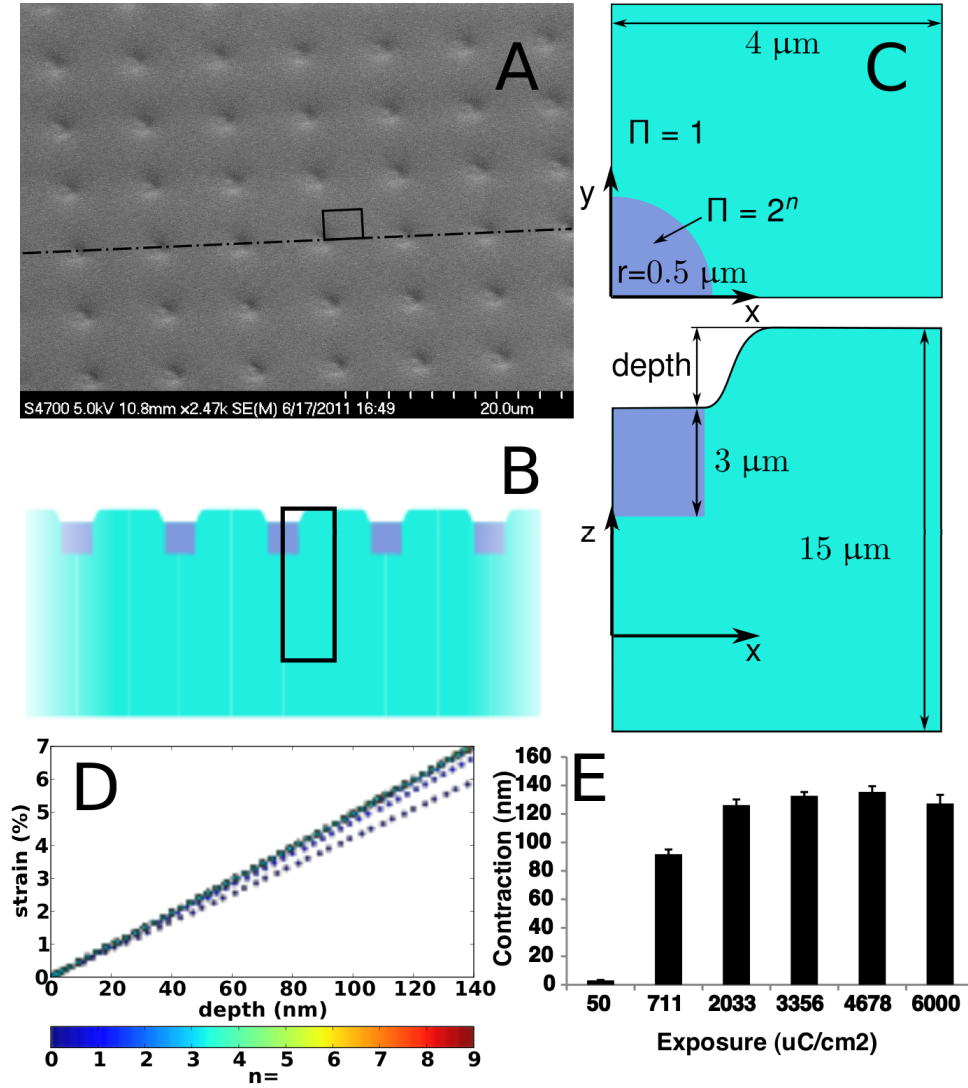
Figure 5.1: Figure 1A is a scanning electron microscope image of the periodic array of irradiated areas. The dashed line in 1A is the cut for 1B with the solid box representing the repeating unit cell that was modelled in the FEM solution. The close-up of the unit cell–as indicated by the rectangles in 1A–is detailed in 1C. 1D shows the FE results as a function of Π and depth and 1E is the experimentally observed depth as a function of e-beam exposure, σ_q

The second FEM is employed to determine $\Pi(\sigma_q)$ based upon the range of ϵ_0 determined by the first FEM. The PDMS is modeled as a linear-viscoelastic material rigidly bonded to a linear-elastic glass substrate. The model schematic is shown in 5.2A. The indenter is modeled as a rigid cylinder with a fillet radius of 100 nm and radius $R = 76.4$ μm. To reduce computational time, nodes in contact with the indenter are tied to the cylinder surface. This simplification essentially imposes an infinite friction coefficient. However, PDMS is a rubbery material so we expect a large coefficient of friction. In the calculation,

the indenter is pushed into the surface of the viscoelastic elements to a depth of 1.5 μm. After relaxation, the tip oscillates sinusoidally with amplitude 500 nm for 5 cycles. The solution converges to steady-state within 3 cycles.

Experimental observations of the mechanical properties are in terms of the μ^*_{apparent} for the layered PDMS structures diagrammed in 5.2A. A 1mm $\times$ 1 mm area is exposed to e-beam exposures $\sigma_q = 0 - 6000 \frac{\mu C}{cm^2}$, the experimental results of these exposures and apparent moduli are given in Table 5.1. As σ_q is varied from $0 - 6000 \frac{\mu C}{cm^2}$, $\Re(\mu^*_{\text{apparent}}) = 1100 - 6200$ kPa and $\tan(\delta) = 0.19 - 0.10$. These apparent properties depend upon the transformational strain, ϵ_0, change in stiffness due to irradiation, $\Pi(\sigma_q)$, and the mechanical properties of the underlying structure, i.e. $\mu^*_{unexposed}$, μ_{glass}, and ν_{glass}.

To determine the function $\Pi(\sigma_q)$, we consider bounds on the apparent mechanical properties due to variations in ϵ_0 and Π, while $\mu^*_{unexposed}$, μ_{glass}, and ν_{glass} remain constant between nanoindentations. The first FEM determines that $\epsilon_0 = 0\%$–6% as σ_q increases. The first data point for the lower bound of prestrain and material properties is taken as $\Pi = 0$ and $\epsilon_0 = 0\%$. This point corresponds to an unexposed area of PDMS i.e. no transformational strain and no increase in rigidity. We increase Π with $\epsilon_0 = 6\%$ in the film until the highest value of apparent modulus is calculated–$\Pi = 580$, $\Re(\mu^*_{\text{apparent}}) = 6200$ kPa. This data point is employed as the upper bound for the FEM calculations. In determining the function $\Pi(\sigma_q)$, these two values are taken as the boundary values of the function, i.e. $\Pi(0 \frac{\mu C}{cm^2}) = 0$ and $\Pi(6000 \frac{\mu C}{cm^2}) = 580$. The FEM solution is then used to fill in apparent material properties for $\Pi = 0 - 580$ and $\epsilon_0 = 0\% - 6\%$. The upper and lower bounds for apparent properties are illustrated in 5.2B-C by the red, dashed line and blue, solid line, respectively. The red, dashed line represents the apparent modulus as a function of the increase in rigidity due to e-beam irradiation for the highest expected prestrain, $\epsilon_0 = 6\%$. The experimental apparent moduli are measured as a function of e-beam exposure, σ_q as listed in Table 5.1. We next provide a functional relationship between Π and σ_q that maps the data between the upper and lower bound calculated via FEM.

5.3 Results

The cross-linking due to e-beam irradiation is a stochastic process that scises bonds and creates multiple junction types [37, 92, 93]. There is no inherent reason to assume that the dosage of e-beam irradiation will linearly increase the stiffness of PDMS. We assume that the functional relationship between Π and σ_q is C^0 continuous, monotonic, and that the first derivative does not approach infinity. Under these assumptions, the simplest relation–barring a direct linear relation, which does not capture the observed behavior of the exposed PDMS under nanoindentation–is two linear functions. The boundary conditions of the relationship are determined by the two points: $\Pi(0 \, \frac{\mu C}{cm^2}) = 0$ and $\Pi(6000 \, \frac{\mu C}{cm^2}) = 580$. Using these two boundary conditions, and assuming that two regimes exist with distinct slopes, we execute a brute-force minimization routine to fit the data within the FEM calculated bounds of $\Re(\mu^*_{apparent})$ and $\tan(\delta_{apparent})$.

The minimization is achieved by varying the two slopes that define the two regimes of stiffening as affected by e-beam irradiation. The experimental data and bounds are shown in 5.2C-D for $\Re(\mu^*_{apparent})$ and $\tan(\delta_{apparent})$, respectively. The optimization assigns an error of $1/N$ for each data point that is mapped outside of the bounds calculated by the second FEM, where N is the number of experimental data points mapped. The optimized function results in

$$
\Pi = \begin{cases}
3.05 \frac{cm^2}{\mu C} \sigma_q, & \text{if } 0 \frac{\mu C}{cm^2} \leq \sigma_q \leq 145 \frac{\mu C}{cm^2} \\
0.024 \frac{cm^2}{\mu C} (\sigma_q - 6000 \frac{\mu C}{cm^2}) + 580, & \text{if } 145 \frac{\mu C}{cm^2} < \sigma_q \leq 6000 \frac{\mu C}{cm^2}
\end{cases} . \tag{5.6}
$$

This functional relation helps to elucidate the effect of e-beam irradiation on the mechanical properties of PDMS films, plotted in 5.2B. Fitting the data to these two linear functions, the predictive error between the model reduces from 0.36–a direct linear fit–to 0.01–a function with two linear regions.

Equation 5.6 has two linear regimes to describe the increase in stiffness as a function of e-beam exposure. The initial linear regime–for $\sigma_q \leq 145 \, \frac{\mu C}{cm^2}$–compounds a nonlinear mechanical response with an unknown function of cross-linking due to e-beam irradiation. As the value of Π increases, the mechanical response becomes more linear as seen in 5.2C
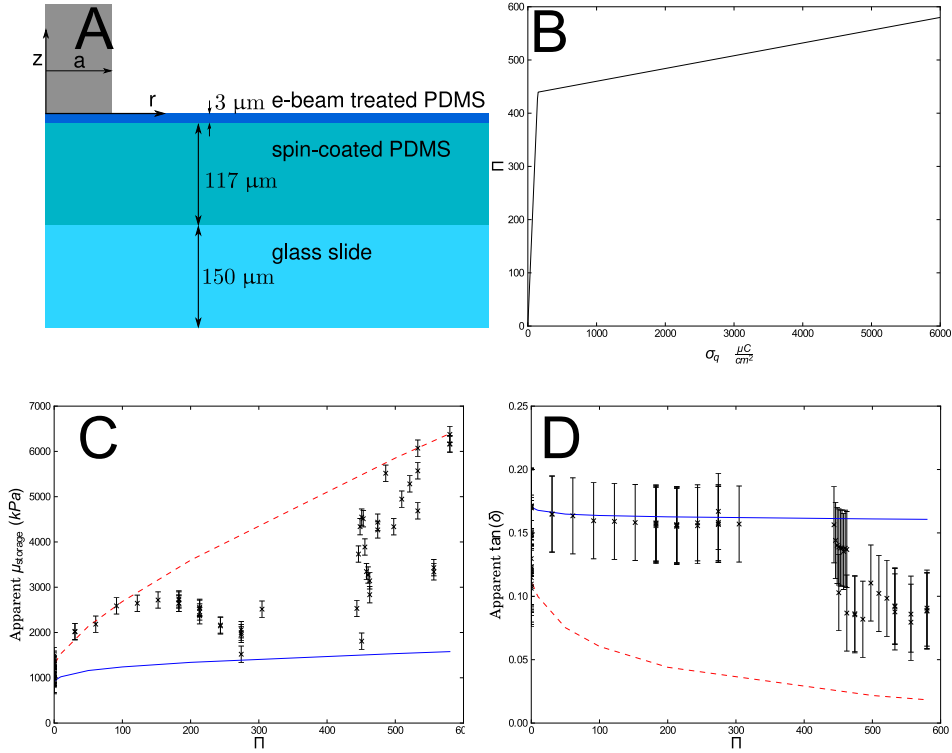
Figure 5.2: Figure 2A is a graphical representation of the FEM used to determine the apparent properties of a viscoelastic layered material–e-beam exposed PDMS–rigidly bonded to an elastic substrate–glass. Equation 5.6 is plotted in 2B showing the two linear regimes of e-beam irradiation stiffening. Plotted in 2C-D is the resulting apparent μ_{storage} and $\tan{(\delta)}$ as a function of Π for the e-beam exposed $3\ \mu\mathrm{m}$ film. The red dashed and blue solid lines are the bounds set by the material properties and prestrain on the film. The red line sets $\epsilon_0 = 6\%$ and the blue line sets $\epsilon_0 = 0\%$. The black $\times$ data points in 2C-D are the nanoindentation results plotted by use of a brute-force optimization to determine the function of $\Pi(\sigma_q)$, determined to be Equation 5.6. The error bars indicate the standard deviation in apparent properties of the data at $\Pi = 0$, $\sigma_q = 0\ \frac{\mu\mathrm{C}}{\mathrm{cm}^2}$.

and D. We have assumed two linear regimes, but the actual influence of e-beam irradiation on the surface of PDMS could be more complex. The goal here is to gather as much insight into the stiffening of e-beam-irradiated-PDMS without overstating the knowledge gained from these experiments.

5.4 Outlook

In conclusion, we have–within experimental uncertainty–determined a functional relationship between e-beam irradiation and PDMS mechanical properties. The mechanical properties of PDMS can be tailored to suit a variety of applications. Our description of

highly localized variation of PDMS mechanical properties extends the range of applications possible for this versatile material, from biomimetic surfaces for studying cellular mechanotransduction to microfluidic devices with locally varying stiffness actuators. It should also be possible to use the localized increased stiffness of PDMS to shield delicate components from large strains induced by bulk deformations of a flexible substrate–as has been done with composite structures for flexible electronics [87]. The results and methodology presented herein are broadly applicable in the understanding of complex mechanical systems.

5.5 Materials and Methods

5.5.1 PDMS preparation

Standard microscope cover-glasses were cleaned for 12 h in a 1% v/v solution of the detergent MICRO-90 (International Products, NJ, USA), rinsed in reverse osmosis water (ROH_2O) and blown-dry in a stream of filtered nitrogen. The samples are prepared by mixing Sylgard 184 PDMS (Dow Corning, MI, USA) with a 50:1 ratio to the included accelerator and degassed at 5 Torr for 10 min. The uncured PDMS mixture is then applied to a microscope cover-glass and spin-coated for 45 s at 1000 rpm with an acceleration of 400 rpm/s resulting in a film 120 μm thick. PDMS (0.5 ml) was applied to the microscope cover-glasses and spin-coated for 45 s at 1000 r.p.m. and an acceleration of 400 rpm/s to form a uniform film. PDMS-coated cover-glasses were cured for for 17 h before further processing. Substrates were subjected to an oxygen plasma in a tabletop Harrick PDC32G plasma cleaner for 10 sec at a RF power of 18 W to induce surface hydrophilicity. Samples were next coated with a conductive discharge layer to facilitate electron beam exposure. A 5 nm thick discharge layer was applied to the substrates by spin coating 100 ul of Aquasave (Mitsubishi Rayon) for 45 s at 4000 rpm and an acceleration of 400 rpm/s. Samples were stored at RT until e-beam exposure.

The PDMS substrates were patterned by e-beam exposure using a scanning electron microscope (FEI XL 30 Sirion) equipped with a Nabity NPGS pattern generator. The

exposures used an accelerating voltage of 30 kV and a beam current of $\approx$2.5 nA. Substrates were cleared of Aquasave in deionized water for 3-5 min and allowed to air dry for 30 min.

5.5.2 Finite Element details

Abaqus uses a Prony series to define viscoelastic materials [97]. Here we use a first-order Prony series model, where the time-dependent Young's modulus is defined as $E(t) = E_\infty + \sum_{i=1}^{n_E} E_i \exp\left(-t/\tau_i\right)$ and E_∞ is the modulus at $t = \infty$ while E_i and τ_i are the viscoelastic terms to describe the time-dependent modulus. Our model used a single Prony series term and we normalized the time by the time-constant to simplify the material parameters. This is appropriate because we only wished to characterize the layered material response at the testing frequency of 110 Hz. The input parameters for Abaqus then include the modulus at $t = \infty$, E_∞, and a factor relating the modulus at $E(t = \infty)$ to $E(t = 0)$ defined as $g = 1 - E_\infty/E_0$. The relationship between the complex modulus and time dependent modulus is as follows

$$
\begin{aligned}
g &= \frac{((\mu_{\text{storage}}+\mu_{\text{loss}})^2+\mu_{\text{storage}}^2-2\mu_{\text{storage}}(\mu_{\text{storage}}+\mu_{\text{loss}})+\mu_{\text{loss}}^2)}{((\mu_{\text{storage}}+\mu_{\text{loss}})^2-\mu_{\text{storage}}(\mu_{\text{storage}}+\mu_{\text{loss}}))} \\
E_\infty &= 3(1-g)(\mu_{\text{loss}} + \mu_{\text{storage}})
\end{aligned}
\tag{5.7}
$$

Using these equations, we converted between the complex modulus and the input parameters for Abaqus, E_∞ and g at the testing frequency. Equations 5.7 are necessary because the experimental results are in terms of storage and loss modulus while the Prony series viscoelastic material description used in Abaqus depends on the Young's modulus as a function of time.

The first model consisted of 25,379 nodes and 22,680 8-node quadrilateral elements. A quarter-disk at the corner of the model was assigned a modulus $2^n E_{substrate}$, where $n = 0..9$ and $E_{substrate}$ was the Young's modulus of the rectangular column as seen in the schematic in Figure 1A. The model did not account for mass losses that may occur during irradiation.

The second model was comprised of 2760 4-node axisymmetric elements and 2867

nodes for the 120 μm thick PDMS simulation. The indenter was modeled as a rigid cylinder with a fillet radius of 100 nm and $R = 76.4$ μm. Each time step was $\frac{T}{91}$ where T is the period of the oscillations. The apparent complex modulus was then calculated using equations 2.

A bulk, cast PDMS was used to verify the FE calculations. In the bulk material, the apparent properties are equivalent to the material properties. The storage modulus and $\tan(\delta)$ were measured to be 94.6 kPa and 0.41, respectively. Using equations 5.7, $E_\infty = 0.17$ kPa and $g = 0.59$. These material parameters were entered and used to solve the semi-infinite, axisymmetric FE model. The FE model consisted of a 6000 μm thick PDMS layer rigidly fixed to a linear-elastic, glass substrate in the FE model. The resulting apparent properties were $\bar{}_{storage} = 95$ kPa and $\tan(\delta) = 0.4$–equivalent to the material properties input into the model. This analysis served as a verification that the FE solution converged to the desired solution for a semi-infinite viscoelastic solid subject to indentation by a rigid flat-punch.

The determination of the spin-coated PDMS was essential to the investigation of the exposed PDMS mechanical properties. The experimentally measured storage and loss moduli of e-beam exposed PDMS are highly influenced by the properties of the underlying unexposed PDMS properties. By first determining the mechanical properties of spin-coated PDMS, we then investigated the mechanical properties of the exposed region. The measurement of the modulus for the bulk and spin-coated PDMS was compared to other mechanical tests of PDMS of different base-to-accelerator ratios in 5.3 represented by the lower and upper + symbols, respectively. Both values were within the expected range of modulus values for PDMS.
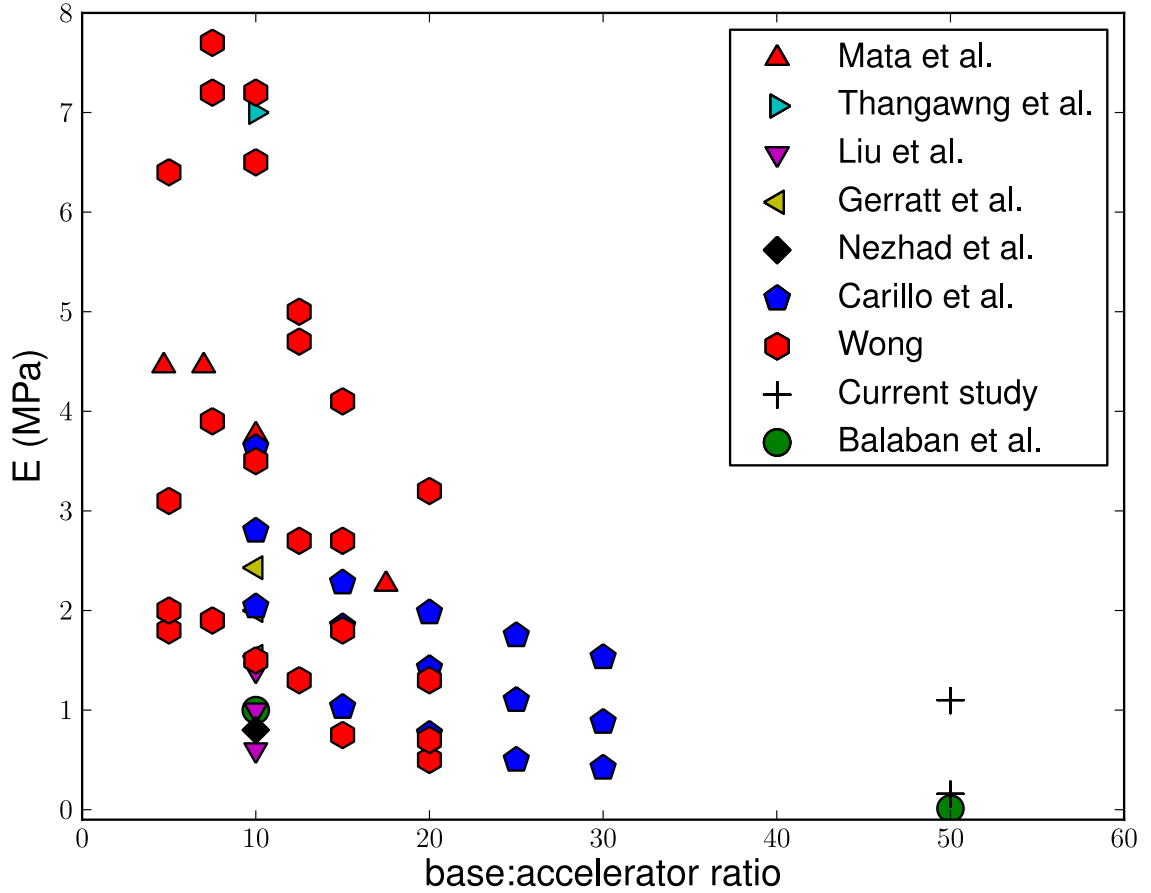
Figure 5.3: Plotted here is the Young's modulus of PDMS as a function of the base-to-accelerator ratio measured by different research groups using different preparation techniques and measurement methods. [4, 12, 23, 61, 64, 91, 103, 116] The upper and lower + symbols are the measurements of 50:1 PDMS moduli for spin-coated and cast PDMS in the current study, respectively.

Experimental data points were compared to the FE bounds on apparent properties. The experimental data that fell outside of the bounds were assigned a uniform error of (number of data points)$^{-1}$ otherwise no error was assigned. The sum of function errors was calculated between the bounds of $m_1 = m_{lin}..42m_{lin}$ and $m_2 = 0.01m_{lin}..m_{lin}$ in a grid of 75072 solutions, where m_{lin} refers to a direct linear function of $\Pi(\sigma_q)$. As the solution tended towards a step function–i.e. $m_1 \gg m_{lin}$ and $m_2 \ll m_{lin}$–a uniform floor error was achieved. We assumed that the smallest value of m_1 and largest value of m_2 that achieved the minimum floor error were the optimized linear regimes that describe the relationship between e-beam dosage and Young's modulus. The experimentally measured

values for the storage modulus and $\tan(\delta)$ are shown in Table 5.1.

$\sigma_q \left(\frac{\mu C}{cm^2} \right)$	$\Re(\mu^*_{apparent})$ (kPa)	$\tan(\delta_{apparent})$	$\sigma_q \left(\frac{\mu C}{cm^2} \right)$	$\Re(\mu^*_{apparent})$ (kPa)	$\tan(\delta_{apparent})$
0	1130±180	0.14±0.02	400	4338	0.14
10	2015	0.16	500	4549	0.14
10	2025	0.16	500	1809	0.10
20	2184	0.16	600	4513	0.14
30	2588	0.16	700	3889	0.14
40	2646	0.16	800	3346	0.14
50	2718	0.16	900	3270	0.14
60	2646	0.16	1000	3141	0.14
60	2718	0.16	1000	2835	0.09
60	2647	0.16	1500	4437	0.09
60	2742	0.16	1500	4266	0.09
70	2534	0.16	2000	5518	0.08
70	2556	0.16	2500	4336	0.11
70	2454	0.16	3000	4946	0.10
70	2370	0.16	3500	5283	0.10
80	2165	0.16	4000	4687	0.09
80	2146	0.16	4000	6072	0.09
90	2062	0.16	4000	5571	0.09
90	1958	0.16	5000	3432	0.08
90	1999	0.16	5000	3340	0.09
90	1521	0.17	6000	6168	0.09
100	2516	0.16	6000	6161	0.09
200	2532	0.16	6000	6375	0.09
300	3733	0.14			

Table 5.1: Experimental results from nanoindentation on e-beam-exposed PDMS films. The apparent properties of storage modulus in kPa and $\tan(\delta)$ are given for reference. The bounds on measured properties for no exposure is the standard deviation in experimental measurements for 20 indentations.

Chapter 6

Conclusions and Future Work

In conclusion, these experimental and numerical techniques provide a framework for determining the mechanical properties of a variety of thin film materials. I provide a detailed account of dealing with both material and geometrical nonlinearities that I encounter during nanoindentation of thin films. For future reference, I have included Appendices of procedures for substrate fabrication, AFM nanoindentation, and the procedure for using the 2D material nanoindentation method for the Agilent G200 nanoindenter. This work has three main accomplishments. First, I provide novel implementation of nanoindentation techniques. Second, the mechanical properties of the thin films provide new results interesting for basic science. Third, quantifying these mechanical properties helps in the process of transferring these technologies to industrial solutions.

These methods help to show the breadth of possibilities for implementing nanoindentation as a means of monitoring thin film properties for quality control or process monitoring. In the case of 2D crystals–detailed in chapters 2-4, one could imagine using these fracture loads with a chart of material strengths to ensure chemical vapor deposition methods are consistent between processes. In the case of locally varied PDMS properties reported in chapter 5, one could monitor the changes in microfilm stiffness as electron beam irradiation is applied. Chapter 5 goes through this process methodically.

The results of chapters 2-4 demonstrate the high mechanical integrity of 2D crystals. These results parallelize computational and experimental techniques in an effort to

provide innovative techniques for new material design. The experimental validation of first-principles multiscale modeling allows one to design the next material solutions with insight from computational results, thus reducing the cycle of trial-and-error.

The high strength of CVD graphene necessitates a more thorough investigation of the role of grain boundaries in 2D materials. Polycrystalline metals have been shown to exhibit higher strength [65] as grain size decreases. Graphene with symmetric tilt grain boundaries is estimated to reduce the strength of the crystal [114]. The experiments of chapter 4 do in fact show a slight decrease in strength as grain boundaries are introduced, but not to the extent that Wei *et al.* predict [114]. Looking forward, it will be interesting to see more data correlating the grain boundary orientations and fracture force.

Further work is also necessary to estimate the effect of random defects the nanoindentation analysis of failure. Previous work estimated that because the state of stress under the nanoindenter tip is uniform and that fracture would occur at the highest point of stress under the tip [58]. This assumption is valid for a pristine sheet of graphene. If one is concerned with the weakening effects of defects in the membrane, then the state of stress of the entire strained membrane must be integrated into the prediction of failure due to a weakening defect. This will be especially important as different grain orientations are stitched together and symmetry in the stress state is lost. Weibull provided a generalized form of the "weakest link" theory in 1939 [115]. This theory can be incorporated into the finite element analysis routine with experimentally measured grain boundary geometries and subject to loading by spherical indentation. One can then approximate a risk of rupture–or probability of failure–depending on a Weibull modulus.

If graphene's high mechanical strength is to be utilized in new technologies, it is imperative to investigate multiple scales of defects due to processing. The work in chapter 4 investigates the effect of nanostructural defects on the strength of graphene. The introduction of grain boundaries changes the orientation and number of covalent bonds between carbon atoms in graphene. There is no evidence that suggests this will significantly reduce the strength. The next level of investigation should explore the effect of microstructural defects in graphene.

The electron beam irradiation of PDMS provides a foundation for further investigation. The preparation methods of PDMS have been researched extensively. I have tried to highlight the main components that affect PDMS stiffness i.e. casting method (spinning, casting, molding, etc.), curing thermal history (temperature and time), and accelerating agent. To quantify the changes in the stiffness, it is first necessary to have consistent samples. The thickness of the irradiated sections was estimated based upon Monte Carlo calculations [1]. This thickness should be validated with experimental measurement–possibilities include cross-sectioning and performing measurements with AFM, SEM, or optical microscopy. The study investigates the stiffening of PDMS with the hypothesis that cross-link density increases through irradiation.

A statistical mechanics analysis of cross-linked polymer chains in a rubber estimates the small strain modulus to be proportional to the cross-link density–assuming the length of polymer chains is constant and only cross-link density increases[20, 34]. The stochastic nature of electron beam irradiation of PDMS means that both chain length and cross-link density could be changing in unknown ways. This is why I do not attempt to calculate the change in cross-link density as a function of electron irradiation in Chapter 5. Further work is needed to characterize the change in polymer chain length (i.e. molecular weight) and cross-link density as a function of e-beam irradiation.

Aside from the characterization of the heterogeneous PDMS microfilms, these films have already found use in biomimetic surfaces to monitor the growth of stem cells [6]. In chapter 5.4 I mention the possibility of shielding sensitive components from large strains using e-beam irradiation for flexible electronics. The results indicate that the stiffness increases $\approx 500\times$. This could easily protect a thin electrode from large strains in a rubber-electronics interface. This problem represents a prime example of when the primary objective may be electrodes, light emitting diodes, or otherwise, but because the substrate is flexible an innovative solution is necessary to accomplish the task.

The results of this thesis could also be used as groundwork for two dimensional electrodes adhered to microfilms of PDMS with user-defined stiffened platforms. This project is interesting for both basic science and industry-strengthening innovation. The effects

of strain on 2D material electrical properties is still being explored [83]. Locally varied rigidity could serve as a tool to concentrate strained regions for electrical characterization in new configurations. Both graphene and MoS_2 fail at strains of $\approx 25\%$ so it is reasonable to imagine a device that contorts and flexes–such as PDMS–with 2D conductors and semiconductors. The sensitive connections for such a device–such as soldered joints that fail at much lower strains–could be bonded to an electron beam irradiated area with much higher stiffness. These systems could be designed for the basic science investigation of electromechanical coupling in two dimensional films or for a substitute to traditional silicon microdevices. In this manner, the work presented in chapters 2-5 can be used to guide further experiments involving two dimensional electronics adhered to PDMS microfilms for new flexible electronics.

In conclusion, I have successfully characterized the mechanical properties of three novel thin films. First, I characterized the nonlinear elastic properties of two dimensional molybdenum disulfide. Secondly, I characterized the nonlinear elastic properties of chemical vapor deposited graphene and directly compare it to previous work on exfoliated (or pristine) graphene. Finally, I measured the viscoelastic properties of PDMS microfilms and determine the change in stiffness as a function of electron beam irradiation. These projects span multiple time and length scales to provide new experimental and numerical techniques for characterization of new thin film materials.

Bibliography

[1] "`http://www.gel.usherbrooke.ca/casino/`".

[2] Caroline Armbruster, Matthias Schneider, Stefan Schumann, Katharina Gamerdinger, Maximiliano Cuevas, Sophie Rausch, Gerhard Baaken, and Josef Guttmann. Characteristics of highly flexible pdms membranes for long-term mechanostimulation of biological tissue. *Journal of Biomedical Materials Research Part B: Applied Biomaterials*, 91(2):700–705, 2009.

[3] A. Ayari, E. Cobas, O. Ogundadegbe, and M. Fuhrer. Realization and electrical characterization of ultrathin crystals of layered transition-metal dichalcogenides. *Journal of Applied Physics*, 101(1):014507, 2007.

[4] Nathalie Q Balaban, Ulrich S Schwarz, Daniel Riveline, Polina Goichberg, Gila Tzur, Ilana Sabanay, Diana Mahalu, Sam Safran, Alexander Bershadsky, Lia Addadi, et al. Force and focal adhesion assembly: a close relationship studied using elastic micropatterned substrates. *Nature cell biology*, 3(5):466–472, 2001.

[5] S. Bertolazzi, J. Brivio, and A. Kis. Stretching and breaking of ultrathin MoS_2. *ACS Nano*, 2011.

[6] Manus J. P. Biggs, Ryan C. Cooper, J. Liao, Teresa Fazio, Carl Dahlberg, Daniel Moskowitzand Jeffrey W. Kysar, and Shalom J. Wind. Cellular response to surfaces with nanoscale heterogeneous rigidity. *to be submitted.*

[7] P. E. Blöchl. Projector augmented-wave method. *Phys. Rev. B*, 50:17953, 1994.

[8] Th. Böker, R. Severin, A. Müller, C. Janowitz, R. Manzke, D. Voß, P. Krüger, A. Mazur, and J. Pollmann. Band structure of MoS_2, $MoSe_2$, and α-$MoTe_2$: Angle-resolved photoelectron spectroscopy and *ab initio* calculations. *Phys. Rev. B*, 64:235305, Nov 2001.

[9] T. J. Booth, F. Pizzocchero, H. Andersen, T. W. Hansen, J. B. Wagner, J. R. Jinschek, R. E. Dunin-Borkowski, O. Hansen, and P. Boggild. Discrete dynamics of nanoparticle channelling in suspended graphene. *Nano Letters*, 11(7):2689–2692, 2011.

[10] M Bouty. Pressures caused by electrodeposits. *Compt. rend*, 88(714):187, 1879.

[11] JR Cahoon, WH Broughton, and AR Kutzak. The determination of yield strength from hardness measurements. *Metallurgical Transactions*, 2(7):1979–1983, 1971.

[12] Fernando Carrillo, Shikha Gupta, Mehdi Balooch, Sally J Marshall, Grayson W Marshall, Lisa Pruitt, and Christian M Puttlitz. Nanoindentation of polydimethylsiloxane elastomers: Effect of crosslinking, work of adhesion, and fluid environment on elastic modulus. *Journal of materials research*, 20(10):2820–2830, 2005.

[13] R. C. Cooper, C. Lee, C. A. Marianetti, X. Wei, J. Hone, and J. W. Kysar. Non-linear elastic behavior of two-dimensional molybdenum disulfide. *Physical Review B*, 87(3):035423, 2013.

[14] R. C. Cooper, C. A. Marianetti, and J. W. Kysar. In review.

[15] M.A. Crisfield. *Non-linear finite element analysis of solids and structures*. Number v. 2 in Non-linear Finite Element Analysis of Solids and Structures. Wiley, 1997.

[16] JM DeSimone, GA York, JE McGrath, AS Gozdz, and MJ Bowden. Synthesis, bulk, surface and microlithographic characterization of poly (1-butene sulfone)-g-poly (dimethylsiloxane). *Macromolecules*, 24(19):5330–5339, 1991.

[17] F. Ernst, M. W. Finnis, A. Koch, C. Schmidt, B. Straumal, and W. Gust. Structure

and energy of twin boundaries in copper. *Zeitschrift Fur Metallkunde*, 87(11):911–922, 1996.

[18] D.K. Felbeck and A.G. Atkins. *Strength and fracture of engineering solids*. Prentice-Hall, 1984.

[19] A C Fischer-Cripps. Critical review of analysis and interpretation of nanoindentation test data. *Surface and coatings technology*, 200(14):4153–4165, 2006.

[20] Paul J Flory. Network structure and the elastic properties of vulcanized rubber. *Chemical reviews*, 35(1):51–75, 1944.

[21] Fausto G. Fumi. Third-order elastic coefficients in trigonal and hexagonal crystals. *Phys. Rev.*, 86:561–561, May 1952.

[22] A.K. Geim and K.S. Novoselov. The rise of graphene. *Nature Materials*, 2007.

[23] Aaron P Gerratt, Ivan Penskiy, and Sarah Bergbreiter. In situ characterization of pdms in soi-mems. *Journal of Micromechanics and Microengineering*, 23(4):045003, 2013.

[24] Saba Ghassemi, Giovanni Meacci, Shuaimin Liu, Alexander A Gondarenko, Anurag Mathur, Pere Roca-Cusachs, Michael P Sheetz, and James Hone. Cells test substrate rigidity by local contractions on submicrometer pillars. *Proceedings of the National Academy of Sciences*, 109(14):5328–5333, 2012.

[25] P. Giannozzi, S. Baroni, N. Bonini, M. Calandra, R. Car, C. Cavazzoni, D. Ceresoli, G. L. Chiarotti, M. Cococcioni, I. Dabo, A. Dal corso, S. deGironcoli, S. Fabris, G. Fratesi, R. Gebauer, U. Gerstmann, C. Gougoussis, A. Kokalj, M. Lazzeri, L. Martin-samos, N. Marzari, F. Mauri, R. Mazzarello, S. Paolini, A. Pasquarello, L. Paulatto, C. Sbraccia, S. Scandolo, G. Sclauzero, A. P. Seitsonen, A. Smogunov, P. Umari, and R. M. Wentzcovitch. Quantum espresso: a modular and open-source software project for quantum simulations of materials. *Journal Of Physics-condensed Matter*, 21:395502, 2009.

[26] Radhashyam Giri, MS Sureshkumar, K Naskar, YK Bharadwaj, KSS Sarma, S Sabharwal, and GB Nando. Electron beam irradiation of lldpe and pdms rubber blends: Studies on the physicomechanical properties. *Advances in Polymer Technology*, 27(2):98–107, 2008.

[27] X. Gonze, B. Amadon, P. Anglade, J. Beuken, F. Bottin, P. Boulanger, F. Bruneval, D. Caliste, R. Caracas, M. Cote, T. Deutsch, L. Genovese, P. Ghosez, M. Giantomassi, S. Goedecker, D. Hamann, P. Hermet, F. Jollet, G. Jomard, S. Leroux, M. Mancini, S. Mazevet, M. Oliveira, G. Onida, Y. Pouillon, T. Rangel, G. Rignanese, D. Sangalli, R. Shaltaf, M. Torrent, M. Verstraete, G. Zerah, and J. Zwanziger. Abinit: first-principles approach to material and nanosystem properties. *Computer Physics Communications*, 180:2582, 2009.

[28] R. Grantab, V. B. Shenoy, and R. S. Ruoff. Anomalous strength characteristics of tilt grain boundaries in graphene. *Science*, 330(6006):946–948, 2010.

[29] Julia R Greer, Ju-Young Kim, and Michael J Burek. The in-situ mechanical testing of nanoscale single-crystalline nanopillars. *JOM*, 61(12):19–25, 2009.

[30] A. A. Griffith. The phenomena of rupture and flow in solids. *Philos. Trans. R. Soc. London Ser. A*, 221(582-593):163–198, 1921.

[31] J. Hay, P. Agee, and E. Herbert. Continuous stiffness measurement during instrumented indentation testing. *Experimental Techniques*, 34(3):86–94, 2010.

[32] Jack C Hay and GM Pharr. Critical issues in measuring the mechanical properties of hard films on soft substrates by nanoindentation techniques. In *MRS Proceedings*, volume 505. Cambridge Univ Press, 1997.

[33] Jennifer Hay and Bryan Crawford. Measuring substrate-independent modulus of thin films. *Journal of Materials Research*, 26(06):727–738, 2011.

[34] G Heinrich, E Straube, and G Helmis. Rubber elasticity of polymer networks: theories. In *Polymer Physics*, pages 33–87. Springer, 1988.

[35] EG Herbert, WC Oliver, A Lumsdaine, and George Mathews Pharr. Measuring the constitutive behavior of viscoelastic solids in the time and frequency domain using flat punch nanoindentation. *Journal of Materials Research*, 24(03):626–637, 2009.

[36] EG Herbert, WC Oliver, and GM Pharr. Nanoindentation and the dynamic characterization of viscoelastic solids. *Journal of Physics D: Applied Physics*, 41(7):074021, 2008.

[37] David JT Hill, Christopher ML Preston, Daniel J Salisbury, and Andrew K Whittaker. Molecular weight changes and scission and crosslinking in poly (dimethyl siloxane) on gamma radiolysis. *Radiation Physics and Chemistry*, 62(1):11–17, 2001.

[38] Gao Huajian, Chiu Cheng-Hsin, and Lee Jin. Elastic contact versus indentation modeling of multi-layered materials. *International Journal of Solids and Structures*, 29(20):2471–2492, 1992.

[39] P. Y. Huang, C. S. Ruiz-Vargas, A. M. van der Zande, W. S. Whitney, M. P. Levendorf, J. W. Kevek, S. Garg, J. S. Alden, C. J. Hustedt, Y. Zhu, J. Park, P. L. McEuen, and D. A. Muller. Grains and grain boundaries in single-layer graphene atomic patchwork quilts. *Nature*, 469(7330):389–392, 2011.

[40] S. Jiménez Sandoval, D. Yang, R.F. Frindt, and J.C. Irwin. Raman study and lattice dynamics of single molecular layers of $mos2$. *Phys. Rev. B*, 44(8):3955–3962, Aug 1991.

[41] P Jothimuthu, A Carroll, A Asgar S Bhagat, G Lin, J E Mark, and I Papautsky. Photodefinable pdms thin films for microfabrication applications. *Journal of Micromechanics and Microengineering*, 19(4):045024, 2009.

[42] Y. Kadowaki, K. Aika, H. Kondoh, and H. Nozoye. Surface structure of $MoS_2(001)$ determined by coaxial impact-collision ion scattering spectroscopy (caiciss). *Surface Science*, 287-288(Part 1):396 – 399, 1993.

[43] K. K. Kam and B. A. Parkinson. Detailed photocurrent spectroscopy of the semiconducting group vib transition metal dichalcogenides. *The Journal of Physical Chemistry*, 86(4):463–467, 1982.

[44] A. Kelly and N.H. Macmillan. *Strong solids.* Monographs on the physics and chemistry of materials. Clarendon Press, 1986.

[45] D.H. Killeffer. *Molybdenum compounds, their chemistry and technology.* Interscience Publishers, N.Y., 1952.

[46] D. W. Kim, Y. H. Kim, H. S. Jeong, and H. T. Jung. Direct visualization of large-area graphene domains and boundaries by optical birefringency. *Nature Nanotechnology*, 7(1):29–34, 2012.

[47] K. Kim, V. I. Artyukhov, W. Regan, Y. Y. Liu, M. F. Crommie, B. I. Yakobson, and A. Zettl. Ripping graphene: Preferred directions. *Nano Letters*, 12(1):293–297, 2012.

[48] K. Kim, Z. Lee, W. Regan, C. Kisielowski, M. F. Crommie, and A. Zettl. Grain boundary mapping in polycrystalline graphene. *ACS Nano*, 5(3):2142–2146, 2011.

[49] A. Kis, D. Mihailovic, M. Remskar, A. Mrzel, A. Jesih, I. Piwonski, A. Kulik, W. Benoît, and L. Forró. Shear and young's moduli of mos2 nanotube ropes. *Advanced Materials*, 15:733–736, 2003.

[50] G. Kresse and J. Furthmüller. Efficiency of ab-initio total energy calculations for metals and semiconductors using a plane-wave basis set. *Comput. Mat. Sci.*, 6:15, 1996.

[51] G. Kresse and J. Furthmüller. Efficient iterative schemes for *ab initio* total-energy calculations using a plane-wave basis set. *Phys. Rev. B*, 54:11169, 1996.

[52] G. Kresse and J. Hafner. *Ab initio* molecular dynamics for liquid metals. *Phys. Rev. B*, 47:558, 1993.

[53] G. Kresse and J. Hafner. *Ab initio* molecular-dynamics simulation of the liquid-metal-amorphous-semiconductor transition in germanium. *Phys. Rev. B*, 49:14251, 1994.

[54] G. Kresse and D. Joubert. From ultrasoft pseudopotentials to the projector augmented-wave method. *Phys. Rev. B*, 59:1758, 1999.

[55] T. S. G. Krishnamurty. Fourth-order elastic coefficients in crystals. *Acta Crystallographica*, 16(8):839–840, Aug 1963.

[56] A. Kuc, N. Zibouche, and T. Heine. Influence of quantum confinement on the electronic structure of the transition metal sulfide TS_2. *Phys. Rev. B*, 83:245213, Jun 2011.

[57] S. Lebègue and O. Eriksson. Electronic structure of two-dimensional crystals from *ab initio* theory. *Phys. Rev. B*, 79:115409, Mar 2009.

[58] C. Lee, X. D. Wei, J. W. Kysar, and J. Hone. Measurement of the elastic properties and intrinsic strength of monolayer graphene. *Science*, 321(5887):385–388, 2008.

[59] T. Li. Ideal strength and phonon instability in single-layer MoS_2. *Phys. Rev. B*, 85:235407, Jun 2012.

[60] X. S. Li, C. W. Magnuson, A. Venugopal, R. M. Tromp, J. B. Hannon, E. M. Vogel, L. Colombo, and R. S. Ruoff. Large-area graphene single crystals grown by low-pressure chemical vapor deposition of methane on copper. *Journal of the American Chemical Society*, 133(9):2816–2819, 2011.

[61] Miao Liu, Jianren Sun, Ying Sun, Christopher Bock, and Quanfang Chen. Thickness-dependent mechanical properties of polydimethylsiloxane membranes. *Journal of Micromechanics and Microengineering*, 19(3):035028, 2009.

[62] K.F. Mak, C. Lee, J. Hone, J. Shan, and T.F. Heinz. Atomically thin MoS_2: A new direct-gap semiconductor. *Phys. Rev. Lett.*, 105:136805, Sep 2010.

[63] C. A. Marianetti and H. G. Yevick. Failure mechanisms of graphene under tension. *Phys. Rev. Lett.*, 105:245502, Dec 2010.

[64] Alvaro Mata, Aaron J Fleischman, and Shuvo Roy. Characterization of polydimethylsiloxane (pdms) properties for biomedical micro/nanosystems. *Biomedical microdevices*, 7(4):281–293, 2005.

[65] M A Meyers, A Mishra, and D J Benson. Mechanical properties of nanocrystalline materials. *Progress in Materials Science*, 51(4):427–556, 2006.

[66] M.A. Meyers and K.K. Chawla. *Mechanical Behavior of Materials*. Cambridge University Press, 2009.

[67] Edmund J Mills. On electrostriction. *Proceedings of the Royal Society of London*, 26(179-184):504–512, 1877.

[68] A. Molina-Sánchez and L. Wirtz. Phonons in single-layer and few-layer MoS$_2$ and WS$_2$. *Phys. Rev. B*, 84:155413, Oct 2011.

[69] P. Nemes-Incze, K. J. Yoo, L. Tapaszto, G. Dobrik, J. Labar, Z. E. Horvath, C. Hwang, and L. P. Biro. Revealing the grain structure of graphene grown by chemical vapor deposition. *Applied Physics Letters*, 99(2):023104, 2011.

[70] C. Neto and K. Novoselov. Two-dimensional crystals: Beyond graphene. *Materials Express*, pages 10–17, 2011.

[71] K. S. Novoselov, A. K. Geim, S. V. Morozov, D. Jiang, Y. Zhang, S. V. Dubonos, I. V. Grigorieva, and A. A. Firsov. Electric field effect in atomically thin carbon films. *Science*, 306(5696):666–669, 2004.

[72] K. S. Novoselov, D. Jiang, F. Schedin, T.J. Booth, V.V. Khotkevich, S.V. Morozov, and A.K. Geim. Two-dimensional atomic crystals. *Proceedings of the National Academy of Sciences of the United States of America*, 102(30):10451–10453, 2005.

[73] J. F. Nye. *Physical properties of crystals: their representation by tensors and matrices*. Oxford science publications. Clarendon Press, 1985.

[74] W C Oliver and G M Pharr. Improved technique for determining hardness and elastic modulus using load and displacement sensing indentation experiments. *Journal of materials research*, 7(6):1564–1583, 1992.

[75] Warren C Oliver and Georges M Pharr. Measurement of hardness and elastic modulus by instrumented indentation: Advances in understanding and refinements to methodology. *Journal of materials research*, 19(01):3–20, 2004.

[76] E. Orowan. Fracture and strength of solids. *Rep. Prog. Phys.*, 12(185), 1949.

[77] EJ Pavlina and CJ Van Tyne. Correlation of yield strength and tensile strength with hardness for steels. *Journal of materials engineering and performance*, 17(6):888–893, 2008.

[78] R. Peierls. Quelques propriétés typiques des corps solides. *Ann. Inst. Henri Poincaré*, 1935.

[79] B Peng, M Locascio, P Zapol, S Li, S L Mielke, G C Schatz, and H D Espinosa. Measurements of near-ultimate strength for multiwalled carbon nanotubes and irradiation-induced crosslinking improvements. *Nature nanotechnology*, 3(10):626–631, 2008.

[80] J. P. Perdew, K. Burke, and M. Ernzerhof. Generalized gradient approximation made simple. *Phys. Rev. Lett.*, 77:3865, 1996.

[81] J. P. Perdew, K. Burke, and M. Ernzerhof. Erratum: Generalized gradient approximation made simple. *Phys. Rev. Lett.*, 78:1396, 1997.

[82] J. P. Perdew and A. Zunger. Self-interaction correction to density-functional approximations for many-electron systems. *Phys. Rev. B*, 23:5048, 1981.

[83] Nicholas Petrone, Inanc Meric, James Hone, and Kenneth L Shepard. Graphene field-effect transistors with gigahertz-frequency power gain on flexible substrates. *Nano letters*, 13(1):121–125, 2012.

[84] M. Poot and H. S. J. van der Zant. Nanomechanical properties of few-layer graphene membranes. *Applied Physics Letters*, 92(6):063111, 2008.

[85] B. Radisavljevic, A. Radenovic, J. Brivio, V. Giacometti, and A. Kis. Single-layer mos2 transistors. *Nature Nanotechnology*, 6(3):147–150, 2011.

[86] Q. M. Ramasse, R. Zan, U. Bangert, D. W. Boukhvalov, Y. W. Son, and K. S. Novoselov. Direct experimental evidence of metal-mediated etching of suspended graphene. *Acs Nano*, 6(5):4063–4071, 2012.

[87] Alessia Romeo, Qihan Liu, Zhigang Suo, and Stéphanie P. Lacour. Elastomeric substrates with embedded stiff platforms for stretchable electronics. *Applied Physics Letters*, 102(13):131904, 2013.

[88] C. S. Ruiz-Vargas, H. L. L. Zhuang, P. Y. Huang, A. M. van der Zande, S. Garg, P. L. McEuen, D. A. Muller, R. G. Hennig, and J. Park. Softened elastic response and unzipping in chemical vapor deposition graphene membranes. *Nano Letters*, 11(6):2259–2263, 2011.

[89] Matthew T Russell, Liam SC Pingree, Mark C Hersam, and Tobin J Marks. Microscale features and surface chemical functionality patterned by electron beam lithography: A novel route to poly (dimethylsiloxane)(pdms) stamp fabrication. *Langmuir*, 22(15):6712–6718, 2006.

[90] Ranjana Saha and William D Nix. Effects of the substrate on the determination of thin film mechanical properties by nanoindentation. *Acta Materialia*, 50(1):23–38, 2002.

[91] A Sanati Nezhad, Mahmood Ghanbari, Carlos G Agudelo, Muthukumaran Packirisamy, Rama B Bhat, and Anja Geitmann. Pdms microcantilever-based flow sensor integration for lab-on-a-chip. 2013.

[92] Claudia Sarmoria and Enrique Vallés. Model for a scission-crosslinking process with both h and y crosslinks. *Polymer*, 45(16):5661–5669, 2004.

[93] Angel J Satti, Noemí A Andreucetti, Jorge A Ressia, Marie F Vallat, Claudia Sarmoria, and Enrique M Vallés. Modelling molecular weight changes induced in polydimethylsiloxane by gamma and electron beam irradiation. *European Polymer Journal*, 44(5):1548–1555, 2008.

[94] L. Scandella, A. Schumacher, N. Kruse, R. Prins, E. Meyer, R. Lüthi, L. Howald, and H.-J. Güntherodt. Tribology of ultra-thin MoS_2 platelets on mica: Studies by scanning force microscopy. *Thin Solid Films*, 240(1-2):101 – 104, 1994.

[95] A. Schumacher, L. Scandella, N. Kruse, and R. Prins. Single-layer MoS_2 on mica: Studies by means of scanning force microscopy. *Surface Science Letters*, 289(1-2):L595 – L598, 1993.

[96] N. Severin, S. Kirstein, I. M. Sokolov, and J. P. Rabe. Rapid trench channeling of graphenes with catalytic silver nanoparticles. *Nano Letters*, 9(1):457–461, 2009.

[97] SIMULIA. Abaqus 6.11 user's manual, 2011.

[98] A. Splendiani, L. Sun, Y. Zhang, T. Li, J. Kim, C.Y. Chim, G. Galli, and F. Wang. Emerging photoluminescence in monolayer MoS_2. *Nano Letters*, 10(4):1271–1275, 2010.

[99] G Stan, S Krylyuk, AV Davydov, I Levin, and RF Cook. Ultimate bending strength of si nanowires. *Nano letters*, 12(5):2599–2604, 2012.

[100] G Gerald Stoney. The tension of metallic films deposited by electrolysis. *Proceedings of the Royal Society of London. Series A, Containing Papers of a Mathematical and Physical Character*, 82(553):172–175, 1909.

[101] Yubing Sun, Liang-Ting Jiang, Ryoji Okada, and Jianping Fu. Uv-modulated substrate rigidity for multiscale study of mechanoresponsive cellular behaviors. *Langmuir*, 28(29):10789–10796, 2012.

[102] John L Tan, Joe Tien, Dana M Pirone, Darren S Gray, Kiran Bhadriraju, and Christopher S Chen. Cells lying on a bed of microneedles: an approach to isolate

mechanical force. *Proceedings of the National Academy of Sciences*, 100(4):1484–1489, 2003.

[103] Abel L Thangawng, Rodney S Ruoff, Melody A Swartz, and Matthew R Glucksberg. An ultra-thin pdms membrane as a bio/micro–nano interface: fabrication and characterization. *Biomedical microdevices*, 9(4):587–595, 2007.

[104] Pu Tian. Molecular dynamics simulations of nanoparticles. *Annu. Rep. Prog. Chem., Sect. C: Phys. Chem.*, 104:142–164, 2008.

[105] M. Tortonese and M. Kirk. Characterization of application-specific probes for SPMs. In T. A. Michalske and M.A. Wendman, editors, *Society of Photo-Optical Instrumentation Engineers (SPIE) Conference Series*, April 1997.

[106] N. Troullier and J. L. Martins. Efficient pseudopotentials for plane-wave calculations. *Phys. Rev. B*, 43:1993–2006, Jan 1991.

[107] A. W. Tsen, L. Brown, M. P. Levendorf, F. Ghahari, P. Y. Huang, R. W. Havener, C. S. Ruiz-Vargas, D. A. Muller, P. Kim, and J. Park. Tailoring electrical transport across grain boundaries in polycrystalline graphene. *Science*, 336(6085):1143–1146, 2012.

[108] Katerina Tsougeni, Angeliki Tserepi, and Evangelos Gogolides. Photosensitive poly (dimethylsiloxane) materials for microfluidic applications. *Microelectronic engineering*, 84(5):1104–1108, 2007.

[109] M R VanLandingham. Review of instrumented indentation. Technical report, DTIC Document, 2003.

[110] J H Warner, E R Margine, M Mukai, A W Robertson, F Giustino, and A I Kirkland. Dislocation-driven deformations in graphene. *Science*, 337(6091):209–212, 2012.

[111] X. Wei, B. Fragneaud, C. A. Marianetti, and J. W. Kysar. Nonlinear elastic behavior of graphene: *Ab initio* calculations to continuum description. *Phys. Rev. B*, 80:205407, Nov 2009.

[112] X. D. Wei, B. Fragneaud, C. A. Marianetti, and J. W. Kysar. Nonlinear elastic behavior of graphene: Ab initio calculations to continuum description. *Physical Review B*, 80(20):205407, 2009.

[113] X. D. Wei and J. W. Kysar. Experimental validation of multiscale modeling of indentation of suspended circular graphene membranes. *International Journal of Solids and Structures*, 49(22):3201–3209, 2012.

[114] Y. Wei, J. Wu, H. Yin, X. Shi, R. Yang, and M. Dresselhaus. The nature of strength enhancement and weakening by pentagon–heptagon defects in graphene. *Nature Materials*, 11:759–763, 2012.

[115] W Weibull. A statistical theory of the strength of materials, ser. *Ingeniörsvetenskapsakademiens Handlingar. Stockholm: Generalstabens Litografiska anstalts förlag*, (151), 1939.

[116] Eehern J Wong. *Modeling and control of rapid cure in polydimethylsiloxane (PDMS) for microfluidic device applications*. PhD thesis, Massachusetts Institute of Technology, 2010.

[117] Bin Wu, Andreas Heidelberg, and John J Boland. Mechanical properties of ultrahigh-strength gold nanowires. *Nature materials*, 4(7):525–529, 2005.

[118] J Wu, ZJ Liu, J Song, Y Huang, K-C Hwang, YW Zhang, and JA Rogers. Stretchability of encapsulated electronics. *Applied Physics Letters*, 99(6):061911–061911, 2011.

[119] Y Xia and G M Whitesides. Soft lithography. *Annual review of materials science*, 28(1):153–184, 1998.

[120] D. Xiao, G. B. Liu, W. Feng, X. Xu, and W. Yao. Coupled spin and valley physics in monolayers of MoS_2 and other group-vi dichalcogenides. *Phys. Rev. Lett.*, 108:196802, May 2012.

[121] Q. K. Yu, L. A. Jauregui, W. Wu, R. Colby, J. F. Tian, Z. H. Su, H. L. Cao, Z. H. Liu, D. Pandey, D. G. Wei, T. F. Chung, P. Peng, N. P. Guisinger, E. A. Stach, J. M. Bao, S. S. Pei, and Y. P. Chen. Control and characterization of individual grains and grain boundaries in graphene grown by chemical vapour deposition. *Nature Materials*, 10(6):443–449, 2011.

[122] R. Zan, U. Bangert, Q. Ramasse, and K. S. Novoselov. Interaction of metals with suspended graphene observed by transmission electron microscopy. *Journal of Physical Chemistry Letters*, 3(7):953–958, 2012.

[123] J. F. Zhang, J. J. Zhao, and J. P. Lu. Intrinsic strength and failure behaviors of graphene grain boundaries. *Acs Nano*, 6(3):2704–2711, 2012.

Appendix I: Agilent G200 2D material Nanoindentation Standard Operating Procedure

1. Mount sample on aluminum nanovision puck using Crystalbond.

2. Ensure red-flagged pins are in XP shaft.

   NOTE: If pins are not in place, the XP tip will be exposed after the next step. THIS IS NOT GOOD. This can cause damage to the XP head, tip, etc. REMEMBER TO PLACE FLAGS.

3. Open Nanosuite and click the red "XP" in the lower-right corner of the program window. A message will ask if you want to change the workspace. Click "Yes". Close Nanosuite.
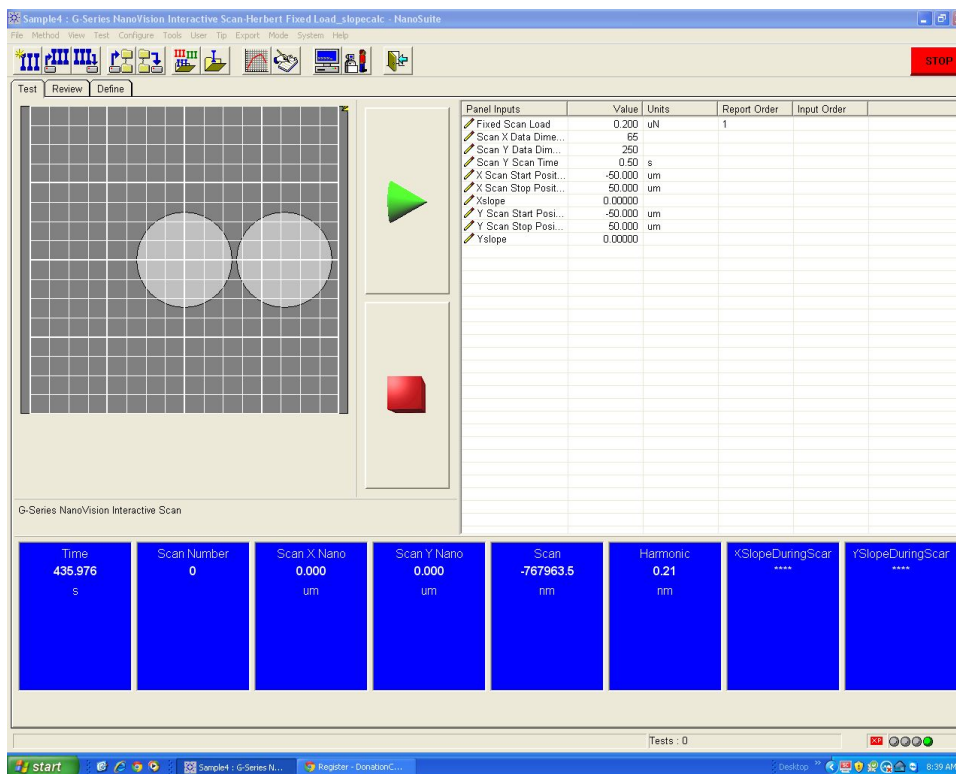

Figure 6.1: Location of workspace switcher.

4. Wait 10-30 s before reopening Nanosuite. *Prematurely opening program can cause driver and miscommunication errors.*

5. Open method "G-Series Nanovision Interactive Scan-Herbert Fixed Load_slopecalc" in folder "Ryan's methods".

6. Open G200 nanoindenter hood.

7. Replace traditional sample holder with nanovision sample holder.

8. Mount single crystal aluminum standard in one of the sample mounts (with no spring or washer) and mount sample with a spring and washer underneath as seen in Fig 6.2.

    (a) Al sample will be used as reference height.

    (b) Ensure sample of interest is on the same plane or below Al surface as seen in Fig. 6.2
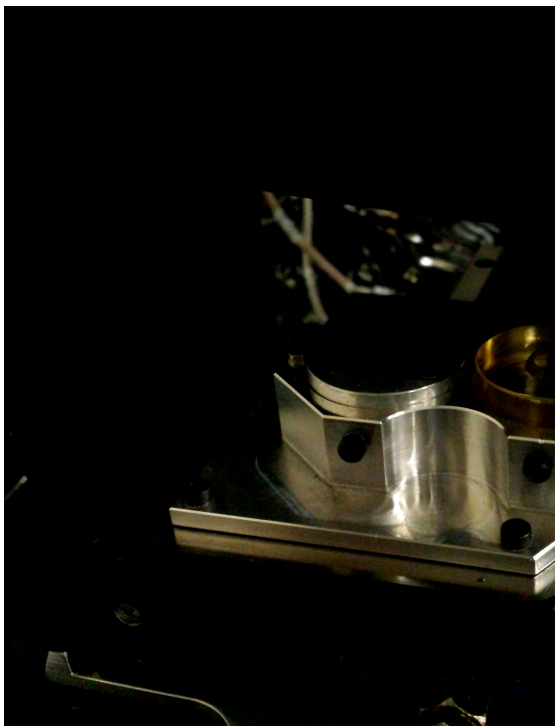
Figure 6.2: Nanovision stage mounted in G200 with sample mounted in left slot and the reference single crystal Al mounted in right slot. The Al surface will be used as reference height and initial microscope-to-indenter calibration. Could also be another metal with 0.9 in total height.

9. Change the objective to the appropriate magnification.

    (a) This operating procedure uses $100\times$.

    NOTE: Use great CAUTION when moving the stage with the $100\times$ magnification. The focal height of the lens is very close to the surface of the sample. DO NOT CRASH THE LENS INTO THE SAMPLE SURFACE while moving the stage.

(b) The other available lenses are 10× and 40×.

10. In Nanosuite, right click the Handset window and change the template to "Nano Positioning Sample Tray".

11. Right click the Handset window again and change the ✓ to "Nano Video Handset".

12. With the blank video screen replacing the tray template, right click again and change the Objective to 100× *or whatever objective is loaded.*

13. Click and hold the "Microscope up Fast" to raise objective away from sample. NOTE: This step ensures the objective will not crash into sample. The absolute height of the objective should be less than 750 μm. ♦♦♦♦ 745.5 um

14. Right click the video handset again and change the ✓ back to "Nano Handset".

15. Left click on the center of the template that has the Al reference sample. The setup in Fig. 6.2 would be the right grey circle.

16. Right click and select "Move to Target".

17. Right click the handset window again and change the ✓ back to "Nano Video Handset".

18. Adjust the focus until the Al surface is in focus as shown in Fig. 6.3. NOTE: This may require moving the sample laterally to have the Al directly under the microscope. This can be done either in the "Nano Handset" menu by selecting an area with left-click and moving to that area with the right-click menu or in the "Nano Video Handset" by click anywhere in the video window. This will bring the clicked point to the center of the field of view. Clicking and holding in this mode will drive the stage continuously in the direction of the mouse *be careful, the stage can move quickly.*

19. The light will also have to be adjusted. This is done by sliding the lightbulb seen in Fig. 6.3. Or by adjusting the manual levers on the nanoindenter itself.
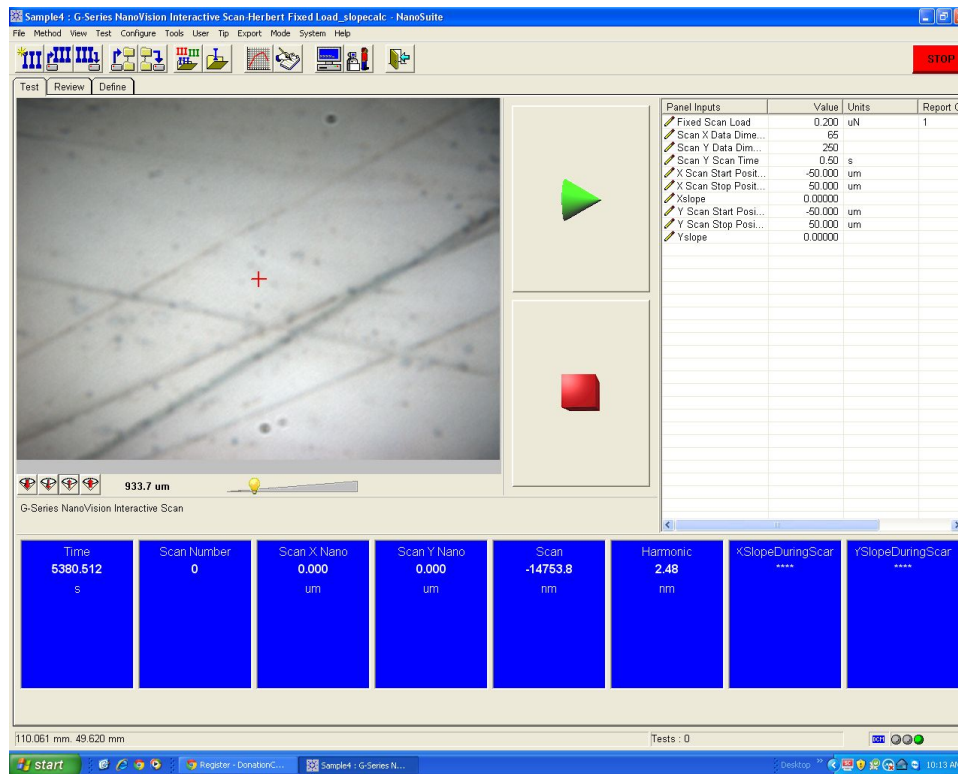
Figure 6.3: Al sample brought into focus.

20. Find an area that does not have many previous indent locations.

21. Perform a microscope to indenter calibration by right-clicking the video screen. Select "Advanced Settings".

    For the 100× objective:

    (a) Change "Number of indents" to 5.

    (b) Change "Distance From Center" to 10 microns.

    (c) Change "Depth into Surface" to 1000 nm.

    (d) Click "Next".

22. After the 5 indents are made, move the red cross-hair to the center of the central indent by click and moving the stage as seen in Fig. 6.4.

    NOTE: If the 5 indents cannot be found by scanning the area, click "Back" and this will center the stage to where the test began. Then click "Finish". This will keep the calibration from getting worse. Then, move 20 μm left and perform another

microscope-to-indenter calibration, this time using "Number of indents"= 3. Now
the pattern should be more recognizeable.

Figure 6.4: Microscope to indenter properly centered before clicking "Finish".

23. Perform another microscope to indenter calibration setting "Number of indents" to
    1 inside the previous indent square.

24. Ensure that indent location does not need further calibration.

25. Right-click on video and bring change ✓ to Nano Handset.

26. Move microscope to sample i.e. the left grey circle.

27. Right-click on video and bring change ✓ to Nano Video Handset.

28. Do not change focus height. Open G200 hood and manually move sample into the
    focal plane as seen in Fig. 6.5. *The sample is spring-loaded, so be careful. Loosen*

the set screw while holding the Al puck and slowly bring it towards the microscope while watching the video feed. Change light as necessary
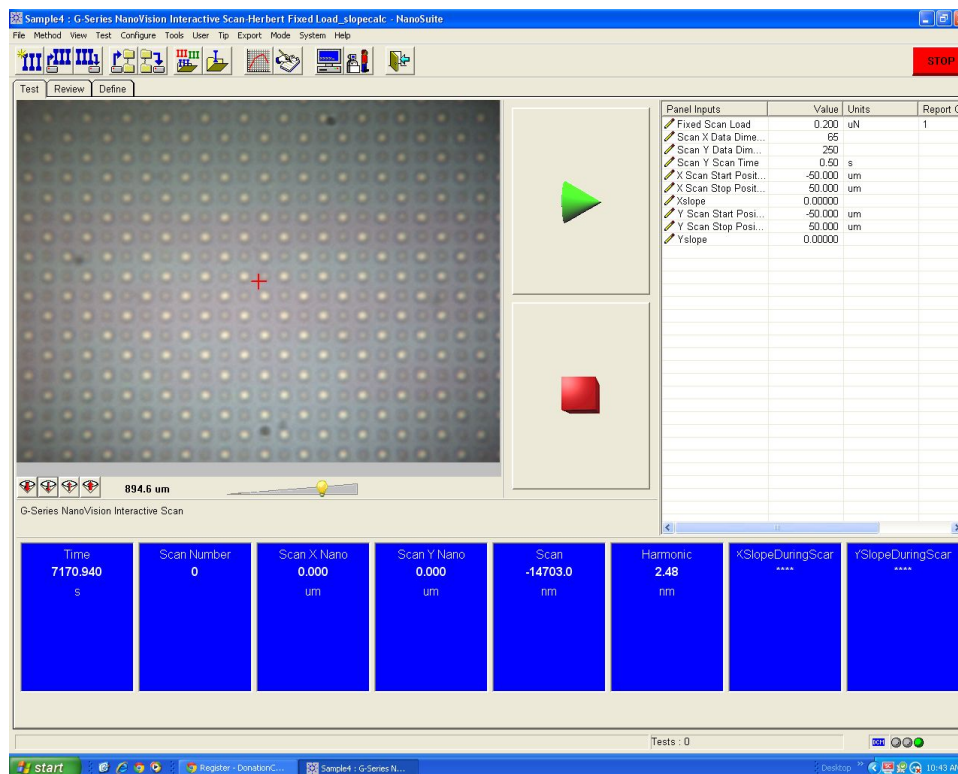

Figure 6.5: Sample surface brought into focus after manually raising sample into focal plain.

29. Move stage to bring 2D crystal into field of view as seen in Fig 6.6. Adjust focus to make 2D crystal as clear as possible.
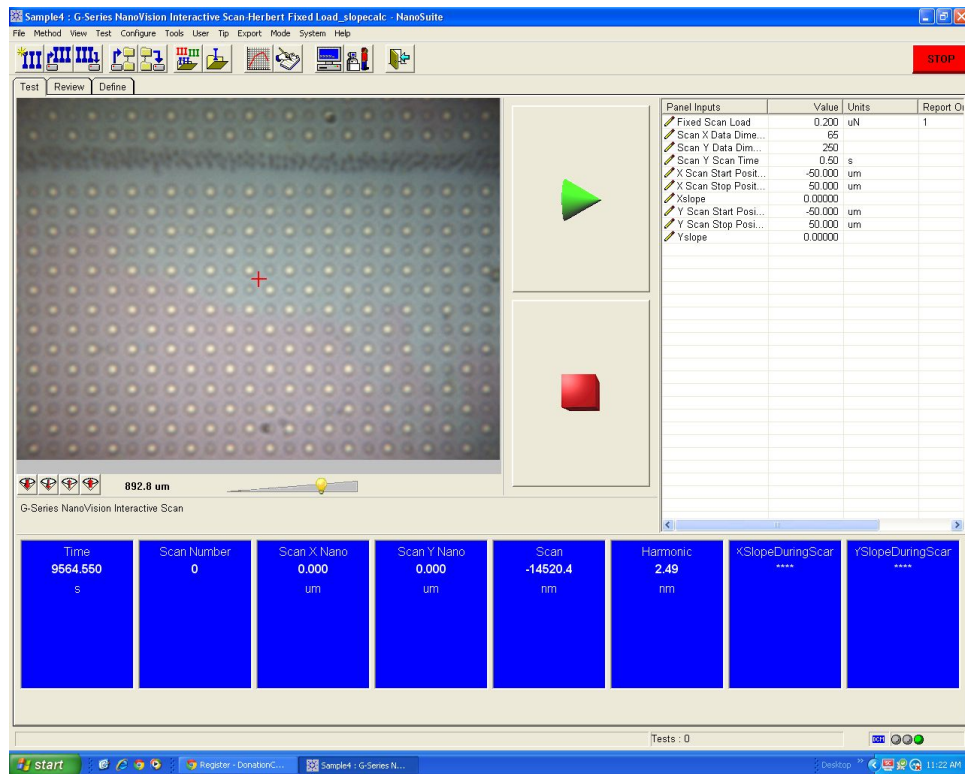
Figure 6.6: Large grain CVD graphenere brought into focus at $100\times$.

30. Right click on video and select "Move Absolute/Relative". Write down "Present Table Position" "X" and "Y" coordinates.

31. Move field of view away from 2D crystal. Preferably to area without etched holes.

32. Redo microscope to indenter calibration following steps 20-24.
    NOTE: DO NOT change focus height throughout the rest of the testing even if indents are out of focus. Changing the focal plane changes the microscope to indenter calibration.

33. Move field of view back to suspended 2D crystal.
    NOTE: "Move Absolute/Relative" has a bug that keeps it from controlling the stage. Just use the 'X' and 'Y' values to help navigate.

34. Center the red crosshair between the etched holes as seen in Fig. 6.6. Make sure that an area is in the field of view that is not sensitive to scratching i.e. silicon dioxide without graphene.

35. Right click on the video image and change the ✓ to "Scanning

36. Click the green down arrow "Move under probe and engage". Handset". A message appears "NO IMAGE CURRENTLY AVAILABLE".

37. Now an image is present of the last microscope image. This is not a live image. Click and drag to create a scanning box on 9-16 holes as seen in Fig. **??**.
NOTE: The holes in this operating procedure are 1 and 1.5 µm diameter. The scanning area just needs to be at least 10 µm×10 µm. Bigger is better for slope calculation.
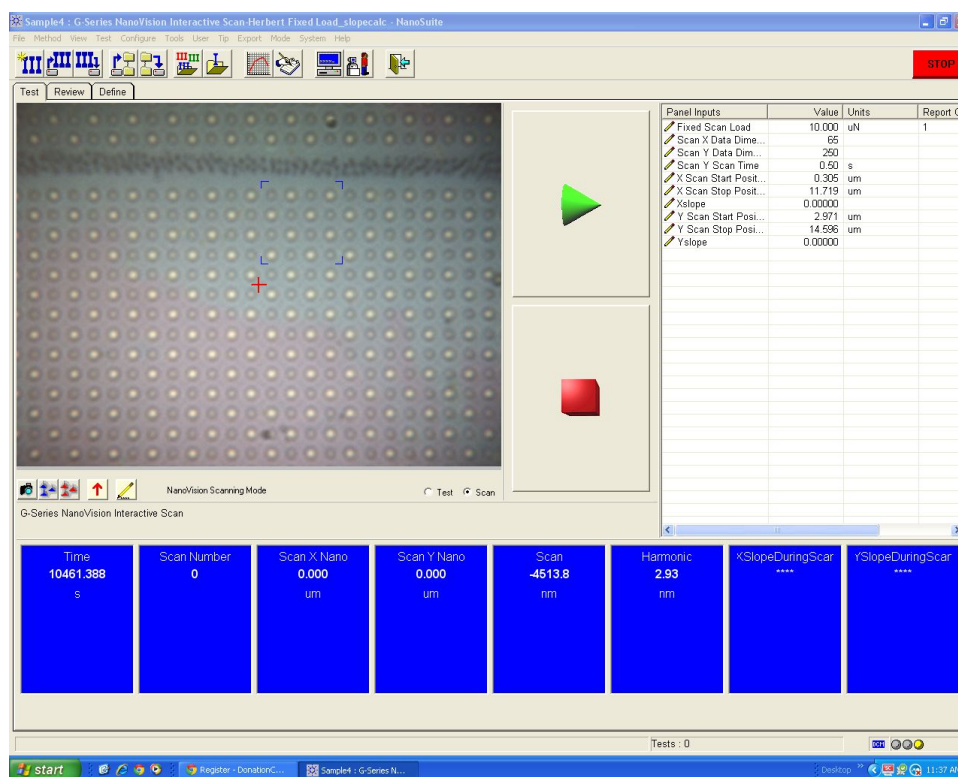

Figure 6.7: Scanning area and scanning parameters properly set for first 10 µN scan.

38. Set the "Fixed Scan Load" to 10 µN.

39. Set the "Xslope" and "Yslope" to 0.00000.

40. Click the Green Triangle to start the scanning.

41. When the test has completed, save the sample in a subfolder labeled 'Scans'.

42. Click the 'Review' tab and look at the 3D image.

43. Change the 'YSlopePosition' value to an x-coordinate that can be used to calculate the Y-slope. In Fig 6.8, this value is taken as 8.37 μm.

NOTE: This value is chosen for a part of the sample that is in a flat plane. You may have to choose an x-coordinate +/- 0.1 μm depending on if it lands on a scan location (there are 65 scan locations by default). image of the scan. Clicking and holding the image shows a crosshair with x,y, and z-coordianate of the measured surface.
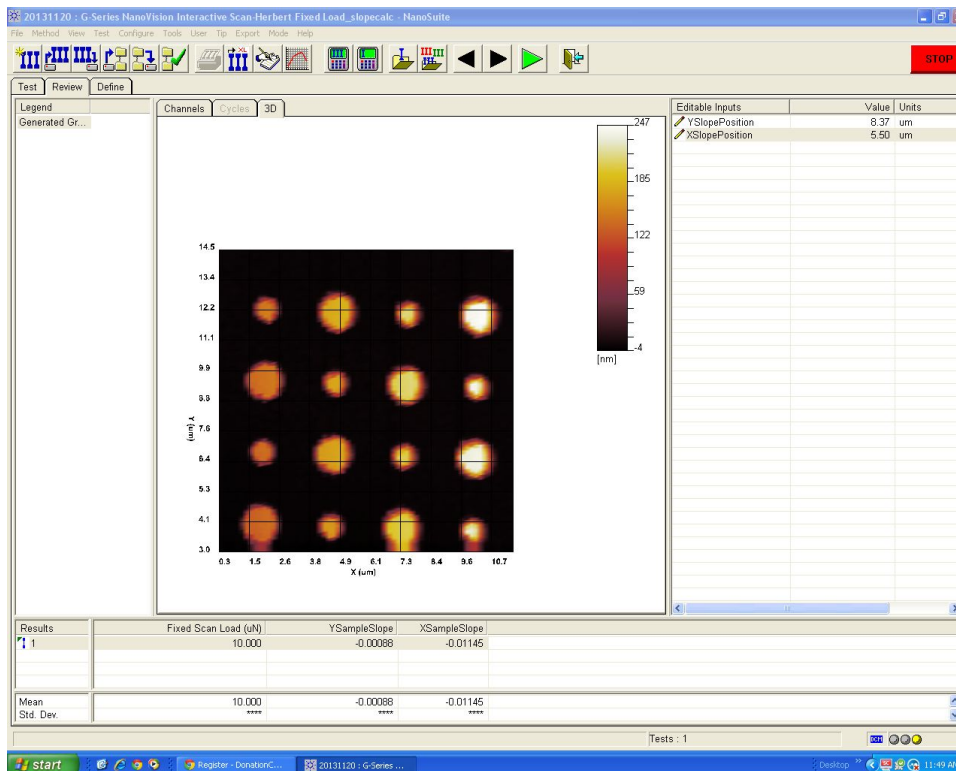
Figure 6.8: Scanned image of surface with 10 μN scanning load. The "YSlopePosition" and "XSlopePosition" have been set properly.

44. Repeat for the "XSlopeposition".

45. Copy the "YSampleSlope" and "XSampleSlope" to the "Test" tab values of "YSlope" and "XSlope". *There is no option to copy and paste, be carefule with +/- signs.*

46. Change "Fixed Scan Load" to 0.2 μN.

47. Click green triangle to begin test.

48. When test has finished go back to "Review" tab and see how much "YSampleSlope" and "XSampleSlope" have changed. Enter the new values again as in Step 45.

49. Go back to the "Test" tab and click the camera button to "Show Video Image".

50. Choose a new scan area that scans some of the previous area and an area that has not been scanned as in Fig. 6.9.
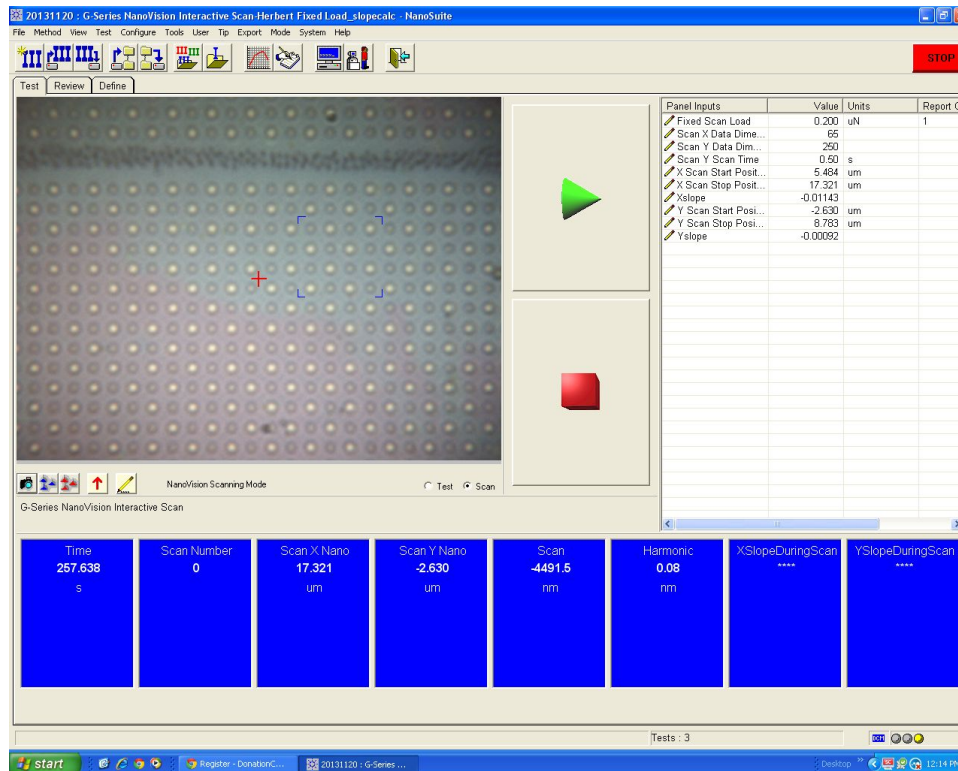
Figure 6.9: New scan area that overlaps first area.

51. Begin test.

52. When test ends, go to review tab. Most likely the surface was damaged from the initial 10 µN scan as seen in Fig. 6.10.
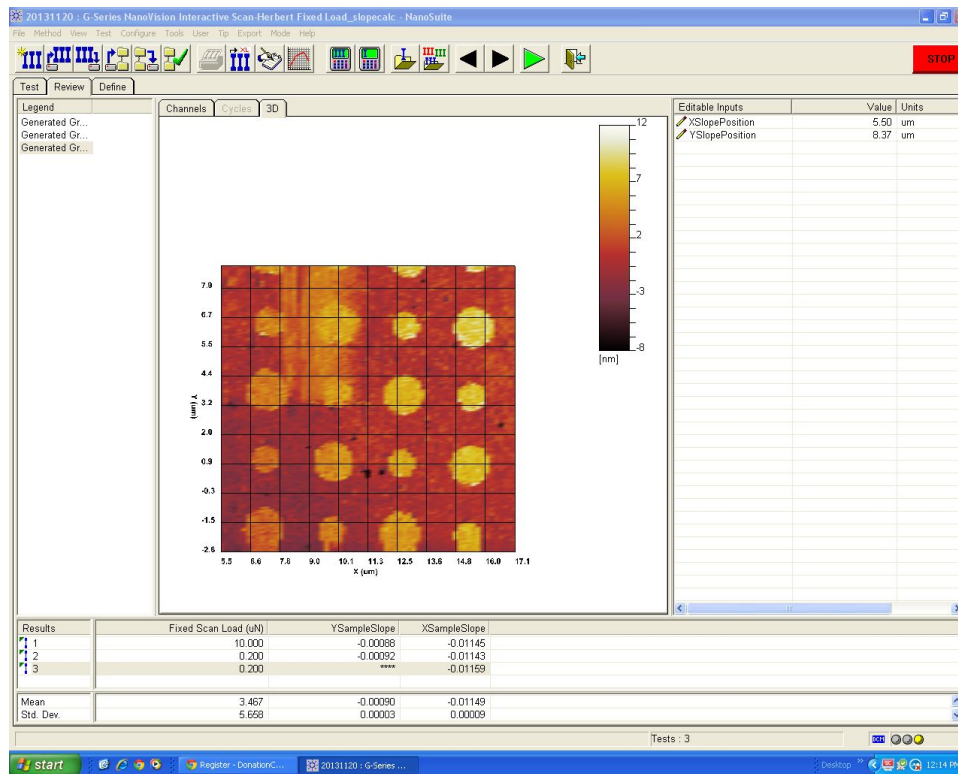
Figure 6.10: New scan area that overlaps first area.

53. Repeat Step 45 for an undamaged section of the substrate.

    NOTE: If slopes are varying more than 0.001, continue to scan areas and update the slope until convergence is achieved.

54. Go back to the "Test" tab and click the camera button to "Show Video Image".

55. Choose a scan area that scans the suspended 2D crystals as seen in Fig. 6.12.
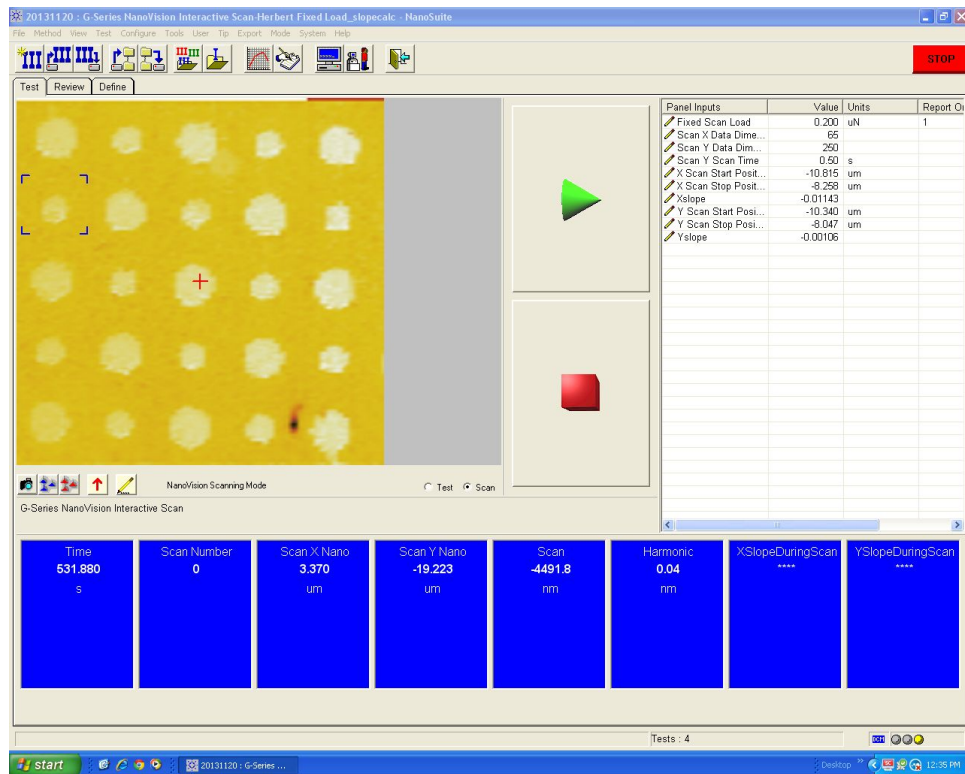
Figure 6.11: New scan area that scans suspended 2D crystals.

56. Begin test.

    NOTE: If the scanning happens to begin–the bottom-left corner is the beginning
    of the scan–in an etched hole, then stop the test immediately. The load will not be
    properly applied and the suspended crystals will be ruined.

57. When test ends, change the scan area to encompass a single hole as seen in Fig. 6.13.
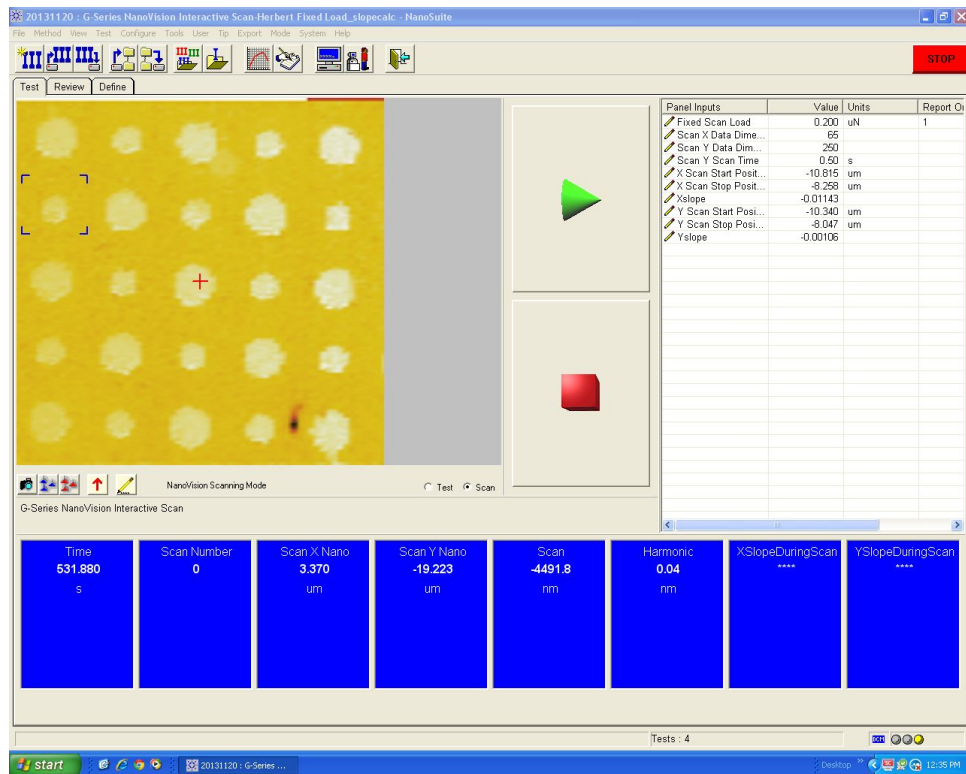
Figure 6.12: New scan area that encompasses one hole.

58. Begin test.

59. When test ends, a single hole should be in the scanning window. Click the radio button "Test" below the image.

60. Load the "V2_DCM-Cycles CSM membrane indentation test_nanovision" method.

61. This will open a new method and a new sample file. The last image in the scanning window is preserved. Click the center of the hole and a blue crosshair appears as seen in Fig. 6.13. This is where the test will occur.
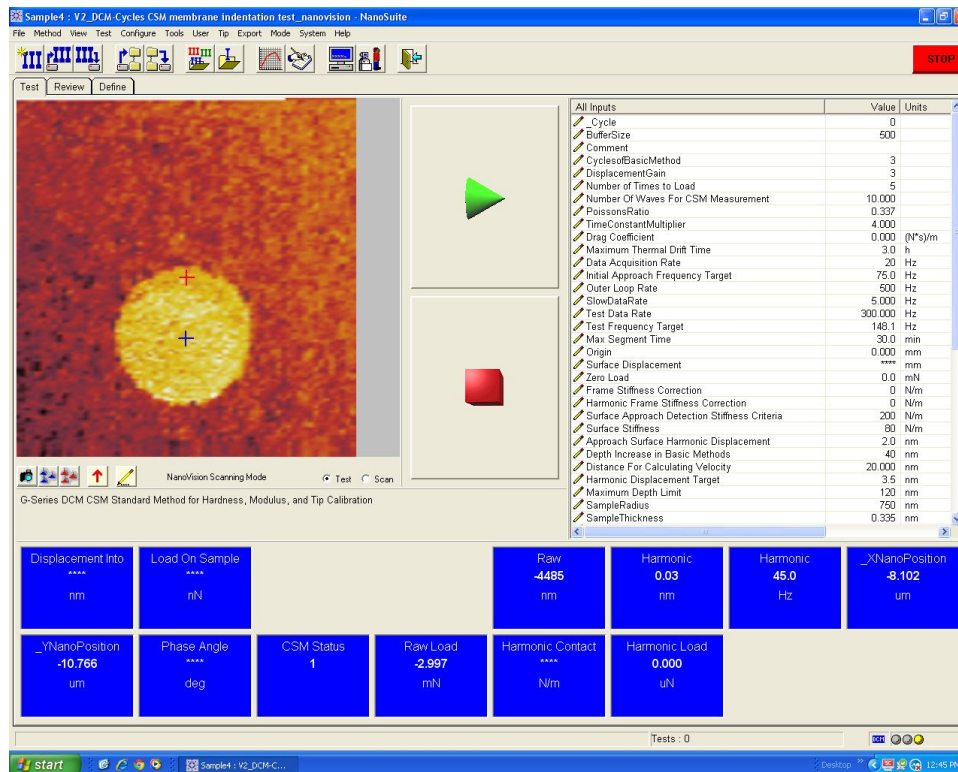
Figure 6.13: "Test" radio button activated and indentation method loaded. After clicking the center, the blue crosshair marks the test location.

62. Right click on the inputs in the right part of the window and move the ✓ to "Panel Inputs".

63. Change the "SampleRadius" to the appropriate value, here it is 500 nm.

64. Change the "Test Frequency" to the Harmonic frequency of the DCM tip.
    NOTE: This value should be recorded in the log book. If it is not, or you have changed the tip since the last time it was recorded. The "_HarmonicFrame" will have to be calibrated. This procedure is laid out in the G200 manual.

65. Leave "CyclesofBasicMethod" as 3, "Number of Times to Load" as 5, "Maximum Depth Limit" as 120 nm, and "Depth Increase in Basic Methods" as 40 nm.
    NOTE: These settings make sure there are 2 CSM-enabled tests that move 30 nm and 60 nm past the initial point of contact and three basic tests that move 120 nm, 160 nm, 200 nm past the initial contact point. These settings can be varied for other geometries that require deeper or shallower indents for larger or smaller diameters,

respectively.

66. Change "Y Distance for Surface Find" to 800 nm and leave "X Distance for Surface Find" as 0 nm.

67. Leave "CSM Test Loading Rate" and "Test Loading Rate" at 5 and 15 µN/s. *These values determine how fast test is run. 15 µN/s is the upper limit for good data collection.*

68. If the time between scanning and indenting is more than 2 min, return to the scanning method and repeat the scan of the hole. This will correct for any thermal drift that occurs over time.

69. With blue crosshair centered and parameters set, press green triangle to begin test.

70. When test has completed, click the "Review" tab and then click the "Channels" tab.

71. Right click on graph and change "Y-Axis Channel" to "Slope Corrected Load on Sample (nN)"

72. Right click on again on graph and change "X-Axis Channel" to "Displacement into Surface (nm)"

73. If the test yeilds no results as seen in Fig. 6.14, then scan another hole and try indenting again. When the test results look like Fig. 6.15, continue onto next step for data analysis.
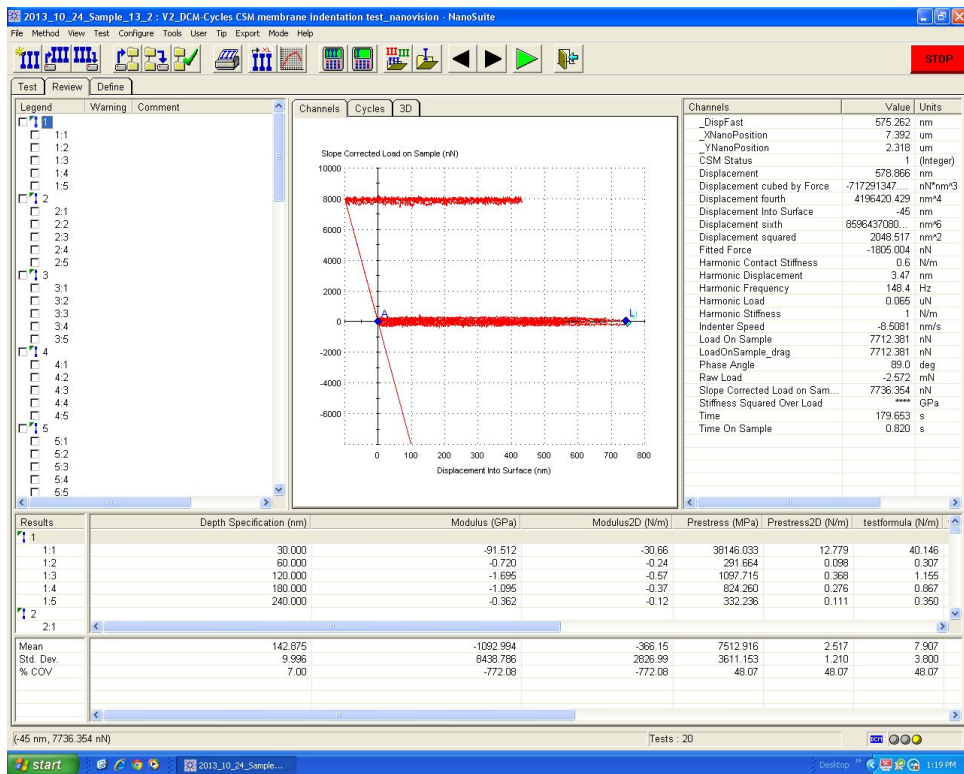
Figure 6.14: Test results that yield no data. The hole is empty.
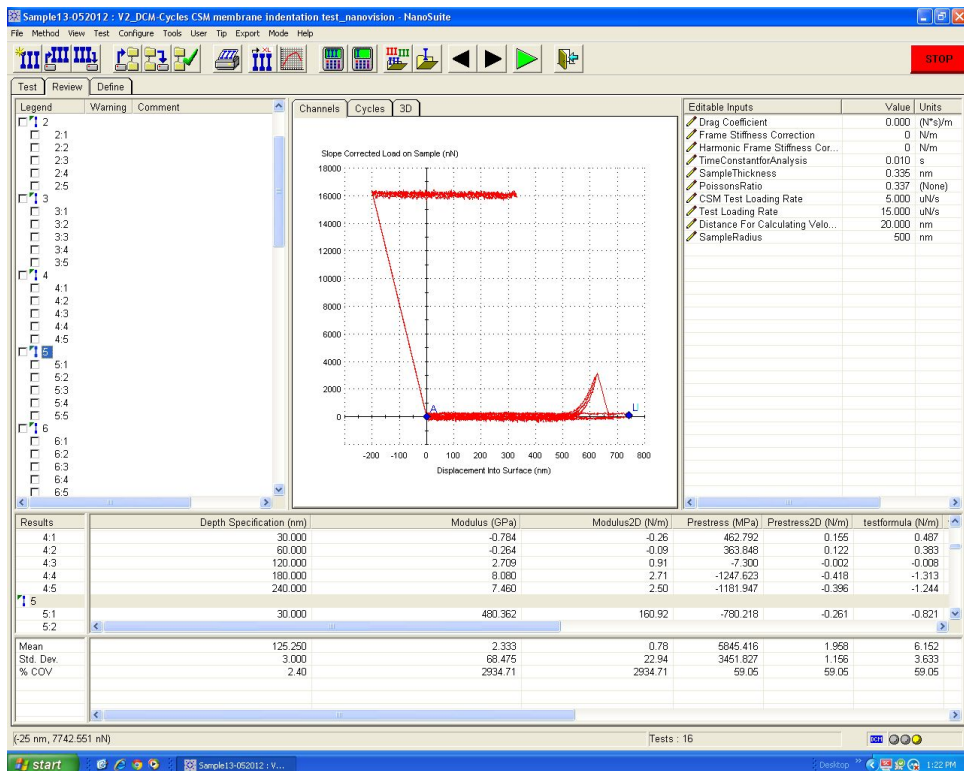
Figure 6.15: Test results that yield data. The hole is covered by a crystal.

74. Right click on graph and change "Y-Axis Channel" to "Phase Angle (deg)"

75. Right click on graph and change "X-Axis Channel" to "Time (s)"

76. Highlight test 1:2.

77. The phase angle is 90 degrees until contact is made with the membrane, then a dramatic change is registered, as seen in Fig. 6.16. Zoom in on the portion of the graph with a stable phase angle and the drop as seen in Fig. 6.17.
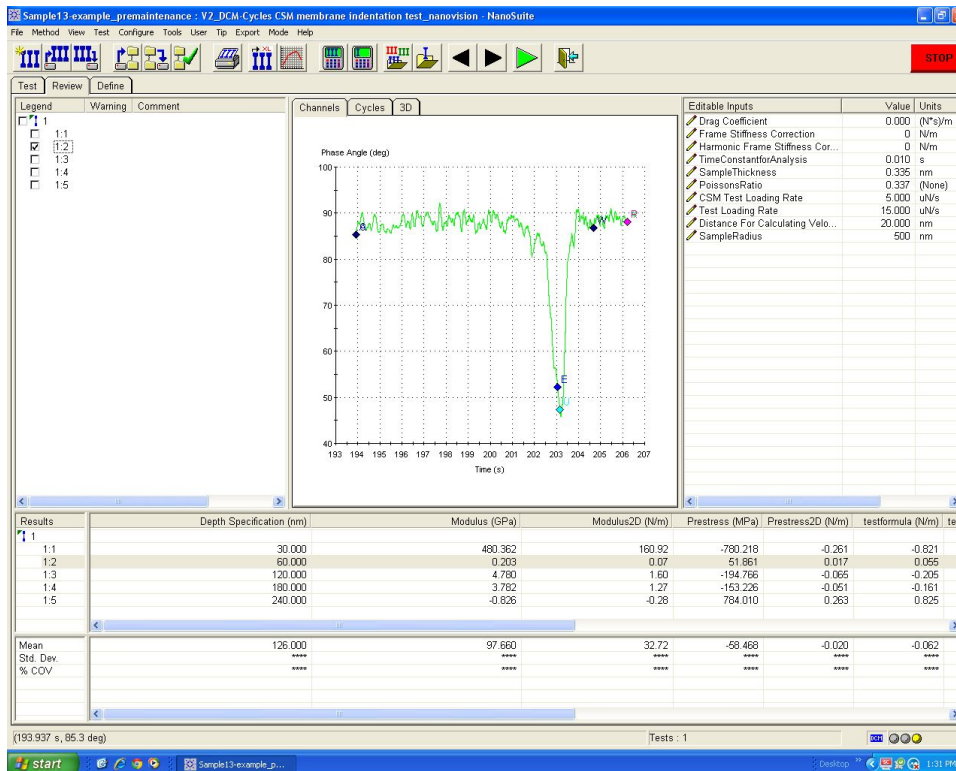
Figure 6.16: Phase angle measured by CSM when contact is made.
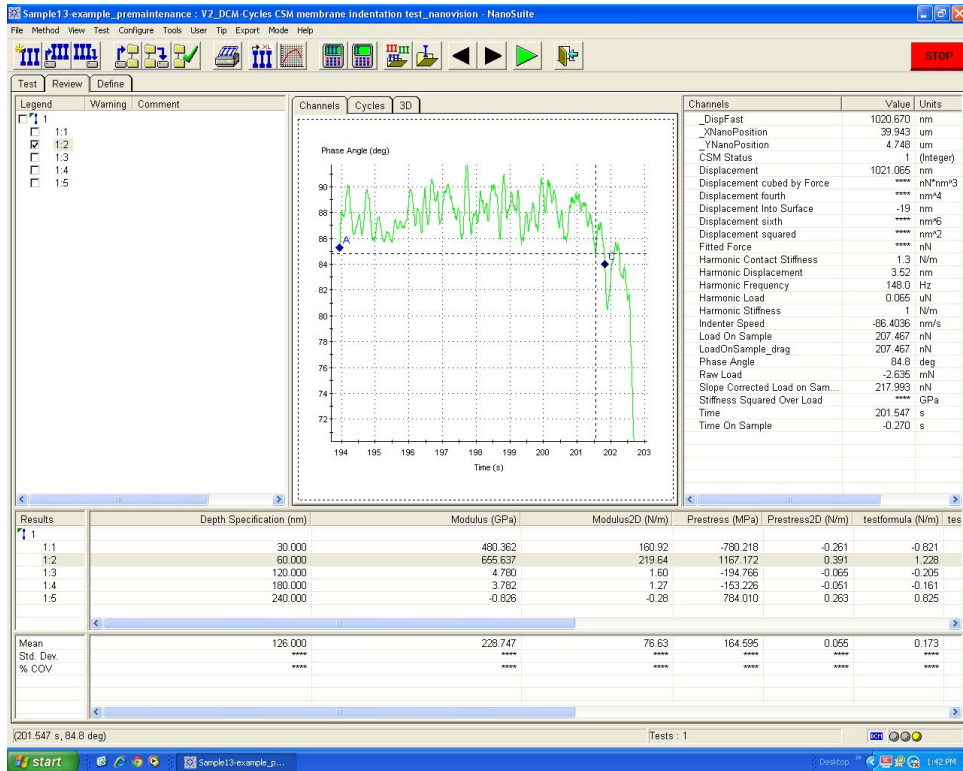
Figure 6.17: Contact point chosen based on drop in phase angle. Indicated by the diamond labeled "C".

78. Move the crosshairs to a point below the noise floor of the phase angle and press "c" on the keyboard. The diamond marker that indicates point of contact will be moved to the current crosshair location.

79. Right click on the right panel and select "Raw Channel Data". This panel now shows the data points for all data channels where the crosshair is located.

80. Zoom in on the point of contact "C" as seen in Fig. 6.18.

81. Make note of the value of "Displacement". In Fig. 6.18 it is 1040.42 nm. The contact point is only accurate to within 2.5 nm with the default settings.
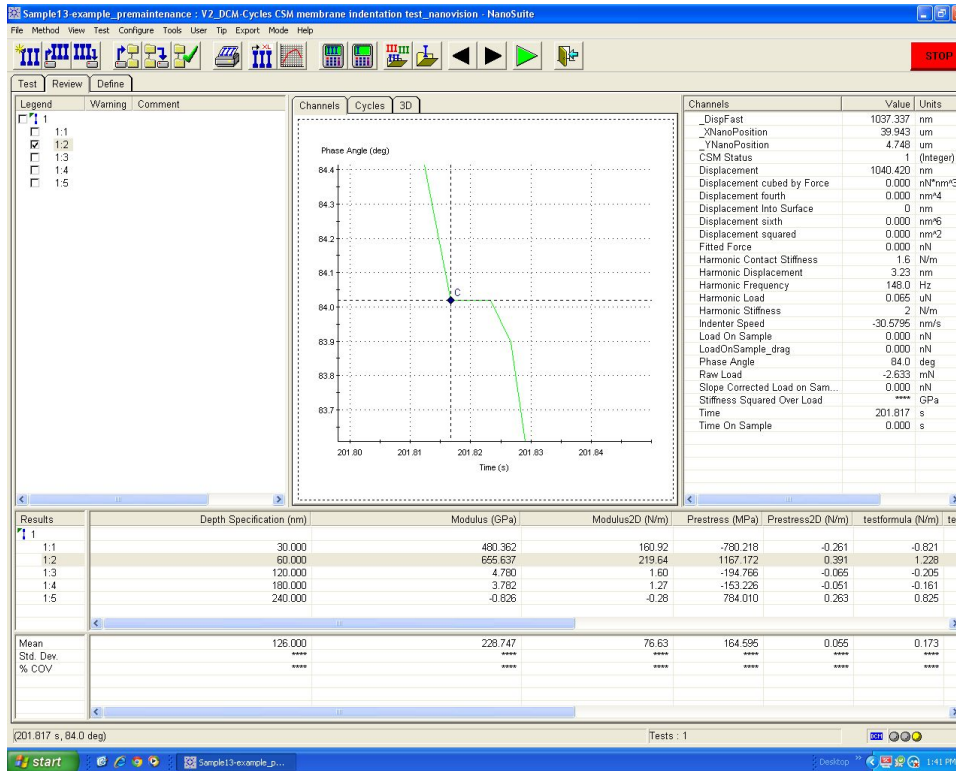
Figure 6.18: Contact point labeled "C". Channel data located to right gives raw displacement value of 1040.42 nm as point of contact.

82. Right click on graph and change "Y-Axis Channel" back to "Slope Corrected Load on Sample (nN)"

83. Highlight test 1:3.

84. Move the crosshairs until the "Displacement" channel reads ≈1040 nm and press "c" on the keyboard again.

85. Repeat for tests 1:4 and 1:5.

86. Check the boxes next to 1:3-5, and change the "X-Axis Channel" to "Displacement into Surface".

87. The resulting graphs should resemble Fig. 6.19.
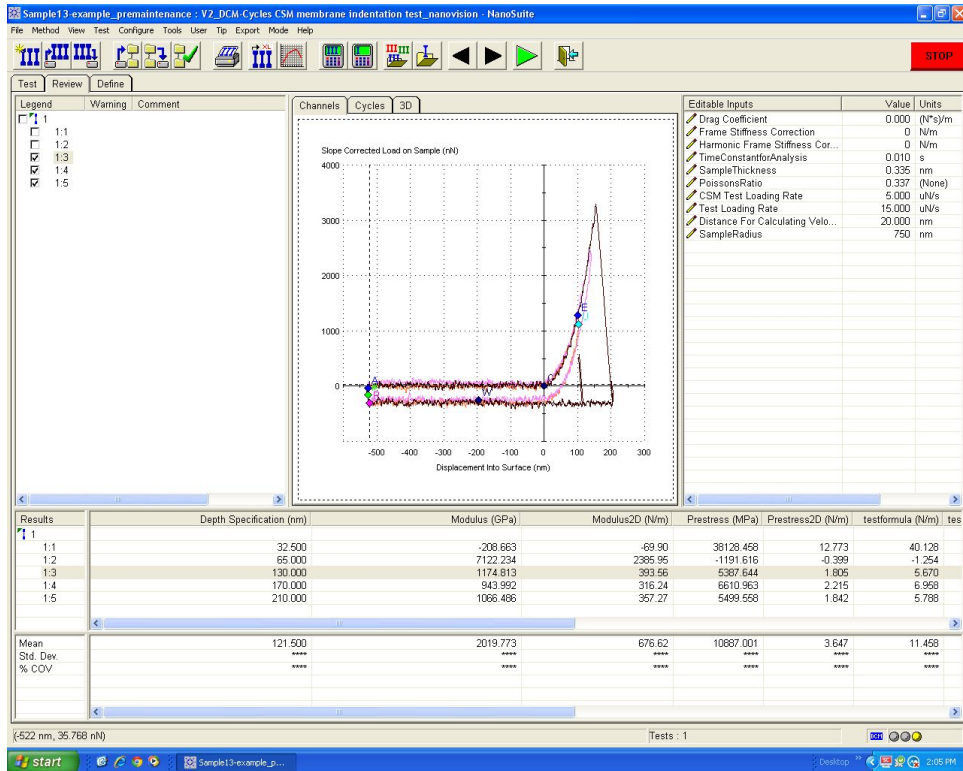
Figure 6.19: Contact points for tests 1:3-5 determined and force-vs-displacement results shown. In the results below the graph, the Modulus is calculated in 2D and 3D values (normalizing by the "SampleThickness" Input) and the prestress is calculated in 2D and 3D.

88. If the test does not measure a breaking point, as in the case of 1:3-4, then the modulus should be accurate. If the membrane fractures during the test, the end of the curve fit should be moved before fracture occurs. This is done by moving the crosshairs and pressing "e" on the keyboard to indicate the end of the curve fit. NOTE: The curve-fitting is done by a least-squares curve-fit to the function

$$F = \sigma_0^{2D}\left(\pi a\right)\left(\frac{\delta}{a}\right) + E^{2D}\left(q^3 a\right)\left(\frac{\delta}{a}\right)^3$$

where a is sample radius, E^{2D} is the 2D modulus, σ_0^{2D} is the 2D prestress, q is a function of Poisson ratio, F is applied force, and δ is the displacement of the center of the membrane.

If the value of a is incorrect i.e. "SampleRadius", then the 2D modulus will be incorrect. If the "SampleThickness" is incorrect, then the value of 3D modulus and 3D prestress will be incorrect.

89. Change the value of "Drag Coefficient" to 0.8 Ns/m. The nanoindenter has inherent

drag due to a number of factors. When the "Drag Coefficient" is updated, the force values compentsate for the inherent drag. This will not affect results much, but it shows there is no hysteresis in the loading-unloading until fracture occurs, as seen in Fig. 6.20.

NOTE: The value of 0.8 Ns/m was calculated by indenting into empty holes at different indenter speeds. I took at least 3-5 data points per speed. Then, I integrated the total area between the curves and determined what drag coefficient would lead to that amount of energy loss. Taking the average, I came up with the current figure for drag in the system. In the future, it may be necessary to recalibrate this figure, but it has been constant through multiple tip changes thus far.
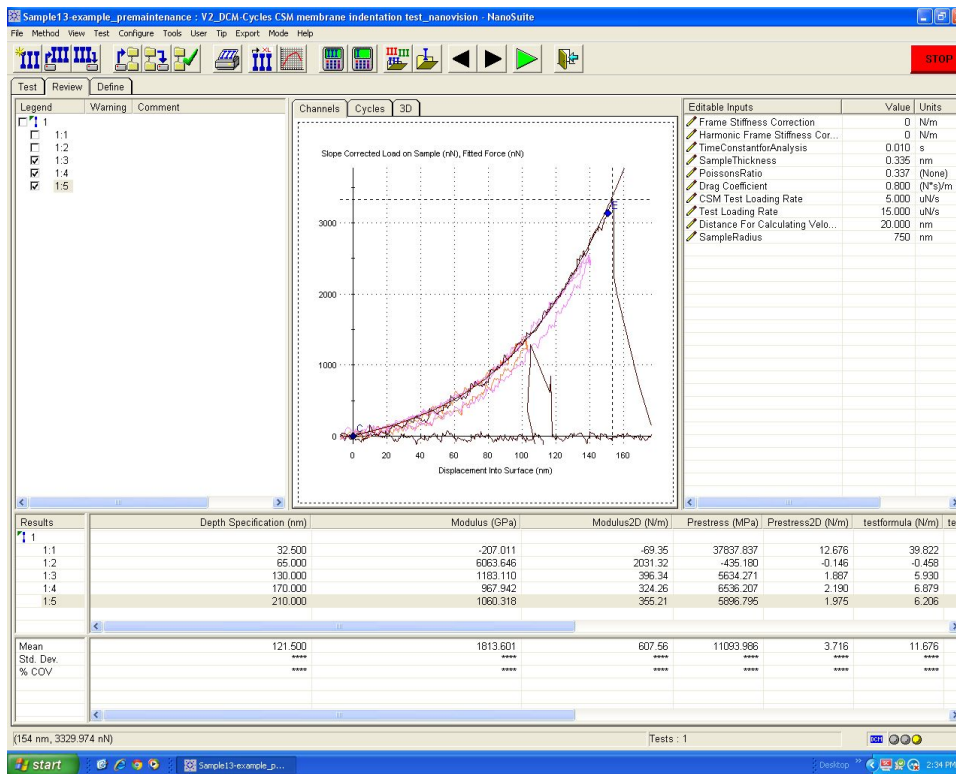
Figure 6.20: Graph demonstrating little to no hysteresis after "Drag Coefficient" is updated and the fitted force plotted.

90. Highlight test 1:5.

91. Move the cursor to the maximum load measured, in the bottom left corner is the value 3329.974 nN as seen in Fig. 6.20. This is the value of "Breaking Force".

92. To plot two values of force on the same graph (in this case the fitted force and the

measured force), right click on the graph and select "Properties".

93. Check the box on the left "Multiple Channels".

94. Click "Select...".

95. Highlight "Fitted Force" and Click "Add".

96. Click "OK", then "OK" again.

97. Now three curves appear, zoom in and ensure that they describe the data well as seen in Fig. 6.20.

98. Record the values of Modulus, prestress, and breaking force.

99. Repeat scanning and indenting procedure until data is statistically significant. NO-TE: In the scanning method, the picture shown in the scanning window on the "Test" tab can be changed to another image. Go to the "Review" tab select the "3D" tab. Then, select the "Generated Graph" of interest. Select the "Test" tab again and the scanning window will be updated.

100. When testing is complete, click the red up arrow to "Disengage Tip".

101. Right click on the scanning window and move the ✓ to "Nano Handset".

102. Right click the nanohandset window and select "Initialize".

103. Open the G200 hood and replace the traditional positioning tray.

104. Change the workspace back to XP by clicking the small blue icon in the bottom-right of the Nanosuite window.

105. Restart the Nanosuite software and the nanoindenter is ready for the next user.

106. Place the Nanovision stage on the shelf below the main nanoindenter hood.

107. Replace the objective with the 10× objective.

108. Close hood of the nanoindenter.

Final words of advice:

- Keep the number of tests in each sample file under 20. The more tests in a sample file the higher the risk for crashing the software *and losing data.*

- Thermal drift is always a hurdle. One of the best ways to get close to thermal equilibrium is to set up the sample and leave it alone for 3-5 hours. Testing can be run remotely through a desktop sharing program.

- This method was validated using exfoliated graphene. If the method is not working properly, you should be able to run experiments on graphene and get the same results as C. Lee *et al.* 2008 and G. Lee *et al.* 2013.

- It is possible to indent into the silicon dioxide with the edges of the tip. This results in almost a step response of force. It is not super-strong graphene.

- This test was designed to use a cube corner tip with a known radius. The experimental results will not be affected by unknown tip radii or other tip geometries, but the post-processing of the data is dependent upon knowing the radius at the very end of the tip that contacts the membrane.

- This method does not give the user an idea if the hole is well covered or even covered at all, until indentation is performed. One way to work around this is to use SEM or AFM to first examine the quality of the crystal and carefully document where prime candidates for testing are located.

Appendix II: XE-100 Nanoindentation Standard Operating Procedure

AFM Standard Operating Procedure for imaging:

by Ryan Cooper

1. Open AFM door

2. Unclamp scanner head and unplug

3. Using one hand, slide scanner head to right to remove from AFM

4. Use AFM tweezers to pick up cantilever mounted on holder to gently attach cantilever to scanner head

    (a) **Important:** To avoid losing tip from magnet's pull, bring the cantilever holder in at a $45^{\underline{o}}$ angle to its resting place. Also, hold cantilever holder by corner and avoid blocking either of the holes

5. Turn on light bank

6. Turn on the three AFM programs:

    (a) XEP (positioning software to control AFM)

    (b) XEI (image software for analysis)

    (c) XEC (camera software to see optical microscope image)

7. Click on "Part Select"

(a) Turn on NC-AFM for non-contact mode

(b) Turn XY Voltage to high

(c) Turn Z Voltage to high

(d) Turn XY to 100 μm

(e) Turn Z-scanner to 20 nm

8. Turn on laser and click OK to frequency sweep

9. Use dials to move laser onto center of cantilever

10. Once laser is positioned in center of cantilever, adjust mirrors to maximize 'A+B' and minimize 'A-B' and 'C-D'

(a) A+B ≈ 2

(b) A-B < 0.7

(c) C-D < 0.7

11. In the Scan Control Box, click "NCM setup"

(a) The peak corresponds to the resonance frequency

(b) Adjust the "Drive %" until $^1/_4$ of the peak is approximately 0.25 μm and use this as the set point by placing the red bar there

(c) Note: If the peak is very wide, the tip may not be good anymore

12. With "Focus Follow" checked, approach stage until substrate can almost be seen

13. Uncheck "Focus Follow" and focus on substrate

14. Using control knobs, move substrate to desired position

15. Close AFM door and place latch on without tightening down

16. Move the focal point up 100 μm from substrate

17. Move AFM cantilever down until in focus (Now cantilever is 100 μm from substrate)

18. Check "Focus Follow"

19. Ensure approach is at the appropriate setting, if unsure use the slow setting

20. Click "Approach"

21. Set "Scan Rate" to ˜0.5 Hz

22. Set "Z-servo gain" to ˜ 1–2

23. Set "Scan Size" to appropriate setting, good to start with 20 μm

24. For imaging, look at Topography, NCM amplitude, and NCM phase in both directions

25. Once image is obtained, analysis can be achieved on the image by right-clicking on the image and selecting export

    (a) Once in the XEI software, image can be flattened, measurements taken, and saved as tiff or information per pixel for matlab or other software analysis

26. After images are taken, click "Lift Z" and raise scanner head to upper ³⁄₄ of diagram on screen

27. Turn off the laser

28. Turn off light bank

29. Unplug and unclamp scanner head

30. Carefully remove AFM tip

31. Remove sample

32. Replace scanner head, clamp and plug in

33. Close AFM door and close latch but do not tighten down

AFM Standard Operating Procedure for indentation:

by Ryan Cooper

1. Open AFM door

2. Unclamp scanner head and unplug

3. Using one hand, slide scanner head to right to remove from AFM

4. Use AFM tweezers to pick up cantilever mounted on holder to gently attach cantilever to scanner head

1. (a) **Important:** To avoid losing tip from magnet's pull, bring the cantilever holder in at a 45$^{\text{o}}$ angle to its resting place. Also, hold cantilever holder by corner and avoid blocking either of the holes

1. Turn on light bank

2. Turn on the three AFM programs:

1. XEP (positioning software to control AFM)

2. XEI (image software for analysis)

3. XEC (camera software to see optical microscope image)

1. Click on "Part Select"

1. Turn on NC-AFM for non-contact mode

2. Turn XY Voltage to high

3. Turn Z Voltage to high

4. Turn XY to 100 μm

5. Turn Z-scanner range to 20nm

6. Cantilever: **Choose Calibrated Cantilever type**

1. Turn on laser and click OK to frequency sweep

2. Use dials to move laser onto center of cantilever

3. Once laser is positioned in center of cantilever, adjust mirrors to maximize 'A+B' and minimize 'A-B' and 'C-D'

1. A+B ≈ 2 (if under 1.2 you will get error message)

2. A-B < 0.7

3. C-D < 0.7

1. In the Scan Control Box, click "NCM setup"

1. The peak corresponds to the resonance frequency

2. Adjust the "Drive %" until $^1/_4$ of the peak is approximately 0.25 μm and use this as the set point by placing the red bar there

3. Note: If the peak is very wide, the tip may not be good anymore

1. With "Focus Follow" checked, approach stage until substrate can almost be seen

2. Uncheck "Focus Follow" and focus on substrate

3. Using control knobs, move substrate to desired position

4. Close AFM door and place latch on without tightening down

5. Move the focal point up 200 μm from substrate

6. Move AFM cantilever down until in focus (Now cantilever is 200 μm from substrate)

7. Check "Focus Follow"

8. Ensure approach is on slow setting (in the tab "Set-up"-> "Approach")

9. Click "Approach"

10. Set "Scan Rate" to ˜0.5 Hz

11. Set "Z-servo gain" to ˜ 1–2

12. Set "Scan Size" to appropriate setting, good to start with 20 µm

13. For imaging, look at Topography, NCM amplitude, and NCM phase in both directions

14. Once image is obtained, raise z-stage by 50 µm

Cantilever Calibration:

1. Open previous calibrated cantilever data such as "Namiki_set3_#2.xml" in "C:/Park Systems/XEP/DB"

2. Change "Cantilever Stiffness" to 40 N/m as initial guess

3. Save as new tip name "_New Name_.xml"

4. open XEP

5. In part select, choose "_New Name_"

6. Perform *Sensitivity Calibration* to determine sensitivity

7. turn on NC mode

8. lift cantilever ˜100 µm off surface

9. move crosshair to end of calibration cantilever

10. scan 5x5 µm images until edge of calibration cantilever is found (**Important:** Stop test **immediately** when edge is found)

11. choose indent location near edge of cantilever

12. use excel to interpolate linear section of Force-displacement data

13. Use the Tortonese and Kirk "Characterization of application specific probes for SPMs" to calculate Cantilever stiffness

14. Lift cantilever

15. Turn on NC mode

16. go to "C:/Park Systems/XEP/DB/"_New Name_.xml" and change cantilever stiffness to new value

17. restart XEP to access calibrated cantilever data

Sensitivity Calibration:

1. Click "F/D Spectroscopy mode" (**Important:** Once clicked, the program switches to contact mode)

2. Change "Set point" to 100 nN

3. Set "min" to 0 μm

4. Set "max" to 0.150 μm

5. Set "Points" to 1024

6. Right click on substrate (or any hard point on surface) and click move here

7. On same spot, right click again and choose "Add point"

8. Click "approach" then tip will be on that point

9. Click "Aquire"

10. Change "min" to -20 nm

11. Z-detector data should not be subject to hysteresis

12. Once data is acquired, lift z-stage 50 μm

13. Click "Mode" –> "Maintenance Mode" –> Password: "cantilever"

14. Click "Mode" –> "Calibrate Mode" –>Click "Cantilever"

15. Use mouse to highlight linear, nonzero, response of Voltage-displacement response

16. Click "Calculate"

17. Click "Calibrate" (A-B sensitivity is typically ˜80)

18. Click "Save Calibration" 2–4 times to ensure data is saved

End of Calibration

Data Acquisition

1. Turn off laser

2. Change to NC-AFM

3. Turn on laser

4. Change resolution to 128 and increase scan rate

5. Image surface and find center of sample

6. Move z-stage up 50 μm

7. Click "F/D Spectroscopy mode"

8. Right click on image and select "Remove all points"

9. Right click on center of sample and choose "move here"

10. Right click on same spot and choose "add point"

11. Ensure approach setting is "slow"

12. Click "Approach"

13. Change "min" to 0 μm

14. Click "Acquire"

15. Increase "min" by -20 μm per run until ready to break sample

16. Save graphs by double-clicking, checking the X-Y data box and clicking "export"

17. To perform more indentations, repeat "Data Acquisition" steps 1–16

End of Data Acquisition

Shut Down

1. After images are taken, click "Lift Z" and raise scanner head to halfway the diagram on screen

2. Turn off the laser

3. Turn off light bank

4. Unplug and unclamp scanner head

5. Carefully remove AFM tip

6. Remove sample

7. Replace scanner head, clamp and plug in

8. Close AFM door and close latch but do not tighten down

Appendix III: Nanoimprint Lithography Standard Operating Procedure

Wafer Fabrication Standard Operating Procedure:

written by Ryan Cooper

E-beam evaporator (evaporating Chrome onto Si wafer)

1. If red light on top of machine is off, press "Manual"

2. Press "Navigator Panel" then "Pumping Control" then "vent PC" to vent process chamber

3. Wait for red light to turn on again on top of device

4. Open the process chamber by pressing "Chamber Power" and "Chamber Up" simultaneously

5. Ensure shutter is blocking sample from e-beam evaporator

6. Load samples in top of process chamber

7. Locate crucible with chrome for deposition

    (a) Note: Up to six crucibles can be used for multi-layered deposition

8. Close the process chamber by pressing "Chamber Power" and "Chamber down" simultaneously

9. Press "calibrate ATM" then "Pump PC" to evacuate the process chamber

    (a) Note: Log the time the PC starts to evacuate and the times when the pressure reaches 8E-2 and 9E-6 (9E-6 is minimum operating pressure)

    (b) Note: Its best to wait until PC pressure reaches 1E-6 to start evaporating

10. Turn chiller power on

11. Press "Navigator Panel" then "Power Control" to make "Power Interface" panel appear

    (a) Note: All Interlock lights on screen should be green

12. Start from bottom turning devices on:

    (a) Contactor- "on"

    (b) 10 seconds later- Press "Reset"

    (c) High Voltage- "on"

    (d) Filament- "on"

13. Press "Sigma" to open the Sigma interface

14. Update the Material/Sensor Setup with the settings for Chromium

15. Press "Zero thickness QCM 1" similarly 2

16. Start loop control

17. Quickly set output set point as 1%, then 1.5%

18. Increase the output set point by 0.5% intervals until desired set point is reached

    (a) Note: Check last user's set point for metal in use

19. Check viewer to see if e-beam is located on metal used for deposition, if not use the Power Supply Controller dials "lat" and "long" on the "pos" row to move the e-beam to desired position

20. When evaporation rate reaches a steady and desirable level, press "Zero Thickness QCM" and then quickly open the source by pressing "Open"

    (a) Note: The evaporation rate changes as the e-beam is shifted in the crucible, be careful when adjusting the e-beam position while depositing on substrate

21. When desired thickness is achieved, close the source by pressing "Close"

22. Decrease e-beam power output by 0.5% intervals until 0% is reached then press "Stop Power"

23. Press "Navigator" then "Power Control" to open the power control panel

24. From the top of the panel turn components off (only the right column buttons):

    (a) Filament- "Off"

    (b) High voltage- "Off"

    (c) Contactor- "Off"

25. Turn chiller off

26. Record final pressure

27. Press "vent PC" to vent the PC

28. Record in the log book the deposition rate, the metal, etc.

29. Press "Chamber Power" and "Chamber Up" simultaneously to raise the chamber

30. Remove the samples from the PC

31. Vacuum and brush clean the PC

32. Press "Chamber Power" and "Chamber Down" simultaneously to close PC

33. Press "calibrate ATM" then "pump PC" to evacuate PC

34. Log out

Spin Coating w/ PMMA (anisole, anhydrous 99.7% 495 PMMA A6)

1. Swipe into spin coater

2. Set hot plate temperature to 180°C

3. Turn on vacuum

4. Blow dry sample

5. Place on vacuum holder

6. Press "Program" then "Edit mode"

   (a) Steps = 1/1

   (b) Time: 00:45.0

   (c) rpm: 3000 rpm

   (d) Acel: 1000

7. Press "V" to vacuum hold sample

8. Drop on PMMA 495kA3

9. Press "start >"

10. After process, place on 180°C hot plate for ~1 min

11. After sample has been on hot plate ~1 min, transfer to sample case

12. Log out of machine

Nanoimprint:

1. Swipe into machine

2. Check gages

   (a) First gage, should be above 600 psi

   (b) Second gage should be about 500 psi

   (c) Wall gage should be >80 psi (turn on)

3. Press "Recipe" then "User set"

   (a) Pumping time: 2 min

   (b) Pre-imprint: 180 $^{\circ}$C and 50 psi

   (c) Imprint: 180°C and 450 psi

   (d) Process time: 3 min

4. Open nanoimprinter door slowly

5. Place down the big membrane first then place smaller membrane on top

6. Place sample on second membrane with master on top

   (a) Note: be sure to offset the master slightly from the sample

7. Check the membrane on the metal ring and make sure magnets are properly placed

8. Ensure smaller membrane is between large membrane and sample and align metal ring in machine

9. Press "Begin" then "OK"

10. When process ends, open SLOWLY and PAY ATTENTION to sample

11. Remove sample from nanoindenter

12. **IMPORTANT:** When separating sample from master be sure **not** to induce any shear stress between the sample and master. Use a razor to separate the sample from the master and then gently flip over to prevent damage to master print.

13. When finished, log out of machine

I.C.P. (Oxford Plasma Lab 80 Plus)

1. Scan in to machine

2. Press "Process" then "Recipe" then "Load" then "OK"

3. Choose "OPT-ICP-Plasmaclean"

4. Click "OPT clean" then "edit step" specify step time: 10 min

5. Click "OK" then click "Run"

   (a) When "Yellow Alert" appears, press "Accept"

6. After cleaning, and machine vented raise the chamber by choosing "Chamber up" and pressing both "Hoist" buttons

7. Load sample

8. Choose "Chamber Down" and lower by pressing both "Hoist" buttons

9. Press "Stop" then "Evacuate"

10. When using Oxygen, do not enter wafer name

11. Press "Process" then "Recipes" then "Load" and choose "Changgu-02NOICP"

    (a) Specify step time: 15 sec

    (b) Press "Start"

    (c) Yellow alert signifies the end of the process

12. If repeating the process, a second cleaning is not necessary. Start from Step 6.

13. When finished, log out of machine

Chromium Etching

1. Fill beaker with CR-7S Cr etchent

2. Insert sample into etchent for 15 sec

3. Remove sample, blow dry, rinse, and blow dry a second time

4. Pour etchent into "Acid Waste" when done with CR-7S

PMMA Removal

1. Remove PMMA with acetone

RIE (Technics Micro-RIE series 800)

1. Swipe in and turn on machine (switch on back of device)

2. Turn on CF4/O2 and set to 0.250 Torr with dial

3. Turn on Power and set to 100 Watts

4. Set timer: 8 min

5. Turn the dials off

6. Vent the chamber by alternately switching between vent and SOL'N to prevent chemical release (3x is sufficient)

7. Load sample slightly off center towards back of machine

8. Turn pump on with SOL'N

9. Turn on gas

10. Turn on Power and start timer simultaneously

11. Wait for timer to run down and turn power off, then gas off

12. Vent machine by alternating between vent and SOL'N (3x is sufficient)

13. Remove sample

Final Cr etch

1. Fill beaker with CR-7S solution

2. Place sample in beaker

3. Allow all Cr to dissolve before removing (Will not etch as quickly as first Cr layer due to oxidation in RIE process)

4. Pour empty etchent into "Acid Waste" container